Karlsruher Institut für Technologie

Spin Coupling to Superconducting Qubits

Zur Erlangung des akademischen Grades eines

Doktors der Naturwissenschaften

von der KIT-Fakultät für Physik des
Karlsruher Instituts für Technologie (KIT)

genehmigte

Dissertation

von

M.Sc. Simon Günzler

Tag der mündlichen Prüfung:
18. Juli 2025

Referent:	Prof. Dr. Wolfgang Wernsdorfer
Korreferent:	Prof. Dr. Ioan Pop

Abstract

Superconducting qubits, equipped with quantum non-demolition (QND) readout and active feedback control, have emerged as powerful tools to probe and manipulate their electromagnetic environment — from intrinsic microscopic defects to engineered spin systems in hybrid architectures. These hybrid systems aim to integrate the fast, versatile control of superconducting circuits with the exceptional coherence of spin systems such as magnetic molecules. However, the magnetic fields required for spin qubit operation present a challenge for superconductors and Josephson junctions, while the commonly used transverse (σ_x) coupling introduces mode hybridization, compromising QND spin readout.

In this work, we pursue an alternative approach: single-spin readout through a magnetic-field-resilient, longitudinal interaction that avoids mode hybridization and enables frequency-independent QND readout. First, we demonstrate longitudinal coupling between a $\{Cr_7Ni\}$ molecular spin ensemble and a granular aluminum (grAl) resonator, mediated by magnetic-field-induced modulation of the resonator's kinetic inductance. This enables measurement of a full $\{Cr_7Ni\}$ magnetization curve for a $f_{\mathrm{spin}} = 0{-}26\,\mathrm{GHz}$ spin frequency range ($B = 0{-}1\,\mathrm{T}$) using a fixed readout mode at $f_{\mathrm{r}} = 7.8\,\mathrm{GHz}$.

To scale this interaction to the single-spin level, we introduce the gralmonium: a fluxonium qubit incorporating a self-structured, lithographically defined $(20\,\mathrm{nm})^3$ granular aluminum junction that replaces the conventional superconductor-insulator-superconductor (SIS) junction. The gralmonium exhibits a fluxonium spectrum indistinguishable from SIS-based devices and maintains microsecond range coherence. Remarkably, its spectrum and coherence remain resilient up to 1.2 T, with only percent-level suppression of the superconducting gap evident in the qubit spectrum.

We further use the gralmonium as a sensitive probe of its magnetic environment. Energy relaxation in magnetic field reveals a paramagnetic spin-1/2 ensemble coupled to the qubit, constituting the dominant loss mechanism on resonance. Concomitantly, we observe magnetic-field-induced freezing of fast flux noise, consistent with surface spin polarization. Active reservoir engineering experiments rule out electron-spin-based origins for long-lived two-level systems in the qubit environment, which remain unaffected by magnetic field. Moreover, discrete fluctuations in the qubit frequency confirm the exponential sensitivity of the gralmonium to variations in the junction energy E_{J}, positioning it as a nanoscale magnetic sensor. Numerical simulations show that a single magnetic molecule placed atop the nanojunction induces a resolvable kHz-scale frequency shift. These results establish a viable path towards longitudinal single-spin readout using superconducting qubits.

Acknowledgments

Looking back on these eventful years, I can say: The journey really is the reward. I feel deep gratitude for the conversations, support, and opportunities that have shaped my time as a doctoral researcher. This journey wouldn't have been the same without the people who walked it with me.

Wolfgang, thank you for your supervision throughout all these years. What I appreciated most was your around-the-clock support. Whether it was a Tuesday morning or a Sunday evening, you always made time for hour-long discussions — often concluded with your legendary phrase: "just do it, we did this 20 years ago". That line became both a running joke and a challenge, and it consistently pushed me forward. I quickly realized how much I could learn from you beyond mere physics. I'm deeply grateful for the time and energy you invested in me — from your hands-on help in the lab and fixing the setup "over night" to your infectious enthusiasm for cryogenics and your relentless drive for efficiency. I admire your attention to detail, your way of thinking, and your openness in sharing it. Our discussions often nudged me just beyond my comfort zone and helped me see new perspectives. That kind of mentorship is rare, and I'm genuinely grateful for it.

Ioan, thank you for your guidance and expertise throughout this journey. Your passion for science is truly inspiring, and I admire your ability to ignite enthusiasm in others — often leaving them motivated as if the idea had been their own. You taught me the true value of how results are communicated, both in writing and on stage at seminars and conferences, and I learned that clarity and presentation are as important as the results themselves. Looking back, your attention to detail, insistence on precision, and dedication to high standards were not only crucial to the success of my project, but also to my own growth as a scientist. Thank you for all the time and energy you invested in me.

Dennis, I consider myself incredibly lucky to have shared this journey with you. From fabrication to data analysis, and from long days in the cleanroom to late-night laughter in the lab, we experienced so much together. Our strengths complemented each other perfectly, and working alongside you showed me that 1 + 1 can truly be more than 2. Our communication was remarkably smooth and efficient; at times it felt like we didn't even need words to understand each other. I still admire the synergy we developed and how naturally we tackled each challenge that came our way. Your skill and passion continue to impress me, but what meant even more was the trust and friendship we built along the way. Beyond a colleague, you've become a true friend, and I look forward to tackling many more problems together.

I would like to thank all my colleagues from both research groups I had the pleasure to be a part of. Your encouragement and collaboration contributed greatly to making these

last years not only productive, but also enjoyable. Thank you for the inspiring working atmosphere, the countless coffee breaks filled with both scientific and non-scientific discussions, the BBQs, the volleyball and spikeball sessions, and many other moments that made this time so memorable.
Ameya, thank you for the stimulating and cheerful discussions. Your warm-hearted nature never failed to brighten my mood, and I appreciate that you even laugh at my bad jokes.
Patrick and Martin, with joy I remember our time wiring up the BlueFors cryostat and cycling experiments together. Thank you for all the laughter, insightful conversations and the shared experiences at conferences. Martin, thank you especially for our many theory discussions and your patient explanations. I could always rely on your intuition, and I still admire how it always turned out to be right in the end.
Patrick, thank you for an amazing Bachelor project, which sparked my interests in an exciting research field — a spark that never went out. Over the years, you've become a role model, and I'm grateful for your guidance whenever I needed it.
Janic, I really enjoyed working alongside you and pushing the project forward. I'm excited that you're continuing down the path to measure a single molecule and I'm convinced that you'll be the one to finally achieve it! Thanks also to all my students who contributed to the project, your efforts made a real difference.
Nico, thank you for your help with the time-domain setup and for our discussions, especially those on TLS hyperpolarization. Your relentless helpfulness never went unnoticed.
Christoph, thank you for your practical support: from the Prevac to vacuum pumps, your practical wizardry kept the experiment on course.
Luca, I appreciated our vivid discussions and mutual help with the fridge. Thank you for your openness, curiosity, and our shared passion for espresso.
Viktor, thank you for our conversations about cryostats and qubit physics. What are the odds that we started this journey together and will cross the finish line on the same day?
Last but not least, a big thank you to the amplifier team for always having the right amplifier at the right frequency and for the discussions about automatic tune-up procedures.

Finally, I want to thank my family and friends. First and foremost, to my parents — thank you for your unwavering support throughout my life. I'm deeply grateful for the opportunities you gave me and the person you helped me become. To Felix, Melina, Julia, Janet, and Jasmijn: meeting you right at the beginning of my physics studies was a stroke of luck. Your friendship has been a steady source of support, inspiration, and joy ever since. Thank you for something truly special. And to Jasmijn for your love, and for the mutual support we shared while navigating our doctoral journeys together. Sharing both the hurdles and the milestones with you has made the journey so much richer.

Thank you all for being part of this amazing journey and I'm excited for all the adventures ahead!

Contents

List of Publications

Authors marked with † have contributed equally.

[1] **S. Günzler**†, J. Beck†, D. Rieger, N. Gosling, N. Zapata, M. Field, S. Geisert, A. Bacher, J. K. Hohmann, M. Spiecker, W. Wernsdorfer, and I. M. Pop, "Spin Environment of a Superconducting Qubit in High Magnetic Fields", arXiv, 10.48550/arXiv.2501.03661 (2025).

[2] **S. Günzler**†, D. Rieger†, M. Spiecker, T. Koch, G. A. Timco, R. E. P. Winpenny, I. M. Pop, and W. Wernsdorfer, "Kinetic inductance coupling for circuit QED with spins", arXiv, 10.48550/arXiv.2502.07605 (2025).

[3] D. Rieger†, **S. Günzler**†, M. Spiecker, P. Paluch, P. Winkel, L. Hahn, J. K. Hohmann, A. Bacher, W. Wernsdorfer, and I. M. Pop, "Granular aluminium nanojunction fluxonium qubit", Nat. Mater. **22**, 194–199 (2023).

[4] D. Rieger†, **S. Günzler**†, M. Spiecker, A. Nambisan, W. Wernsdorfer, and I. M. Pop, "Fano Interference in Microwave Resonator Measurements", Phys. Rev. Appl. **20**, 014059 (2023).

[5] N. Zapata, I. Takmakov, **S. Günzler**, S. Geisert, S. Ihssen, M. Field, A. Nambisan, D. Rieger, T. Reisinger, W. Wernsdorfer, and I. M. Pop, "Granular Aluminum Parametric Amplifier for Low-Noise Measurements in Tesla Fields", Phys. Rev. Lett. **133**, 260604 (2024).

[6] D. Gusenkova, F. Valenti, M. Spiecker, **S. Günzler**, P. Paluch, D. Rieger, L.-M. Pioraş-Ţimbolmaş, L. P. Zârbo, N. Casali, I. Colantoni, A. Cruciani, S. Pirro, L. Cardani, A. Petrescu, W. Wernsdorfer, P. Winkel, and I. M. Pop, "Operating in a deep underground facility improves the locking of gradiometric fluxonium qubits at the sweet spots", Appl. Phys. Lett. **120**, 054001 (2022).

[7] M. Spiecker, P. Paluch, N. Gosling, N. Drucker, S. Matityahu, D. Gusenkova, **S. Günzler**, D. Rieger, I. Takmakov, F. Valenti, P. Winkel, R. Gebauer, O. Sander, G. Catelani, A. Shnirman, A. V. Ustinov, W. Wernsdorfer, Y. Cohen, and I. M. Pop, "Two-level system hyperpolarization using a quantum Szilard engine", Nat. Phys. **19**, 1–6 (2023).

[8] D. Willsch†, D. Rieger†, P. Winkel, M. Willsch, C. Dickel, J. Krause, Y. Ando, R. Lescanne, Z. Leghtas, N. T. Bronn, P. Deb, O. Lanes, Z. K. Minev, B. Dennig, S. Geisert, **S. Günzler**, S. Ihssen, P. Paluch, T. Reisinger, R. Hanna, J. H. Bae, P. Schüffelgen, D. Grützmacher, L. Buimaga-Iarinca, C. Morari, W. Wernsdorfer, D. P. DiVincenzo, K. Michielsen, G. Catelani, and I. M. Pop, "Observation of Josephson harmonics in tunnel junctions", Nat. Phys. **20**, 815–821 (2024).

[9] S. Geisert†, S. Ihssen†, P. Winkel, M. Spiecker, M. Fechant, P. Paluch, N. Gosling, N. Zapata, **S. Günzler**, D. Rieger, D. Bénâtre, T. Reisinger, W. Wernsdorfer, and I. M. Pop, "Pure kinetic inductance coupling for cQED with flux qubits", Appl. Phys. Lett. **125**, 064002 (2024).

List of Figures

Part I

On Superconducting Qubits and Spins

1 Better Together: Spins and Superconducting Circuits – an Introduction

1.1 Introduction & Manuscript Overview

This thesis pursues a simple but far-reaching idea: marry the unrivaled coherence of an individual spin with the agile control of a superconducting qubit – through a longitudinal, magnetic-field-resilient interface.

Quantum information processing (QIP) seeks to exploit the principles of superposition and entanglement in coherent quantum states for a wide range of applications, from factoring large integers and simulating complex quantum systems in quantum chemistry [10–12] to enabling non-computing technologies such as quantum communication [13–15] and quantum sensing [16–18]. Among the leading hardware platforms, spin systems stand out for their exceptional coherence, stemming from their intrinsic isolation from the environment [19–22]. However, this same isolation poses a significant challenge for efficient manipulation and readout of spins. In parallel, superconducting microwave circuits offer rapid and high-fidelity quantum control and readout, leveraging their macroscopic electromagnetic fields. Yet, their extended structure exposes them to a multitude of uncontrolled environmental degrees of freedom, ultimately limiting their coherence times [7, 23–37]. Consequently, hybrid quantum architectures combining the long-lasting coherence of spins with the agile control, fast manipulation, and versatile design of superconducting circuits present a compelling solution.

Over the past decade, superconducting microwave resonators have demonstrated strong coupling to various spin systems, including vacancy centers in diamond [38], donor atoms in crystalline substrates [39–41], and molecular magnets [42–45]. However, these achievements have not yet fully realized the combined potential of spin systems and superconducting circuits: inhomogeneous broadening in ensembles significantly degrades spin coherence and QIP requires coherent control and readout at the level of individual spins - a milestone only recently achieved for single electron spins [22, 46].

So far, interfacing superconducting circuits with spins primarily relies on transverse coupling, wherein mode hybridization between the spin and the superconducting circuit mediates the interaction. While this enables Purcell-enhanced spin readout [22, 40–43, 46,

47], it is restricted to the cavity frequency and inherently demolishes the spin state [47–49]. Longitudinal coupling between spins and superconducting circuits offers a tantalizing alternative: it does not hybridize the modes, enabling quantum non-demolition spin readout independent of the qubit-resonator frequency detuning [50–57]. However, its realization is challenging, as many key elements of the superconducting circuit toolbox, such as Josephson junctions and microwave resonators made from conventional superconductors, are vulnerable to high magnetic fields required for spin qubit operation. Thus, to truly unlock the potential of universal superconductor-spin hybrid architectures, it is imperative to develop a magnetic-field-resilient longitudinal coupling interface that bridges the gap between the macroscopic size of superconducting circuits and the nanoscopic interaction volume of individual spins.

My PhD thesis addresses this challenge in two stages. First, we realize a non-demolition, detuning-independent readout of a $\{Cr_7Ni\}$ molecular spin qubit ensemble by coupling its collective magnetization to the kinetic inductance of a granular aluminum (grAl) resonator. This experiment conceptually demonstrates longitudinal coupling to spins via kinetic inductance and enables time-resolved measurements of the spin ensemble's excitation and decay dynamics at GHz detuning from the readout. In the second stage, we scale the same principle down to the level of individual spins. Driven by considerations for single spin coupling, we develop a novel type of Josephson junction - the grAl nanojunction - which combines the advantageous coherence of conventional tunnel junctions with the nanoscopic footprint required for single spin interaction. To harness its sensitivity to the dipolar field of a single spin, we incorporate the nanojunction into a superconducting fluxonium qubit, which we nickname gralmonium. A zero-field characterization of the gralmonium confirms a spectrum and coherence comparable to conventional superconducting qubits. Moreover, discrete fluctuations of the qubit frequency highlight the circuit's high sensitivity to variations within the nanojunction and its immediate environment. Measurements in high magnetic fields up to 1 T demonstrate remarkable magnetic field resilience and reveal previously unobserved spin environments coupled to superconducting qubits. These experiments confirm the readiness of the gralmonium for spin sensing applications, and we predict that the field-resilient longitudinal coupling can achieve sensitivity at the kHz-level for an individual spin. Together, these steps establish a practical route to QND single-spin readout in hybrid quantum architectures.

This thesis is organized into four main parts, designed to clearly distinguish the core scientific narrative from supporting yet scientifically valuable results, presented on a scale of increasing technical detail. **Part I: On Superconducting Qubits and Spins** presents the central developments and findings of the thesis, which collectively build towards the overarching goal of achieving longitudinal coupling between a single spin and a superconducting qubit. As novel superconducting circuits and methods are developed and characterized throughout this manuscript, additional measurements - while not directly advancing the central thesis objective - provide important insights and standalone scientific value. These are compiled in **Part II: Device Characterization & Extended Results**. Importantly, these sections are distinct from the **Appendix (Part IV)**, which is reserved for technical and methodological details critical to the reproducibility of the experiments, including fabrication protocols and the measurement setup. Finally, **Part III: Conclusion**

and Future Directions summarizes the key achievements of the thesis, places them in the context of the long-term efforts ongoing in the research group and outlines the prospective research paths that are now open for exploration.

1.2 Hybrid Quantum Architectures

Fault-tolerant QIP will require registers of at least $10^3 - 10^6$ qubits that can be entangled, controlled, and measured on demand. Consequently, every prospective hardware platform must be evaluated against the five DiVincenzo criteria: deterministic state preparation, long coherence, universal control, high-fidelity readout, and scalable fabrication [58]. Yet no single implementation meets the full set simultaneously and each platform offers distinct advantages and faces specific challenges [45, 59–61]. For instance, trapped-ion and neutral-atom systems excel in coherence but two-qubit gate operations are comparatively slow and spatially cumbersome. Superconducting circuits enable nanosecond-scale control and dense on-chip connectivity, yet coherence remains limited to the 0.1–1 ms range. Spin-based qubits, whether donor spins in crystalline substrates or molecular magnets, offer millisecond lifetimes, but their magnetic-dipole coupling to microwave fields is weak and precise placement at scale is challenging. Semiconductor quantum dots offer strong electric-field coupling (few MHz) and fast gates, at the cost of deteriorated lifetime. These complementary strengths and limitations across different physical qubit encodings naturally suggest hybrid architectures, that combine heterogeneous subsystems to exploit only their favorable attributes, while mitigating their respective shortcomings. However, what design principles enable the integration of two (or more) imperfect systems into a hybrid architecture whose combined capabilities outperform those of the individual components?

Circuit-QED (cQED) itself exemplifies a successful "intra-technology" hybrid [48, 59]: linear cavities supply clean, QND readout while nonlinear Josephson qubits supply fast, addressable quantum logic. Although cQED does not bridge fundamentally different physical systems, it illustrates a key design principle of hybrid architectures: balancing strong information transfer against measurement back-action (e.g., Purcell decay, photon shot noise). Because superconducting circuits couple strongly to both electric and magnetic fields and are lithographically versatile, they serve as a foundational platform for many hybrid quantum technologies. Examples include coupling superconducting circuits to semiconducting spin qubits, NV centers, and a wide variety of spin systems [45, 59–61]. Among these, coupling to spin systems is particularly promising, offering a route to bridge the intrinsic isolation of spins with the flexible control afforded by superconducting circuits.

In this manuscript, we focus on utilizing the spin of magnetic molecules, which provides several advantages for QIP and the eventual scaling towards single-spin readout. These molecules, consisting of magnetic atoms embedded in an organic ligand, allow for chemical tailoring of their spin properties. Moreover, the surrounding ligand environment protects the spin properties, ensuring reproducible characteristics across different samples within

different environments. Importantly, magnetic molecules can be engineered to carry large spin moments on the order of $\mu = 10\mu_B$, substantially enhancing the signal for detecting individual spins (cf. Section 3.3). Their multi-level (qudit) structure offers prospects for embedding quantum error correction within a single physical unit [45]. Furthermore, the ability to grow these molecules into single crystals of chemically identical units enables ensemble characterization prior to selecting candidate systems for single-spin experiments [62, 63]. Another practical advantage lies in the modularity of the hybrid approach: the superconducting circuit and the magnetic molecule can be independently fabricated and characterized before coupling them. This is particularly critical for superconducting devices with demanding fabrication requirements, as we will see in Section 3.1.

In the hybrid architecture pursued here, the spin component, i.e. molecular magnets with tailored anisotropy, is defined by chemical synthesis. In contrast, the superconducting circuit must be precisely engineered to mediate information exchange between the two systems via an interaction Hamiltonian H_{int}. This interaction governs whether the hybrid system harnesses the complementary strengths of its components or inherits their limitations. Conventional transverse coupling employs the radio-frequency (rf) magnetic field of the superconducting circuit, e.g. a resonator at frequency ω_r, to couple with the electron spin resonance at the Larmor frequency ω_L. However, this interaction is spectrally selective: effective energy exchange requires resonance conditions, i.e. $\omega_r \approx \omega_L$. Rather than relying on the transverse interaction and its associated dynamic rf field, we exploit the longitudinal, static dipolar field of the spin, which locally perturbs the superconducting condensate. This perturbation translates into a modulation of the superconductor's kinetic inductance L_{kin} (cf. Section 1.3.3) instead of relying on coherent energy exchange, enabling coupling that is independent of the frequency detuning between the two platforms.

Achieving a measurable modulation of the superconducting condensate by the dipolar field of a single spin, however, necessitates expanding the superconducting circuit toolbox with components specifically tailored for spin sensitivity. Section 1.3 introduces this expanded toolbox and outlines the design of the superconducting subsystem within our hybrid platform. Section 1.4 concludes the chapter with a comparison of longitudinal and transverse coupling schemes in the context of cQED.

1.3 Superconducting Quantum Circuits: A Versatile Toolbox

Hybrid spin-superconductor platforms promise the coherence of spins combined with the precise control offered by superconducting microwave circuits. To realize this control via a novel, longitudinal interaction, this section introduces the superconducting circuitry in three stages: beginning with linear resonators, advancing to nonlinear Josephson-based qubits, culminating in high-kinetic-inductance elements engineered to enable longitudinal spin-superconductor coupling.

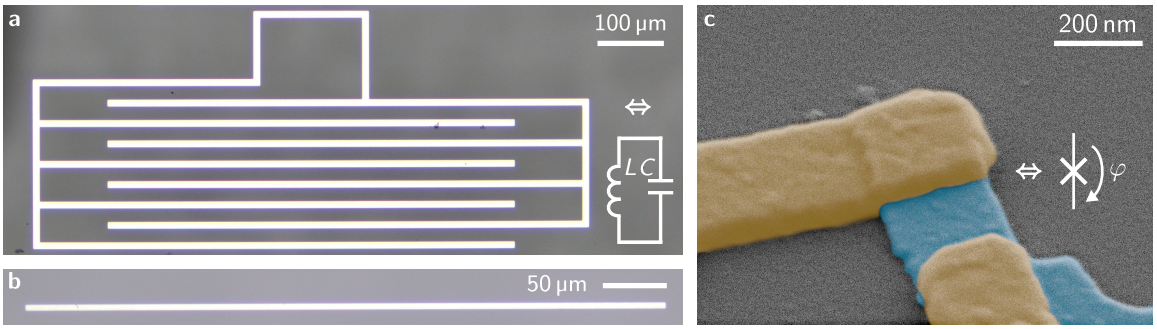

Figure 1.1: Superconducting circuits toolbox. **a** Optical micrograph of a planar superconducting microwave resonator, consisting of an interdigitated capacitor C and an inductor L (top). **Inset:** Circuit schematic of a harmonic LC oscillator. **b** Optical micrograph of a high-impedance stripline resonator operating at microwave frequencies. The compact layout leverages the high kinetic inductance of granular aluminum. **c** False-colored scanning electron microscope (SEM) image of a superconductor-insulator-superconductor tunnel Josephson junction (JJ), where the bottom and top aluminum electrodes (blue and yellow) are separated by a nanometer-thin AlO_x tunnel barrier. **Inset:** Circuit symbol for a JJ with phase difference φ across the junction. Panel c is adapted from Ref. [8].

1.3.1 Superconducting Resonators

Across all implementations of superconducting circuits, coherent excitations are encoded in macroscopic resonant structures fabricated from superconducting thin films patterned on crystalline substrates. Analogous to their classical counterparts, these circuits comprise fundamental elements such as capacitors and inductors. In the simplest case of a linear LC oscillator (cf. Fig. 1.1a), the resonance frequency $\omega_\mathrm{r} = 1/\sqrt{LC}$ is precisely engineered in the GHz regime by tailoring the geometry of the capacitive and inductive components. Capacitance, arising from electric field energy between conductors, is typically tuned through the layout of large superconducting pads or interdigitated electrodes. Inductance, linked to magnetic field energy around current-carrying wires, is controlled by modifying the length and shape of meandering traces. Due to their straightforward design, fabrication, and analysis, resonators serve as versatile, powerful tools for material characterization [64–75], identifying loss mechanisms in superconducting circuits [76–84], and comparing fabrication techniques and experimental setups [77, 85–89]. Moreover, when integrated with superconducting qubits in intra-technology hybrid systems (cf. Section 1.2), they significantly contributed to the remarkable progress of superconducting qubit architectures. In Chapter 2, we harness these benefits in a proof-of-concept demonstration of microwave-based longitudinal readout of a spin ensemble.

Beyond their practical use as microwave probes, linear LC oscillators form the conceptual backbone for modeling superconducting circuits within the cQED framework. To motivate and eventually engineer the spin-superconductor interaction introduced in Section 1.4, as well as to lay the groundwork for describing the novel superconducting circuit elements throughout the manuscript, we briefly revisit the harmonic oscillator as a foundational

example. Full derivations can be found in Ref. [48]. The dynamics of a harmonic mode are commonly expressed in three equivalent notations [48]:

$$H_\mathrm{r} = \frac{Q^2}{2C} + \frac{\Phi^2}{2L} \tag{1.1}$$

$$= 4E_\mathrm{C}n^2 + \frac{1}{2}E_\mathrm{L}\varphi^2 \tag{1.2}$$

$$= \hbar\omega_\mathrm{r}(a^\dagger a + \frac{1}{2})\,. \tag{1.3}$$

In Eq. (1.1), Q and Φ represent the charge and flux operators, directly reflecting electrostatic and magnetic energy stored in the circuit's capacitive and inductive elements, respectively. Equation (1.2) recasts this in terms of the superconducting condensate: the number operator $n = Q/(2e)$ represents the discrete number of Cooper pairs, and the phase operator $\varphi = (2\pi/\Phi_0)\Phi$ denotes the phase of the condensate wavefunction. Here, $E_\mathrm{C} = e^2/2C$ is the charging energy, $E_\mathrm{L} = (\Phi_0/2\pi)^2/L_\mathrm{q}$ is the inductive energy and $\Phi_0 = \mathrm{h}/2\mathrm{e}$ is the superconducting magnetic flux quantum. Since these variables satisfy the canonical commutation relation $[\Phi, Q] = \hbar[\varphi, n] = i\hbar$, we express the system as a quantum harmonic oscillator in Eq. (1.3), using bosonic creation and annihilation operators $a^\dagger$ and a. This description emphasizes the quantized energy levels of the oscillator and is particularly useful when analyzing photon-mediated interactions or excitations. For the remainder of this manuscript, we adopt the common convention of omitting the zero-point energy term (i.e. the factor $1/2$ in Eq. (1.3))

1.3.2 Superconducting Qubits

Josephson Junctions as a Source of Nonlinearity

While linear resonators illustrate the fundamental capabilities of superconducting circuits and the utility of cQED, the full toolbox of superconducting circuits crucially includes nonlinear elements without classical analogs, most notably Josephson junctions (JJs). These enable the construction of superconducting artificial atoms that can be operated within a two-level qubit manifold. Consequently, they fueled the rise of superconducting qubits, and they will be re-engineered in novel ways throughout this thesis, to meet the requirements of longitudinal single-spin coupling.

The Josephson effect [90] describes the non-dissipative tunneling of Cooper pairs across a weak link between two superconducting electrodes. Such weak links may be realized via a normal metal, a semiconductor, or a geometric constriction on the scale of the superconducting coherence length. In practice, however, the vast majority of superconducting qubits is realized using a superconductor-insulator-superconductor (SIS) Josephson junction (JJ), composed of two aluminum electrodes separated by a nm-thin aluminum oxide (AlO_x) layer (cf. Fig. 1.1c) [48, 91, 92]. Coherent tunneling across this barrier couples the superconducting wavefunctions on either side of the junction, linking the phase difference

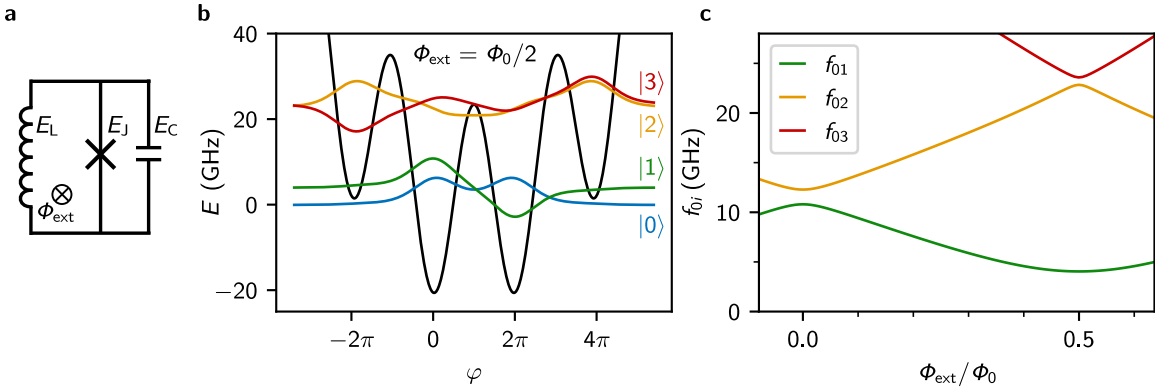

Figure 1.2: Fluxonium superconducting qubit. **a** Circuit schematic of the fluxonium qubit. A Josephson junction with energy E_J is shunted by a superinductance with inductive energy E_L forming a loop threaded by an external magnetic flux Φ_{ext}. The junction capacitance, combined with other geometric capacitances in the circuit, gives rise to a charging energy E_C. **b** Potential energy landscape of the fluxonium at the half-flux sweet spot ($\Phi_{ext} = 0.5\,\Phi_0$), with the first four eigenfunctions plotted and vertically offset by their respective eigenenergies. Parameters are $E_J/h = 23.4$ GHz, $E_C/h = 15$ GHz and $E_L/h = 0.57$ GHz consistent with Ref. [3]. **c** Fluxonium spectrum as a function of external flux Φ_{ext}.

φ between the junction electrodes to a dissipation-less supercurrent, governed by the current-phase relation (CφR):

$$I(\varphi) = I_c \sin(\varphi)\,. \tag{1.4}$$

Here, the junction critical current I_c represents the maximum supercurrent that can be supported at zero voltage. The time evolution of the phase difference is linked to the voltage across the junction via the voltage-phase relation:

$$V = \frac{\Phi_0}{2\pi}\frac{\mathrm{d}\varphi}{\mathrm{d}t}\,. \tag{1.5}$$

Combining these relations yields the energy-phase relation (EφR), which characterizes the energy associated with Cooper pair tunneling:

$$E(\varphi) = \int VI\mathrm{d}t = E_J \int \sin(\varphi)\frac{\mathrm{d}\varphi}{\mathrm{d}t} = -E_J\cos(\varphi)\,, \tag{1.6}$$

where $E_J = \Phi_0 I_c/(2\pi)$ denotes the Josephson energy. This EφR is central to superconducting qubits, as it introduces non-dissipative, intrinsic nonlinearity into the circuit Hamiltonian.

Superconducting Qubits

Over the past three decades, superconducting qubits have evolved from proof-of-concept devices [93–95] to precision-engineered platforms within the framework of circuit quantum electrodynamics (cQED) [48, 96–98]. They now demonstrate coherence times extended by up to six orders of magnitude [99–101], quantum non-demolition (QND) readout [102, 103]

and real-time feedback control. Beyond progress towards universal quantum computing, these advances have enabled seminal experiments, including the observation of quantum jumps and trajectories [104–106], active-feedback error correction [107–111], studies of non-Markovian qubit dynamics in open quantum systems [7, 37], a proof-of-concept for a novel current standard in metrology [112–114] and experiments probing foundational aspects of quantum mechanics [115–118].

Despite this technological evolution, the key concept behind superconducting qubits remains remarkably simple: a JJ introduces nonlinearity into an otherwise linear LC circuit, thereby shaping the circuit's energy landscape. In addition to capacitive and inductive shunts around the JJ, conventional SIS JJs contribute a geometric capacitance arising from the overlapping electrodes. The interplay among the characteristic energy scales E_C, E_J and E_L defines various qubit modalities, such as the transmon, the flux qubit, or the fluxonium [91, 119]. In flux-based designs, like the fluxonium qubit pursued in this work, the JJ is shunted by an inductive flux loop (cf. Fig. 1.2a). For the fluxonium, this shunt is denoted superinductance, characterized by an impedance $Z = \sqrt{L/C}$ that exceeds the superconducting resistance quantum $R_\mathrm{q} = h/(2e)^2$, which makes the fluxonium resilient to charge noise [99]. Experimentally, superinductors are realized using JJ arrays [99, 101, 120–123], high-kinetic-inductance materials [124–126] or geometric aluminum spirals [127, 128].

Threading the flux loop with an external flux Φ_ext introduces an offset phase $\varphi_\mathrm{ext} = 2\pi\Phi_\mathrm{ext}/\Phi_0$ in the inductive term. Promoting φ to an operator in Eq. (1.6) and incorporating it into the harmonic oscillator Hamiltonian yields the fluxonium Hamiltonian

$$H_\mathrm{flux} = 4E_\mathrm{C}n^2 + \frac{1}{2}E_\mathrm{L}\left(\varphi - 2\pi\frac{\Phi_\mathrm{ext}}{\Phi_0}\right)^2 - E_\mathrm{J}\cos\varphi\,. \tag{1.7}$$

At half-flux bias, the inductive energy and the Josephson energy form a double-well potential, shown in Fig. 1.2b. Numerical diagonalization of H_flux (Eq. (1.7)) yields the fluxonium eigenstates and transition frequencies. The energy spectrum exhibits periodic modulation in Φ_ext (cf. Fig. 1.2c), with sweet spots at $\Phi_\mathrm{ext} = 0$ and $\Phi_\mathrm{ext} = 0.5\,\Phi_0$, where first-order flux noise sensitivity vanishes. Importantly, the energy spectrum of superconducting qubits is anharmonic, i.e. the energy levels are distributed non-equidistantly (cf. Fig. 1.2c). This allows selective addressing of the lowest two states, denoted $|0\rangle$ and $|1\rangle$ (or equivalently $|g\rangle$ and $|e\rangle$), thereby obtaining a well-isolated, two-level qubit subspace. Nonetheless, it is essential to recognize the intrinsically multi-level nature of superconducting circuits. Excited states beyond the computational subspace play a key role in phenomena such as dispersive shifts, measurement-induced transitions, gate-induced leakage, and Purcell decay, which requires considering the full level structure for practical scenarios.

1.3.3 Kinetic Inductance Circuits

In addition to geometric inductance L_geo, which stores energy in the magnetic field and opposes changes in current, superconductors exhibit an additional inductive response

arising from the inherent inertia of Cooper pairs. This kinetic inductance reflects the kinetic energy stored in the momentum of the superconducting condensate and resists changes in supercurrent by opposing the acceleration of Cooper pairs. In the JJ discussed in Section 1.3.2, a time-varying supercurrent modulates the phase φ, thereby inducing a voltage (cf. Eq. (1.5))

$$\frac{\mathrm{d}I}{\mathrm{d}t} = I_\mathrm{c}\cos(\varphi)\frac{\mathrm{d}\varphi}{\mathrm{d}t} = \cos(\varphi)\frac{2\pi I_\mathrm{c}}{\Phi_0}V\,.$$

Here, we identify a nonlinear Josephson inductance

$$L = \frac{\Phi_0}{2\pi I_\mathrm{c}}\frac{1}{\cos(\varphi)} = \frac{L_\mathrm{J}}{\cos(\varphi)}\,, \tag{1.8}$$

reflecting the delayed response of the condensate to phase changes.

More generally, kinetic inductance is a fundamental characteristic of all superconductors. It is a direct implication of the first London equation $\mathrm{d}J/\mathrm{d}t = (nq^2/m)E$, where J is the current density, n is the density of Cooper pairs (of charge q and mass m) and E is the electric field. For a uniform wire of length l and cross-section A, the voltage drop $V = l \cdot E$ leads to a change in the current $I = J \cdot A$ such that we identify a kinetic inductance L_kin [129, 130]:

$$V = L_\mathrm{kin}\mathrm{d}I/\mathrm{d}t \qquad \text{with} \qquad L_\mathrm{kin} = \frac{ml}{nq^2A}\,, \tag{1.9}$$

Disordered superconductors, such as NbN [131–133], NbTiN [134–136], InOx [137, 138] and granular aluminum (grAl) [72, 139, 140] exhibit significantly enhanced kinetic inductance due to their lower charge carrier densities relative to elemental superconductors. Consequently, their kinetic inductance can exceed the geometric contribution to the inductance by orders of magnitude (cf. Eq. (1.9)), captured in the kinetic inductance fraction

$$\alpha = \frac{L_\mathrm{kin}}{L_\mathrm{kin} + L_\mathrm{geo}} \approx 1\,.$$

This makes disordered superconductors particularly advantageous for longitudinal spin-superconductor coupling, since our implementation relies on modulating the superconducting condensate, e.g. by locally suppressing the Cooper pair density n (cf. Eq. (1.9)). Moreover, the ability to continuously engineer kinetic inductance through the geometry of the superconducting film (cf. Eq. (1.9)) makes disordered superconductors attractive for integration into quantum devices. Their tunable inductive properties position disordered superconductors as versatile and valuable elements in the superconducting circuit toolbox (cf. Fig. 1.1b).

Granular Aluminum

Beyond its high kinetic inductance, the suitability of a material for quantum circuits is determined by its overall profile and performance, including microwave losses, magnetic

field resilience and nonlinearity. In this work, we employ superconducting granular aluminum (grAl), a superconducting material fabricated via evaporation of aluminum in a dynamic oxygen atmosphere. This single-step fabrication process offers a notable advantage over JJ arrays, which typically require multiple fabrication steps. GrAl consists of self-assembled crystalline aluminum grains, approximately 2–4 nm in diameter [140–142], embedded within an amorphous aluminum oxide (AlO_x) matrix. The degree of oxidation during deposition enables continuous tuning of the normal-state resistivity within the range $\rho = 1\text{–}10^4\,\mu\Omega\,\mathrm{cm}$, approaching the superconductor-to-insulator transition [140, 142, 143]. As a result, the grAl kinetic inductance can be widely tuned, reaching values on the order of nH/□ for 20 nm thick films [72, 139, 144]. From the perspective of quantum circuit integration, grAl offers low dissipation, with microwave loss measurements demonstrating internal quality factors of $Q_\mathrm{i} \sim 10^5\text{–}10^6$ in the single photon regime [4, 72, 124, 145, 146]. Notably, these low levels of microwave loss persist in magnetic fields up to 1 T, with critical fields exceeding several Tesla [4, 126, 139, 147]. This renders grAl circuits highly suitable for hybrid quantum architectures incorporating spins, which typically require high magnetic fields in the range of 10^2 mT for spin qubit operation.

So far, grAl has been successfully employed in various circuit elements and devices, including microwave resonators [4, 72, 145, 146] (see Fig. 1.1b), superinductors in fluxonium qubits [124], field-resilient quantum-limited parametric amplifiers [5], and weakly nonlinear resonators and transmon qubits [148, 149]. Furthermore, its chemical and structural similarity to conventional Al/AlO_x/Al overlap JJs motivates the systematic investigation of microwave losses and noise mechanisms [4, 72, 124, 144–146]. Importantly, this allows to model grAl both as a disordered material and as a network of JJs [150].

This duality becomes evident when considering its kinetic inductance. In the low temperature limit ($T \ll T_\mathrm{c}$), the Ambegaokar-Baratoff relation $I_\mathrm{c} = \pi\Delta/(2eR_\mathrm{n})$ [130] for the JJ critical current can be used to express the Josephson inductance L_J (cf. Eq. (1.8)) in terms of fundamental material properties

$$L_\mathrm{J} = \frac{\hbar R_\mathrm{n}}{\pi\Delta}, \tag{1.10}$$

where Δ is the superconducting gap, e is the electron charge and R_n is the normal state resistance. This result is consistent with that obtained from the Mattis-Bardeen theory [145, 151] for superconductors in the local, dirty limit, where the mean free path l is much smaller than the penetration depth λ and the coherence length χ ($l \ll \lambda, \chi$). Throughout this manuscript, grAl is described from both perspectives interchangeably, as a disordered superconducting material as well as a network of JJs.

1.4 Readout: cQED for Superconducting Circuits and Spins

To utilize a two-level system (TLS), such as a spin or a superconducting qubit, within an (intra-technology) hybrid architecture for QIP, it is essential to extract information about its quantum state through controlled interaction. This is typically accomplished by coupling

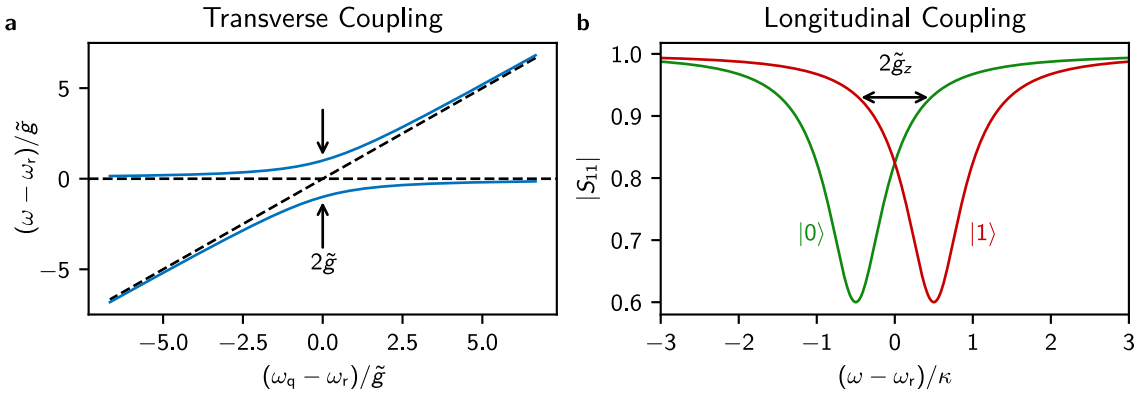

Figure 1.3: Signatures of transverse and longitudinal qubit-resonator coupling. **a** Normalized eigenfrequencies $(\omega - \omega_r)/\tilde{g}$ of the transversely coupled qubit-resonator system as a function of normalized detuning $(\omega_q - \omega_r)/\tilde{g}$, where ω_r is the bare resonator frequency (horizontal dashed line), ω_q is the bare qubit frequency (diagonal dashed line), and $\tilde{g}$ is the coupling strength. The characteristic avoided crossing, with minimum level splitting $2\tilde{g}$, is indicative of transverse coupling. **b** Simulated resonator response depicting the amplitude of the microwave reflection coefficient $|S_{11}|$ versus normalized frequency detuning $\omega - \omega_r$, with κ denoting the resonator linewidth. A longitudinal interaction results in a qubit-state-dependent shift of the resonator frequency, yielding distinct resonances for the states $|0\rangle$ (green) and $|1\rangle$ (red), separated by $2\tilde{g}_z$. Note that in the dispersive regime $|\omega_r - \omega_q| \gg \tilde{g}$, transverse coupling implements an approximately longitudinal readout, leading to a dispersive shift χ (cf. Eq. (1.13)).

the TLS to a harmonic mode, realized e.g. with a superconducting microwave resonator. The coupling can be transverse, leading to coherent qubit-resonator energy exchange, or longitudinal, inducing a purely state-dependent frequency shift. This subsection contrasts the two coupling mechanisms, highlights their respective merits and drawbacks for both spins and for superconducting qubits, and motivates the longitudinal interaction strategy pursued in the remainder of this thesis.

1.4.1 Transverse Coupling

In both spin- and superconducting qubits, transverse coupling arises from a dipolar interaction and is described by a common theoretical framework: the quantum Rabi Hamiltonian. For a spin $s = 1/2$, representing an ideal TLS, the magnetic moment $\vec{\mu}$ interacts with the resonator's magnetic field at the spin location $\vec{B}_r = \delta\vec{B}_r(a^\dagger + a)$, resulting in the interaction Hamiltonian $H_{int} = -\vec{\mu}\vec{B}_r$. Here, $\delta\vec{B}_r$ denotes the microwave field zero-point fluctuations at the spin location and the spin magnetic moment is given by $\vec{\mu} = -g\mu_B\vec{S}/\hbar$, where $\vec{S}$ is the spin operator, g is the Landè factor and μ_B is the Bohr magneton. The coupled system thus follows the quantum Rabi Hamiltonian

$$\begin{aligned} H_{Rabi} &= H_r + H_q + H_{int}^{\perp} \\ &= \hbar\omega_r a^\dagger a + \hbar\frac{\omega_q}{2}\sigma_z + \hbar\tilde{g}(\sigma_+ + \sigma_-)(a^\dagger + a)\,, \end{aligned} \tag{1.11}$$

with an effective coupling strength[1] $\tilde{g} = g\mu_B/\hbar\delta B_r/4$ and the Pauli raising and lowering operators σ_+ and σ_-. Importantly, neither $(a^\dagger + a)$ nor $\sigma_x = (\sigma_+ + \sigma_-)/2$ are diagonal in their respective bases, i.e. $[H_{int}^{\perp}, \sigma_z] \neq 0$ and $[H_{int}^{\perp}, a^\dagger a] \neq 0$. Thus, the interaction does not conserve either the spin state or the photon number in the resonator.

In superconducting qubits, analogous dipole interactions via charge or flux degrees of freedom lead to the same form of the interaction Hamiltonian [48]. A key difference between spins and superconducting qubits, however, is the achievable coupling strength. For spins, it is typically on the order of up to $\tilde{g} \sim 10^1$–10^3 Hz [59, 152, 153], whereas for superconducting qubits it can be engineered to $\tilde{g} \sim 10^1$–10^3 MHz due to their macroscopic dipole moments, strong interaction with electromagnetic fields, and the ability to precisely design circuit QED architectures [48, 59, 154].

Under the rotating wave approximation (valid when $\tilde{g} \ll \omega_q, \omega_r$) Eq. (1.11) simplifies to the Jaynes-Cummings Hamiltonian

$$H_{JC} = H_r + H_q + \hbar\tilde{g}(\sigma_+ a + \sigma_- a^\dagger)\,, \tag{1.12}$$

where we can identify a coherent excitation exchange between the qubit and the harmonic oscillator. This interaction gives rise to an avoided level crossing in the frequency domain, providing a clear experimental signature of transverse qubit-resonator coupling (cf. Fig. 1.3a). In the dispersive regime, where the qubit-resonator detuning $\Delta = |\omega_r - \omega_q| \gg \tilde{g}$, this Hamiltonian can be approximately diagonalized to a dispersive interaction

$$H_{JC} \approx H_{Disp} = H_r + H_q + \hbar\chi\sigma_z a^\dagger a\,, \tag{1.13}$$

where the readout mode is shifted by the dispersive shift $\chi = \tilde{g}^2/\Delta$, depending on the qubit state (cf. Fig. 1.3b). Since Eq. (1.13) commutes with σ_z, $[H_{Disp}, \sigma_z] = 0$, this interaction enables quantum non-demolition (QND) readout. For this reason, dispersive readout has shown great success in superconducting qubit architectures, enabling single-shot, high-fidelity measurements and real-time feedback [7, 104–106, 117]. The underlying transverse interaction, however, entails higher order corrections to Eq. (1.13), which lead to non-QND effects such as measurement-induced qubit transitions [155–157] and Purcell decay [48, 158], and motivate the development of alternative QND interactions.

1.4.2 Longitudinal Coupling

Longitudinal spin-resonator interaction presents an appealing alternative, which directly links the spin state to the resonator frequency:

$$H_{int}^{\parallel} = \hbar\tilde{g}_z\sigma_z a^\dagger a\,, \tag{1.14}$$

[1] Throughout this manuscript, we denote coupling constants using a tilde accent, $\tilde{g}$, to clearly distinguish them from the spin gyromagnetic factor, conventionally represented as g.

where the longitudinal coupling strength $\tilde{g}_z = \delta\omega/2$ reflects the spin-flip induced frequency shift (cf. Fig. 1.3b). This interaction can arise for example from a spin state dependent inductance $L = L(\sigma_z)$. Importantly, it is diagonal in both spin and harmonic oscillator bases: $[H_{\text{int}}^{\parallel}, \sigma_z] = [H_{\text{int}}^{\parallel}, a^\dagger a] = 0$. Consequently, longitudinal coupling preserves both the spin state and resonator photon number, enabling a frequency-independent, quantum non-demolition (QND) readout [50–52]. We note here that there are various definitions of longitudinal and transverse coupling in the literature, including cases where an interaction Hamiltonian with only one diagonal component is referred to as a longitudinal interaction [50–52]. In this work, we define longitudinal and transverse coupling rigorously via the interaction Hamiltonians $H_{\text{int}}^{\parallel}$ and $H_{\text{int}}^{\perp}$, corresponding to longitudinal or transverse fields for both resonator and TLS, respectively.

For superconducting qubits, operation in the dispersive regime often alleviates the need for non-perturbative longitudinal coupling, as other decoherence mechanisms typically prevail. Nonetheless, the challenges of measurement-induced transitions and Purcell decay continue to motivate research into longitudinal readout schemes [50–52] and recent insights into measurement-induced qubit transitions [155–157] emphasize the importance of non-perturbative longitudinal coupling. In contrast, the weaker coupling of spin systems renders the dispersive shift typically too small to resolve. As a result, spins are often coupled on resonance with the resonator, exploiting the transverse interaction (Eq. (1.11)) to enhance spontaneous emission into the cavity mode to boost the signal-to-noise ratio, known as Purcell enhancement [22, 40–43, 46, 47]. Even then, single-spin readout remains challenging and has only recently been demonstrated [22, 46].

As a result, these transverse spin-readout schemes are inherently demolishing and restricted to the resonator frequency, whereas non-perturbative longitudinal coupling avoids the drawbacks of transverse interaction, enabling frequency-independent, QND readout [50–52] even beyond the dispersive approximation (Eq. (1.13)). This thesis demonstrates such coupling for spin ensembles in Chapter 2 and scales it towards single-spin detection (Chapter 3), establishing a platform for robust QND spin readout.

2 Longitudinal Spin-Resonator Coupling: Ensemble Measurements

This chapter presents the first demonstration of longitudinal coupling between a molecular spin ensemble and the kinetic inductance of a grAl microwave resonator. We first situate our approach within existing kinetic inductance-based coupling schemes and evaluate its prospects for single-spin sensitivity. The spin ensemble polarization is encoded in the resonator frequency, independent of spin-resonator detuning, enabling full microwave readout of the magnetization curve. We further demonstrate time-resolved measurements of spin excitation and relaxation at GHz detuning from the readout. Finally, we discuss the challenges and scaling strategies towards single-spin detection. These results establish the foundation for the single-spin-sensitive architectures explored in the next chapter. This chapter is adapted in parts from Ref. [2].

2.1 Longitudinal Coupling via Kinetic Inductance

Kinetic inductance presents a promising platform to implement a longitudinal interaction between superconducting circuits and spins, since it can be modulated by magnetic fields or screening currents, e.g. induced by nearby spins. A well-established implementation is offered by superconducting quantum interference devices (SQUIDs), where the spin magnetic moment couples to the flux threading the superconducting loop, thereby modulating SQUID critical current [45, 159]. As outlined in Section 1.3.3, this effect maps to a modulation of the Josephson inductance in microwave circuits (cf. Eq. (1.8)).

While SQUID-based sensing has successfully demonstrated readout of the spin ensemble magnetization for direct current (DC) implementations, it exhibits several limitations in the context of longitudinal, quantum-compatible readout schemes: First, the DC readout induces local heating at the JJ, undermining the QND character of the longitudinal interaction. Incorporating such SQUIDs into microwave devices, however, introduces additional challenges: the intrinsic JJ nonlinearity introduces anharmonicity in the energy spectrum, limiting the power dynamic range of the system [160]. Furthermore, spin-flux coupling is limited for loop-based devices, which impedes the scaling towards single-spin readout [159]. The qualitative limitation arises from the loop's geometric sensitivity: only magnetic field lines that enclose the loop contribute to the net flux. Field lines that close internally within the loop are effectively canceled. Consequently, even if a spin is positioned directly above a nanoscale constriction with a width of tens of nm, the

effective spin–flux coupling remains limited, typically requiring $\sim 10^3$ magnetic moments to generate a detectable signal [159].

Disordered superconductors, such as NbN, NbTiN, InOx, and grAl, provide a more versatile source of kinetic inductance for longitudinal coupling [72, 91, 134–136, 138–140]. Such materials offer several key advantages compared to JJ-based devices:

- Intrinsic magnetic field susceptibility without requiring a loop geometry [139].
- High magnetic field resilience, maintaining low microwave losses even in Tesla-scale fields [5, 134–136, 138, 139].
- Amenable nonlinearity, tunable via the device geometry to values significantly lower than that of JJ-based devices [5, 72, 150].

Kinetic inductance magnetometers [161–163] leverage the strong current dependence of the kinetic inductance $L_{\mathrm{kin}}(I)$ in such disordered superconductors to convert an applied magnetic field through a superconducting loop into a measurable microwave-frequency shift. Consequently, they circumvent the heating and demolishing effects attributed to DC readout, marking a substantial advance towards QND detection. Nevertheless, these magnetometers still rely on screening currents in loop geometries, which ultimately constrain scalability to single-spin sensitivity, as discussed in the context of SQUIDs. Notably, longitudinal coupling of spins to a microwave device has yet to be demonstrated.

In the following section, we demonstrate longitudinal coupling between a spin ensemble and the kinetic inductance of a grAl resonator. By encoding the spin polarization directly into the resonator frequency, this approach enables measurement independent of the spin–resonator detuning. These ensemble-level measurements establish a proof-of-principle for kinetic inductance mediated longitudinal coupling, forming the foundation for future scaling to single-spin readout.

2.2 Kinetic Inductance Coupling to a Molecular Spin Ensemble

2.2.1 Implementation of Kinetic Inductance Coupling

Figure 2.1 illustrates the conceptual implementation of longitudinal coupling between a grAl resonator and a spin ensemble. The spin ensemble is realized using a single crystal of $\{Cr_7Ni\}$ magnetic molecules, which resemble cyclic wheels of eight chromium atoms, one of which is substituted by a nickel atom, as sketched in Fig. 2.1a. An antiferromagnetic exchange interaction between these metallic centers gives rise to a paramagnetic ground state of the molecule with a total spin $s = 1/2$ and g factor $g = 1.8$ [164–166]. The near-isotropic effective two-level structure avoids additional spectral contributions from higher energy levels and simplifies crystal alignment. Moreover, the deviation from $g = 2$ provides a distinct spectroscopic signature, facilitating discrimination from spurious coupling to extrinsic electronic spins in the environment of superconducting circuits [1, 134, 135, 139], making $\{Cr_7Ni\}$ an ideal choice for our experiment.

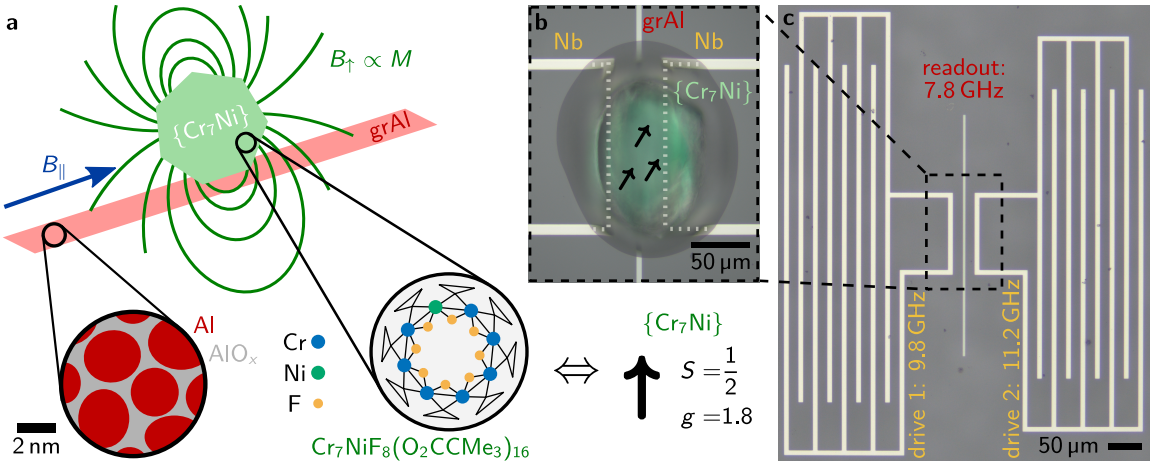

Figure 2.1: Kinetic inductance coupling between a grAl resonator and molecular spins. **a** Schematic of the spin-resonator system implementing a longitudinal interaction. The single crystal of {Cr_7Ni} magnetic molecules (green) is positioned at the center of a grAl stripline resonator (red). The ensemble magnetization M, due to polarization in an in-plane magnetic field $B_\parallel$, creates a local magnetic field $B_\uparrow$ (green lines) at the resonator site. This field increases the grAl kinetic inductance, implementing a longitudinal spin-resonator interaction. Left inset: The high kinetic inductance of grAl arises from its microstructure, consisting of crystalline aluminum grains (red) embedded in an amorphous AlO_x matrix. Right inset: The micro-crystal consists of single magnetic molecules $Cr_7NiF_8(O_2CCMe_3)_{16}$ ≡{Cr_7Ni}, where exchange interaction between Cr and Ni atoms results in a paramagnetic ground state with spin $s = 1/2$, $g = 1.8$ [164–166]. **b** Optical microscope image of the molecular crystal placed atop the grAl readout resonator (central strip). The crystal is attached and thermalized using *Apiezon N* [167] vacuum grease (transparent gray), which provides low levels of magnetic susceptibility and low microwave losses (cf. Section 4.1). For spin excitation, niobium resonators create radio-frequency (rf) magnetic fields perpendicular to the spin quantization axis (given by $B_\uparrow$). To ensure efficient coupling, their inductance is concentrated beneath the molecular crystal (dashed white outline). **c** Zoomed-out view of the grAl readout resonator, which operates at a resonance frequency of $f_r = 7.8\,\mathrm{GHz}$. It is flanked by two low-impedance niobium resonators, used to drive spins at $f_{\mathrm{Nb},1} = 9.8\,\mathrm{GHz}$ and $f_{\mathrm{Nb},2} = 11.2\,\mathrm{GHz}$. Adapted from Ref. [2].

The single crystal is attached at the center of the grAl stripline resonator using *Apiezon N* vacuum grease [167] ensuring thermal anchoring on the sapphire substrate (cf. Fig. 2.1b). The 500 µm long and 5 µm wide resonator (cf. Fig. 2.1c) has a fundamental resonance frequency of $f_r = 7.8\,\mathrm{GHz}$. The 20 nm thick grAl film is patterned on c-plane sapphire substrate and exhibits a sheet resistance of $R_\square = 1.1\,\mathrm{k\Omega/\square}$, corresponding to a sheet inductance of $L_\square = 0.9\,\mathrm{nH/\square}$. Due to its kinetic inductance fraction $\alpha \approx 1$ [72], we expect the longitudinal interaction via its kinetic inductance to dominate over the residual transverse coupling arising from the geometric inductance. However, the high impedance Z of the grAl resonator, which scales inversely with the transverse coupling strength $\tilde{g}^\perp \propto \delta B_r \propto 1/\sqrt{Z}$ [41, 152], renders it suboptimal for coherent spin driving. To address this, we integrate two low impedance niobium resonators on the same chip to drive the spins, as shown in Fig. 2.1b,c. Patterned from a 50 nm thick niobium film, these resonators support high current densities and are designed with 150 µm long inductor sections positioned in close vicinity to the center of the grAl readout resonator below the molecular crystal (cf. Fig. 2.1c). This co-localization facilitates efficient spin driving while preserving the high-impedance readout functionality of the grAl mode.

The longitudinal coupling arises from the interaction of the spin magnetic moment μ and the kinetic inductance L_{kin} of the grAl readout resonator. The total spin magnetization $\vec{M} = \sum_i \vec{\mu}_i$, which encodes an ensemble-averaged spin qubit population, modulates L_{kin} and induces a frequency shift δf_{M} of the resonator frequency f_{r}:

$$\delta f_{\mathrm{M}} / f_{\mathrm{r},0} \propto -M^2 \,. \tag{2.1}$$

This frequency shift results from the perpendicular component of the molecular crystal's magnetic field $B_{\uparrow,\perp} \propto M$, which induces local circulating (persistent) currents I_{p} in the grAl film. Note that, due to the large Pearl penetration depth Λ_{p} with respect to the resonator width w, $\Lambda_{\mathrm{p}} \gg w$, these currents do not significantly screen the magnetic field. Instead, they persist similarly to those in SQUIDs, which justifies denoting them as persistent currents I_{p}.

The kinetic inductance increases with these currents according to the expansion

$$L_{\mathrm{kin}}(I_{\mathrm{p}}) \approx L_{\mathrm{kin},0} \left(1 + \left(\frac{I_{\mathrm{p}}}{I^*} \right)^2 \right) , \tag{2.2}$$

where I^* characterizes the nonlinearity of the grAl film and is typically comparable to the critical current [161, 163, 168, 169]. In the regime of $\Lambda_{\mathrm{p}} \gg w$, the induced local currents scale linearly with the perpendicular magnetic field, $I_{\mathrm{p}} \propto B_{\uparrow}$, leading directly to the quadratic frequency shift described in Eq. (2.1). An additional, but negligible, contribution to the longitudinal coupling arises from the suppression of the superconducting gap with $B_{\uparrow}$. However, for our resonator geometry this effect is minimal and can be disregarded [139]. We emphasize that the operating principle of this longitudinal coupling scheme, where the spin-induced magnetic field perturbs the resonator's kinetic inductance via induction of local circulating currents, is conceptually analogous to that employed in kinetic inductance magnetometers [161–163] and kinetic inductance resonators in perpendicular magnetic field [139, 169].

2.2.2 Longitudinal Readout of Spin Ensemble Magnetization

We perform single-port reflection measurements of the sample in a dilution refrigerator at 30 mK, with the chip mounted in a circular sample holder placed inside a 3D vector magnet (see Appendix B.1). To verify the non-perturbative, detuning-independent nature of the longitudinal spin-resonator interaction, we measure the ensemble magnetization in parallel magnetic fields up to $B_{\parallel} = 0.6\,\mathrm{T}$, as shown in Fig. 2.2. In $B_{\parallel}$, the readout resonator frequency shift δf_{r} (Fig. 2.2a) consists of two contributions: (i) the frequency shift δf_{M} arising from the interaction with the spin ensemble and (ii) the intrinsic frequency shift $\delta f_{\mathrm{r}}(B_{\parallel}, M = 0)$ of the bare grAl resonator in $B_{\parallel}$.

While the perpendicular component of the spin-generated field $B_{\uparrow,\perp}$ governs the longitudinal coupling, we actively compensate the global perpendicular field when applying high $B_{\parallel}$, minimizing its influence (cf. Appendix B.2). Therefore, the prevailing effect on

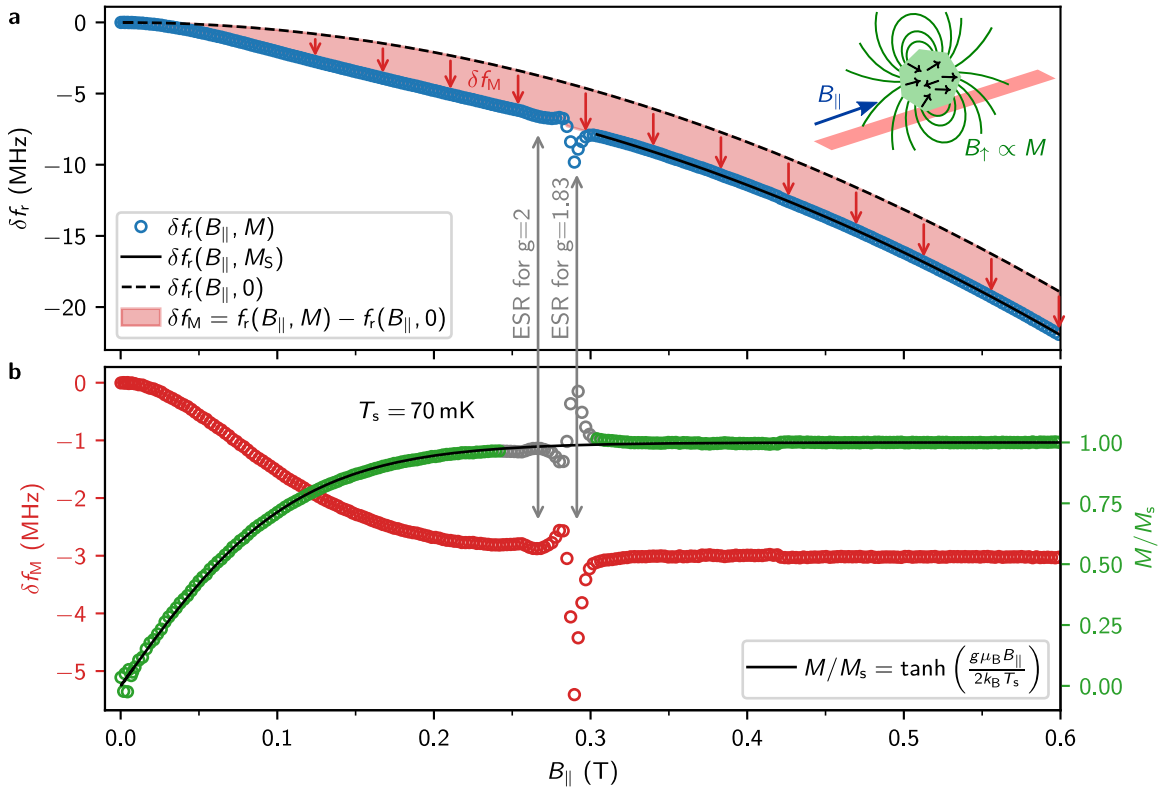

Figure 2.2: Detuning-independent readout of spin ensemble magnetization. **a** Resonance frequency shift $\delta f_r(B_\parallel, M)$ (blue markers) of the grAl readout resonator coupled to a molecular spin ensemble in an applied magnetic field $B_\parallel$. The quadratic shift $\delta f_r(B_\parallel, M = 0)$ (black dashed line) due to suppression of the superconducting gap in $B_\parallel$ [139] is superimposed by a shift δf_M (red arrows) induced by the crystal magnetic field $B_\uparrow$. A fit to the quadratic shift $\delta f_r(B_\parallel, M_S)$ for saturated crystal magnetization ($B_\parallel > 0.32$ T, black line) allows to separate the two contributions $\delta f_r(B_\parallel, M = 0)$ and δf_M. Transverse coupling of the $g = 1.83$ spins and spurious $g = 2$ ESR mode [1, 134, 135, 139] introduces additional hybridization-induced frequency modulations at $B_\parallel = 0.29$ T and $B_\parallel = 0.26$ T, respectively (gray arrows). **b** Extracted frequency shift δf_M (red), induced by the crystal magnetic field, and corresponding crystal magnetization $M \propto \sqrt{\delta f_M}$ (green). Residual transverse coupling with $g = 2$ and $g = 1.83$ spins prevents reliable extraction of the magnetization within the regions of hybridization-induced frequency shift (gray markers), which are therefore excluded from the fit to the paramagnetic response (black line). Note that the magnetization measurements were performed on a sample without Nb drive resonators in order to avoid field distortions (cf. Section 4.2). Adapted from Ref. [2].

the bare resonator becomes the suppression of the superconducting gap $\Delta(B_\parallel)$, leading to a parabolic decrease of the resonator frequency (see Ref. [139] and Section 4.2). To disentangle the two contributions, we fit the parabolic tail $\delta f_r(B_\parallel, M_S)$ for saturated crystal magnetization $M = M_S$ in the field range $B_\parallel > 0.32$ T. This allows to in-situ infer the intrinsic frequency shift $\delta f_r(B_\parallel, 0)$ in $B_\parallel$. Subtracting this reference from the total measured shift $\delta f_r(B_\parallel, M)$ isolates the contribution δf_M arising from the spin ensemble magnetization, as indicated by the red arrows in Fig. 2.2a.

In Fig. 2.2b, we show the extracted spin-induced frequency shift δf_M and the corresponding normalized magnetization $M/M_S = -\sqrt{\delta f_M / \delta f_M(M_S)}$ (cf. Eq. (2.1)). We observe a small hybridization-induced shift in δf_M due to the transverse coupling of the $g = 1.83$ spins to

the remaining geometric inductance of the resonator. This shift propagates to a distortion in the magnetization M. In addition, we detect a similar feature due to the coupling to spurious $g = 2$ paramagnetic impurities, which are commonly present in superconducting circuit environments and have been reported in prior resonator-based measurements [134, 135, 139]. These hybridization features become even more pronounced in the resonator's internal decay rate Γ_i and can be exploited as an in-situ determination of the g-factor and as a magnetic field calibration (see Section 4.1). In the subsequent quantitative analysis, we exclude data points where transverse hybridization significantly distorts the extracted magnetization M (gray points in Fig. 2.2b).

The crystal magnetization is expected to follow the paramagnetic response

$$M = M_S \tanh\left(\frac{g\mu_B B_\parallel}{2k_B T_S}\right), \tag{2.3}$$

where k_B is the Boltzmann constant and T_S denotes the spin temperature. Indeed, a fit to Eq. (2.3) is in good agreement with the extracted magnetization M for $T_S = 70\,\mathrm{mK}$, confirming the detuning-independent nature of the spin-superconductor interaction. Interestingly, the fitted spin temperature exceeds the cryostat base temperature $T \approx 30\,\mathrm{mK}$, indicating limited thermalization of the molecular crystal through the vacuum grease (cf. Fig. 2.1). Subsequent cooldowns with smaller crystal led to spin temperatures of $T_S = 30\,\mathrm{mK}$, foreshadowing limited spin-phonon relaxation, denoted phonon-bottleneck regime [95].

2.2.3 Spin Excitation and Decay

While the previous section focused on passive magnetization measurements, arising from thermal spin polarization under increasing Zeeman splitting in $B_\parallel$, we now demonstrate active spin manipulation, as shown in Fig. 2.3. Owing to the detuning-independence of the longitudinal readout scheme, we measure the spin polarization while exciting the spin ensemble at a frequency 2 GHz detuned from the grAl readout mode. Specifically, we use the low-impedance niobium drive resonator at $f_{\mathrm{Nb1}} = 9.84\,\mathrm{GHz}$. Figure 2.3a shows continuous-wave (CW) two-tone (TT) spectroscopy on the spin ensemble, measured by continuously monitoring the readout resonator response while applying a second microwave tone f_d with varying frequency. The measured shift in the readout frequency δf_r, corrected for cross-Kerr interactions between the drive and readout modes (cf. Section 4.3), is converted into a relative magnetization change of the ensemble $\delta M/M_S$ using a previously calibrated magnetization curve for the same molecular crystal (cf. Fig. 4.3). As expected, we observe the spin transition frequency $hf = g\mu_B B_\parallel$ tuning through f_{Nb1}, from which we extract $g = 1.83 \pm 0.01$, consistent with values reported in Refs. [164, 166]. The excitation pattern reflects a convolution between the Lorentzian linewidth of the Nb drive resonator with the inhomogeneous spin ensemble linewidth. The former determines the magnitude of the radio-frequency (rf) field at the spin position while the latter determines the effective fraction of resonant spins. Importantly this experiment also serves as a control: when the spin transition is far detuned from the drive (e.g. at $B_\parallel = 0.36\,\mathrm{T}$ in Fig. 2.3a), no measurable

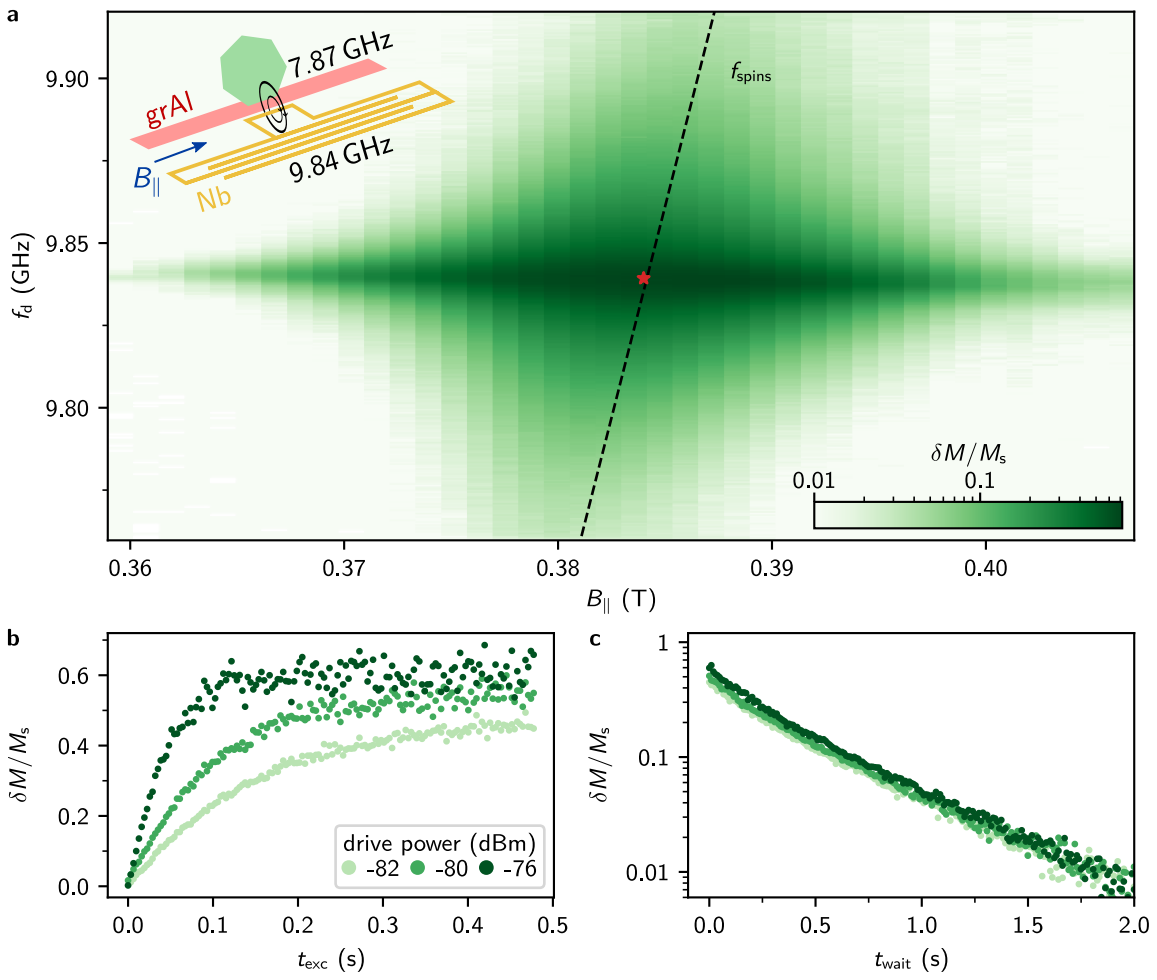

Figure 2.3: Excitation and decay of the spin ensemble 2 GHz detuned from the readout. **a** Continuous-wave two-tone spectroscopy of the spin ensemble, performed by sweeping a second drive tone f_d in the vicinity of the niobium resonator frequency $f_{Nb1} = 9.84$ GHz while monitoring the readout resonator response at $f_r = 7.87$ GHz. The relative shift of the spin magnetization $\delta M/M_S$ (green color bar) is measured from the saturation and calibrated to the respective frequency shift δf_r utilizing a magnetization curve similar to Fig. 2.2 (cf. Section 4.2). The dashed line indicates the center frequency $hf = g\mu_B B_\parallel$ of the spin distribution, with $g = 1.83$. The excitation is most effective when the ESR is within the $\kappa/2\pi = 2$ MHz bandwidth of the Nb resonator. **b, c** Time-domain characterization of the spin ensemble at $B_\parallel = 0.384$ T, in resonance with the Nb drive (red marker in **a**). **b** Excitation to saturation and **c** decay from saturation of the spins for different incident drive powers. Note the non-exponential relaxation with a $1/e$ time of $\tau = 0.38$ s. Adapted from [2].

change in magnetization occurs, excluding drive induced heating as origin of the spin excitation.

We complete the spin ensemble characterization with time-resolved excitation and decay measurements on resonance with the niobium drive in Fig. 2.3b,c. As expected, we observe drive power dependent excitation dynamics, reaching a saturation level of $\delta M/M_S = 0.6$ for the highest drive powers (cf. Fig. 2.3b). After ensuring a steady state excitation by driving the spins for $t_{exc} = 6$ s, the ensemble relaxation exhibits a non-exponential decay, with a $1/e$ decay time of $\tau = 0.38$ s (cf. Fig. 2.3c). This decay time is two orders of magnitude longer than previously reported lifetimes for the same $\{Cr_7Ni\}$ molecules in toluene solution [165],

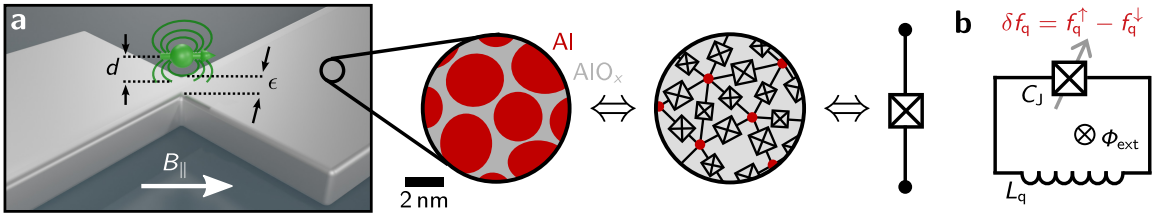

Figure 2.4: Towards a superconducting kinetic inductance element, susceptible to single spins. **a** Sketch of a single spin (green) at a distance d on top of a superconducting thin film in a magnetic field $B_{\parallel}$. The superconductor is locally confined to a nanoscopic volume by confining the width ϵ, to increase the interaction with the spin's magnetic dipole field (green lines). Inset: microstructure of grAl, consisting of crystalline aluminum grains within amorphous oxide [140], forming a 3D network of JJs. The chemical similarity to conventional Al/AlO_x/Al JJs makes grAl a promising candidate for a low-loss nanoscopic JJ. **b** Circuit diagram of a superconducting fluxonium qubit with spin-state-dependent Josephson energy E_J, junction capacitance C_J, superinductor L_q and external flux Φ_{ext}. The exponential sensitivity of the fluxonium transition frequency f_q on E_J implements a frequency shift δf_q depending on the spin polarization. Adapted from [2] and [170] with permission from the author.

indicating that decay is limited not by intrinsic spin-phonon relaxation but by phonon decay into the substrate, commonly referred to as phonon-bottleneck [95]. In this regime, the limited number of phonon modes at the spin transition energy, combined with inefficient phonon-phonon interactions (preventing efficient excitation redistribution into the other modes), leads to a high population of the respective phonon mode for spin relaxation. Combined with poor thermal coupling to the substrate bath, the resulting slow phonon decay significantly prolongs the relaxation time of the spin ensemble.

The phonon-bottleneck is a prime example for ensemble-level effects that modify the spin relaxation and coherence dynamics, alongside inhomogeneous broadening and spin-spin interactions. While the presented results demonstrate the utility of longitudinal spin-resonator coupling and validate its implementation via kinetic inductance, they also emphasize a key limitation: QIP requires precise, coherent control over individual spins, rather than ensembles. Consequently, these measurements establish both the promise and limitations of ensemble-based protocols and motivate the transition to single-spin readout.

2.3 From Ensembles to Individual Spins: Scaling Longitudinal Coupling

A longitudinal single-spin interaction governed by $H_{\text{int}}^{\parallel}$ (cf. Eq. (1.14)) corresponds to coupling a superconducting circuit to the static dipolar field of an individual spin. Even for magnetic molecules with large moments ($\mu \sim 10\mu_B$), this dipole field remains weak and highly localized: $B_{\text{dipole}}(1\,\text{nm}) = 18.5\,\text{mT}$ and $B_{\text{dipole}}(10\,\text{nm}) = 18.5\,\mu\text{T}$, for distances of $d = 1\,\text{nm}$ and $d = 10\,\text{nm}$ along the z-axis, respectively. Consequently, the perturbation induced by a single spin is negligible when averaged over the micron scale of a conventional grAl resonator. To enable single-spin detection, it is therefore essential to concentrate the

kinetic inductance into a nanoscopic volume. However, this volume reduction inherently increases the device nonlinearity [150], which results in an anharmonic circuit with limited power dynamic range [148], effectively transforming it into a superconducting qubit with direct fluorescent readout [148, 160]. To overcome these readout limitations, we can adopt the conventional readout strategy for superconducting qubits, i.e. coupling the spin-sensitive qubit circuit to a harmonic readout circuit. With the spin-state encoded into the superconducting qubit frequency, this allows to precisely determine its frequency via Ramsey interferometry, where readout fidelity and coherence time define the frequency resolution. This reframes the challenge of single-spin readout as the precise detection of a superconducting qubit frequency shift. The key requirement, illustrated in Fig. 2.4, is then a nanoscopic JJ to implement a kinetic inductance sensitive to the spin dipole field.

In practice, the majority of JJs in superconducting qubits are implemented in the form of Al/AlO_x/Al overlap JJ due to their long list of advantages, which include: i) robust fabrication of the oxide barrier [171], ii) robustness to thermal cycling [172], and iii) unmatched coherence [101, 172, 173], which directly impacts the frequency resolution in a Ramsey experiment for spin detection. While typical JJs used in QIP with electrode sizes down to $100 \times 100\,\mathrm{nm}^2$ offer reproducibly low area variation [174], sizes can be reduced to $20 \times 30\,\mathrm{nm}^2$ [114]. However, these aluminum-based JJs are incompatible with the high magnetic fields required for spin-qubit operation. Their performance degrades due to the suppression of the superconducting gap Δ at $\sim 10\,\mathrm{mT}$ in bulk and the diminishing of the JJ critical current in a Fraunhofer interference pattern [175].

While the use of aluminum in the thin film limit can improve magnetic field compatibility [148, 175–177], measured devices still report significant suppression of the qubit frequency and coherence in the range of 10^1–$10^2\,\mathrm{mT}$. An alternative approach towards field resilience in JJs are gate tunable junctions based on semiconducting nanowires [125, 178–183] and graphene [184],which avoid Fraunhofer interference by omitting overlapping electrodes. However, their performance is limited by significant spectral instability and poor coherence. Other weak links that avoid Fraunhofer interference are Superconductor-constriction-Superconductor (ScS) JJs, where the nonlinearity directly originates from a continuous superconducting film [92]. Patterned from field-resilient superconductors like niobium, these JJs are well characterized in DC measurements [185] and have been used to probe magnetization dynamics of magnetic molecules [159]. Yet, the high critical current of niobium nanobridges impedes their use in superconducting qubits [91] and JJ implementations using disordered superconductors have shown marginal coherence, even in zero magnetic field [131–133, 137, 186].

To overcome these limitations, we aim to engineer a novel type of weak link that combines the advantageous coherence of standard Al/AlO_x/Al junctions with the field resilience of disordered superconductors and the nanoscopic footprint of ScS weak links. The granular microstructure of grAl offers a notable difference to atomically disordered superconductors like NbN, InO and NbTiN: Composed of crystalline aluminum grains inside an insulating AlO_x matrix [140–142], its microstructure effectively implements a 3D network of nanoscopic JJs (cf. Fig. 2.4a). Notably, this effective JJ model, governed by inter-grain Josephson coupling, remains valid down to dimensions on the order of tens of nanometers

due to the small coherence length, approaching the grain size in the strongly disordered limit [187]. Moreover, the intriguing chemical similarity to standard Al/AlO_x/Al JJ suggests its potential for coherent operation. Indeed, grAl resonators demonstrate low dissipation (cf. Section 4.1), with internal quality factors of $Q_\mathrm{i} \sim 10^5$–10^6 in the single photon regime [72, 124, 145, 146] and its magnetic field resilience [4, 139] makes it a suitable candidate for hybrid architectures, as we have demonstrated in the previous section. We thus conclude that a promising approach for longitudinal single-spin coupling consists of a nanoscopic confinement of granular aluminum to implement a coherent JJ. The proposed interaction mechanism exploits the modulation of the superconducting gap Δ by the spin dipole field $\Delta(B_\uparrow)$, resulting in a spin-state-dependent Josephson energy $E_\mathrm{J} \propto \Delta(\sigma_z)$. Note that, in contrast to the mechanism for ensemble measurements presented in Section 2.2.1, the contribution from circulating currents is negligible due to the small cross section of the grAl junction.

To detect spin-dependent shifts $\delta E_\mathrm{J} = E_\mathrm{J}^\uparrow - E_\mathrm{J}^\downarrow$, the junction must be embedded in a coherent superconducting circuit for high-resolution qubit frequency readout. While the transmon qubit frequency depends on E_J only in a square root dependence, $\hbar\omega_\mathrm{q} = \sqrt{8E_\mathrm{J}E_\mathrm{C}} - E_\mathrm{C}$ [48], the fluxonium frequency at the half-flux sweet spot exhibits exponential sensitivity to changes in E_J due to the tunneling through the Josephson barrier in the potential. The fluxonium transition frequency can be approximated by the phase-slip rate ν [188, 189]

$$\nu = \frac{4}{\sqrt{\pi}} \left(8E_\mathrm{J}^3 E_\mathrm{C}\right)^{1/4} e^{-\sqrt{8E_\mathrm{J}/E_\mathrm{C}}} . \tag{2.4}$$

Consequently, we propose to embed the grAl junction into a fluxonium superconducting qubit (cf. Fig. 2.4b), governed by the standard fluxonium Hamiltonian H_flux (Eq. (1.7)). Since $[H_\mathrm{flux}, \sigma_z] = 0$, this implements a longitudinal single-spin interaction.

3 Probing Spins with a Superconducting Qubit: Sensing in High Magnetic Fields

Building on the demonstration of longitudinal coupling between superconducting circuits and spin ensembles in Chapter 2, this chapter advances the narrative towards achieving longitudinal coupling to individual spins. We introduce and develop the gralmonium qubit – a novel granular aluminum nanojunction-based fluxonium qubit specifically designed for single-spin detection. By confining the Josephson element to nanoscopic dimensions while maintaining coherence, the gralmonium addresses the challenge of enhancing spin sensitivity without sacrificing qubit stability. Our measurements show that the qubit spectrum and coherence are indistinguishable from conventional fluxonium qubits incorporating SIS-based JJs, allowing circuit engineering based on a simple, established model Hamiltonian. To enable operation in the Tesla regime required for spin qubit experiments, we implement a gradiometric qubit design. Through systematic characterization at zero and high magnetic fields up to 1 T, we quantify the gralmonium's resilience, coherence, and sensitivity to spin-induced perturbations within the nanojunction volume. Furthermore, probing the qubit environment for spin-specific signatures in high magnetic fields establishes its readiness for hybrid architectures integrating single spins. A simulation of spin-flip-induced frequency shifts confirms that, under realistic conditions, a single magnetic molecule placed atop the nanojunction produces a resolvable qubit frequency shift through longitudinal interaction, validating the feasibility of longitudinal single-spin detection with the gralmonium. This chapter is adapted in parts from Refs. [1–3].

3.1 Gralmonium: A Superconducting Qubit for Single Spin Detection

3.1.1 The GrAl Nanojunction

As discussed in Section 2.3, achieving longitudinal coupling to an individual spin requires a novel type of weak link: a nanoscopically confined grAl element. To maximize sensitivity to a single spin, the element must be as small as possible while maintaining acceptable fabrication reproducibility and yield. Additionally, when integrated into a qubit circuit, the structure must retain coherence, as the qubit frequency — encoding the spin state — is determined via Ramsey interference experiments.

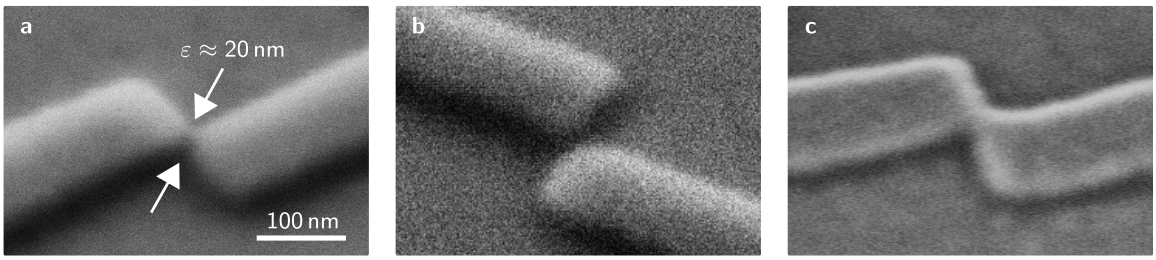

Figure 3.1: The grAl nanojunction. Scanning electron microscope (SEM) image of three grAl nanojunctions with nominally identical design. **a** Two grAl electrodes connected by an $\varepsilon^3 \approx (20\,\mathrm{nm})^3$ grAl volume, forming a grAl nanojunction. About one in four fabricated nanojunctions forms a connection with $\varepsilon \leq 25\,\mathrm{nm}$. **b** Example of a disconnected nanojunction. **c** Junction with an excessively wide connection, $\varepsilon \approx 50\,\mathrm{nm}$, exceeding the design specification. The scalebar in **b** and **c** is identical to that in **a**. Note that, for a 3D perspective on the nanojunction, the imaging was performed under an angle of 45° (**a, b**) and 28° (**c**).

We fabricate the grAl element using a well-established lift-off lithography process on sapphire substrates in order to maintain the low microwave losses obtained in grAl resonator measurements (cf. Section 4.1). Compared to silicon and other substrates, sapphire is a reliable and common substrate that offers low microwave losses [84] without requiring complex surface passivation or removal processes to maintain interface quality [91]. However, electron-beam lithography on insulating sapphire poses challenges due to charge accumulation, which generates local electric fields that distort and deflect the beam, reducing the resolution even when antistatic coatings are applied (cf. Appendix A.2). By refining the lithography to accommodate narrow wire confinement and explicitly accounting for the proximity effect beyond standard correction algorithms, we reliably achieve grAl feature sizes down to $\varepsilon \approx 20\,\mathrm{nm}$, as illustrated in Fig. 3.1a. Despite these optimizations, the fabrication yield remains limited: approximately one in four nominally identical structures results in a lateral grAl confinement below $\varepsilon \leq 25\,\mathrm{nm}$, while others are either discontinuous (Fig. 3.1b) or excessively wide (Fig. 3.1c). In the following, we denote grAl structures with confinement to an $\varepsilon^3 \approx (20\,\mathrm{nm})^3$ volume as **grAl nanojunctions** and focus our development of longitudinal single-spin coupling on these elements due to their favorable scale.

To incorporate the grAl nanojunction into superconducting quantum circuits and engineer the associated circuit elements, it is essential to estimate its nonlinearity. So far, the kinetic inductance nonlinearity in disordered superconductors has been modeled using a leading-order expansion (cf. Eq. (2.2)). However, this approximation becomes inadequate for the nanojunction, where strong geometric confinement enhances the nonlinearity and renders higher-order terms significant. In the case of grAl, the microwave nonlinearity has been analytically described by modeling the film as an effective 1D JJ array. The resulting self-Kerr coefficient K_{11} (quantifying the frequency shift per photon) scales inversely with the grAl volume V_{grAl} as $K_{11} \propto \omega_1^2/(j_c V_{\mathrm{grAl}})$, where ω_1 is the fundamental mode frequency of a rectangular strip of grAl [150]. Remarkably, this simple volume-scaling law agrees with experimental measurements over six orders of magnitude in K_{11}, without the need for fitting parameters. The observed increase in nonlinearity with decreasing volume thus strongly supports the enhanced nonlinearity of the nanojunction relative to standard grAl

elements. However, similar to the kinetic inductance expansion, the self-Kerr coefficient represents a first-order approximation of the nonlinearity. For a more complete model, we treat the nanojunction as an effective JJ, characterized by a critical current I_c and corresponding Josephson energy E_J.

In conventional fluxonium qubits, the nonlinearity arises from tunnel JJs with typical Josephson energies of $E_J/h \sim 10^1$ GHz and a nonlinearity determined by $E_J/E_C \sim 1$ [91], which reflects the extent to which the phase particle in the fluxonium potential probes the nonlinearity of the EφR. To employ the nanojunction as the dominant nonlinear element in a fluxonium qubit, we estimate its effective E_J. Extending the analogy between Josephson inductance and kinetic inductance of disordered superconductors described within the framework of the Mattis-Bardeen theory (cf. Section 1.3.3), we model the nanojunction as a 20 nm × 20 nm square of a 20 nm-thick disordered superconductor with sheet inductance $L_\square = 2\,\mathrm{nH}/\square$ (corresponding to a grAl resistivity of $\rho = 4000\,\mu\Omega\,\mathrm{cm}$ [72]). This yields a critical current $I_c = 165$ nA and corresponding Josephson energy $E_J/h = 82$ GHz, based on the relation for Josephson inductance L_J (Eq. (1.8)). This estimate is corroborated by critical current densities extracted from switching current measurements on grAl micro-SQUIDs with 20 nm × 80 nm × 300 nm constrictions [190, 191], which for a grAl resistivity of $\rho = 3200\,\mu\Omega\,\mathrm{cm}$ yield $E_J/h = 70$ GHz for nanojunction-sized constrictions. These results place the nanojunction within the fluxonium regime $E_J/E_C \sim 1$ for an expected junction capacitance on the order of $C \lesssim 1$ fF ($E_C \gtrsim 19$ GHz), when fabricated from high-resistivity grAl films (e.g. $\rho = 3000\,\mu\Omega\,\mathrm{cm}$).

Beyond its Josephson energy, the nonlinearity of a JJ is governed by its CφR. For constriction-type JJs, the CφR typically deviates from a sinusoidal form, depending sensitively on the constriction geometry and the distribution of transmission channels (cf. Section 5.2) [92]. The grAl microstructure, however, can also be modeled as a three-dimensional network of tunnel JJs with sinusoidal CφR, akin to that of conventional superconductor-insulator-superconductor (SIS) junctions. The nanojunction, therefore, tests the boundaries of existing models for grAl nonlinearity, bridging the gap between a material-based description and a JJ-based framework. The fluxonium qubit offers an ideal testbed to experimentally probe the nanojunction CφR. Its flux-tunable energy spectrum enables fine control of the potential landscape, while its pronounced anharmonicity and characteristic tunnel regime $E_J/E_C \sim 1$ render it highly sensitive to the functional form of the CφR, facilitating a direct probe of the nanojunction's nonlinearity at the most fundamental level.

3.1.2 Gralmonium: Granular Aluminum Nanojunction Fluxonium Qubit

In light of the previous considerations, we integrate the grAl nanojunction as a strongly nonlinear element into a superconducting fluxonium qubit circuit. The previously demonstrated performance of grAl resonators [4, 72, 145, 146] and grAl superinductors in fluxonium architectures [124] combined with the grAl nanojunction now allows to design all circuit elements for qubit and readout from a single grAl film. By tailoring the geometry of the grAl structures, we engineer distinct circuit functionalities, thereby enabling fabrication of the entire device in a single lithographic layer. This monolithic architecture, which

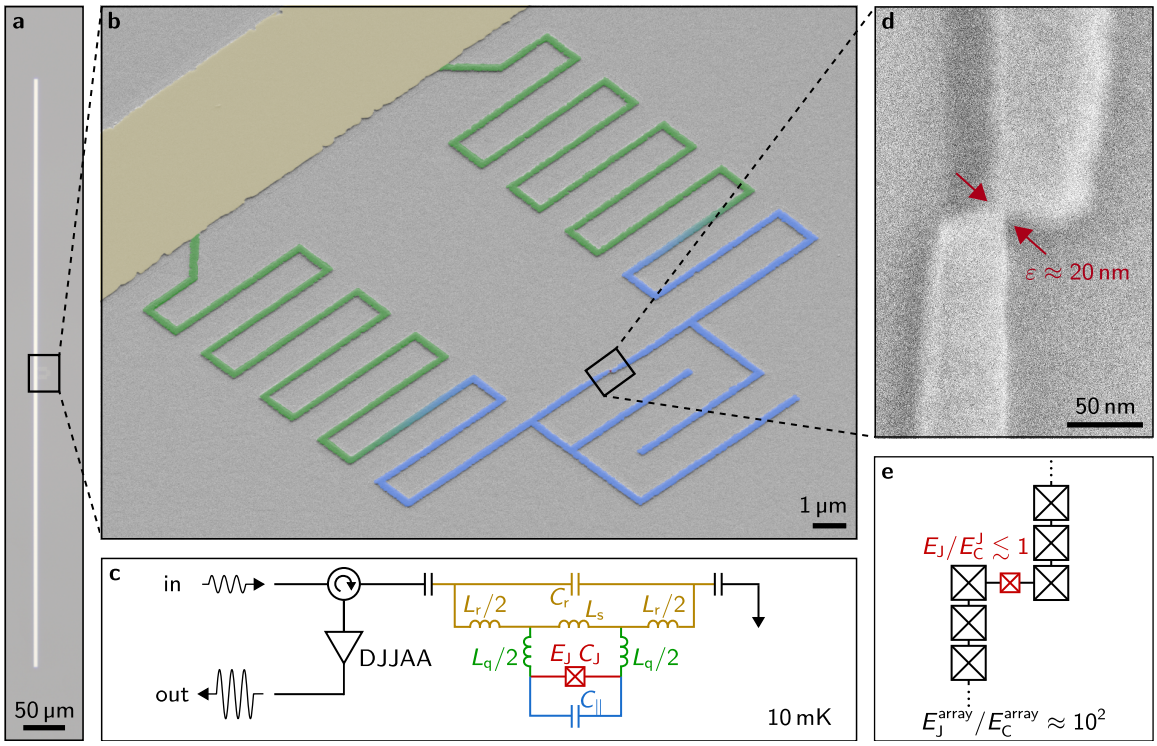

Figure 3.2: The gralmonium: a single-layer granular aluminum fluxonium qubit. **a** Optical micrograph of the grAl stripline antenna, serving as a readout resonator for the gralmonium attached in its center. **b** False-colored SEM zoom-in on the gralmonium qubit circuit. The readout antenna (ocher) is galvanically connected to the qubit, which consists of a meandered grAl superinductor (green) and a grAl nanojunction (red) shunted by an interdigitated capacitor (blue). The green-to-blue gradient indicates inductive-to-capacitive contributions from the meanders, reflecting the compact circuit layout. The entire structure is fabricated in a single-layer without overlapping contact junctions. **c** Lumped-element circuit diagram corresponding the circuit in **b**: The readout resonator, consisting of capacitance C_r and inductance L_r, is inductively coupled via a shared inductance L_s to the qubit. The qubit includes an inductance L_q, a shunt capacitance $C_\parallel$, and a Josephson junction characterized by Josephson energy E_J and intrinsic capacitance C_J (charging energy E_C^J). The circuit is measured in single-port-reflection within a cylindrical copper waveguide sample holder (cf. Appendix B.1) using a Dimer Josephson Junction Array Amplifier (DJJAA) [192]. **d** SEM zoom-in on the grAl nanojunction, formed by laterally confining the grAl wire to a width of $\varepsilon \approx 20$ nm (cf. Fig. 3.1). **e** Circuit model of the nanojunction enclosed by the superinductor in **d**, forming an effective 1D Josephson junction array with spatially modulated Josephson coupling E_J/E_C. Adapted from Ref. [3].

we refer to as gralmonium, offers multiple advantages. Most notably, it eliminates the need for overlap junctions, thereby avoiding the emergence of Fraunhofer interference patterns that typically arise in high magnetic fields, necessary for spin qubit operation. Consequently, the gralmonium design not only incorporates a nanoscopic nonlinear element designed for single-spin detection but also promises to enhance magnetic field resilience compared to conventional superconducting qubit circuits [176].

Figure 3.2 shows the implementation and the corresponding lumped-element circuit diagram of the gralmonium. The circuit is patterned from a 20 nm-thick grAl film with a sheet resistance of $R_\square = 1.5\,\mathrm{k\Omega/\square}$, deposited on a sapphire substrate (see Appendix A.2). The readout resonator is implemented as a 4 µm-wide stripline antenna (cf. Fig. 3.2a)

with the fluxonium qubit located in its center (Fig. 3.2b). Qubit-resonator coupling is mediated via a galvanic connection between the qubit loop and the resonator, which share 8 µm of the resonator inductance, similar to the design in Refs. [121, 124]. We model the entire circuit using a lumped-element representation, illustrated in the circuit schematic in Fig. 3.2c. The qubit loop is formed by a 170 nm wide meandered grAl superinductor, which is closed by locally constricting the grAl wire to a width of $\varepsilon = 20\,\mathrm{nm}$, forming the ε^3 grAl volume that defines the grAl nanojunction (cf. Fig. 3.2d and Section 3.1.1).

Given the coherence length of our grAl film of $5\,\mathrm{nm} < \xi < 10\,\mathrm{nm} < \varepsilon$ [141, 193, 194], the nanojunction does not constitute a conventional constriction-type JJ, which requires both the width and length of the constriction to be on the order of, or smaller than, the superconducting coherence length [92]. Instead, considering the grAl microstructure composed of aluminum grains with an an average grain size of $\approx 4\,\mathrm{nm}$ [140–142], we model the nanojunction as a three-dimensional network of tunnel JJs. For operating frequencies well below the grAl plasma frequency ($\approx 70\,\mathrm{GHz}$ [143, 150]), this 3D JJ network in the nanojunction and the connecting wire of the grAl superinductor can be effectively modeled as a one-dimensional JJ array with abruptly modulated Josephson coupling strength of magnitude E_J at the position of the nanojunction (cf. Fig. 3.2e). While potentially several successive Al/AlO_x interfaces within the nanojunction contribute to electrical transport, we model it as an effective single SIS JJ, characterized by a capacitance C_J and effective Josephson energy E_J with sinusoidal CφR.

In this effective model, not only the Josephson coupling but also the capacitance changes considerably due to the change in wire crossection from the distributed superinductor array to the nanojunction. Specifically, the grAl superinductor operates in the regime $E_\mathrm{J}^\mathrm{array}/E_\mathrm{C}^\mathrm{array} \approx 10^2$, while the nanojunction enters the regime $E_\mathrm{J}/E_\mathrm{C}^\mathrm{J} \lesssim 1$. To engineer the desired fluxonium energy spectrum, we shunt the nanojunction with an interdigitated capacitor (highlighted in blue in Fig. 3.2b,c) with capacitance $C_\parallel \approx 0.8\,\mathrm{fF}$ obtained from finite element simulations. This additional shunt introduces an upper bound for the gralmonium charging energy $E_\mathrm{C} = e^2/(2(C_\mathrm{J} + C_\parallel)) \lesssim E_\mathrm{C}^\parallel = e^2/(2C_\parallel) \approx 24\,\mathrm{GHz}$, bringing the gralmonium into the regime $E_\mathrm{C} \approx E_\mathrm{J}$. Note that due to the compact geometry of the superinductor loop, the meanders in the vicinity of the nanojunction contribute to the shunt capacitance $C_\parallel$, which is qualitatively illustrated by a green-to-blue color gradient in Fig. 3.2b.

3.1.3 Gralmonium Qubit: Exceptionally Unexceptional

We characterize the gralmonium device shown in Fig. 3.2 in a dilution refrigerator at a base temperature of 10 mK, mounted within a sub-wavelength copper sample holder (cf. Appendix B.1). The readout resonator is measured in single-port microwave reflection employing a parametric amplifier to enhance signal-to-noise ratio [192]. Illustrated in Fig. 3.3a, avoided level crossings in the resonator phase response measured as a function of external magnetic flux provide the first indication of a functional gralmonium device. These avoided crossings reflect the coherent transverse coupling between the fluxonium qubit and

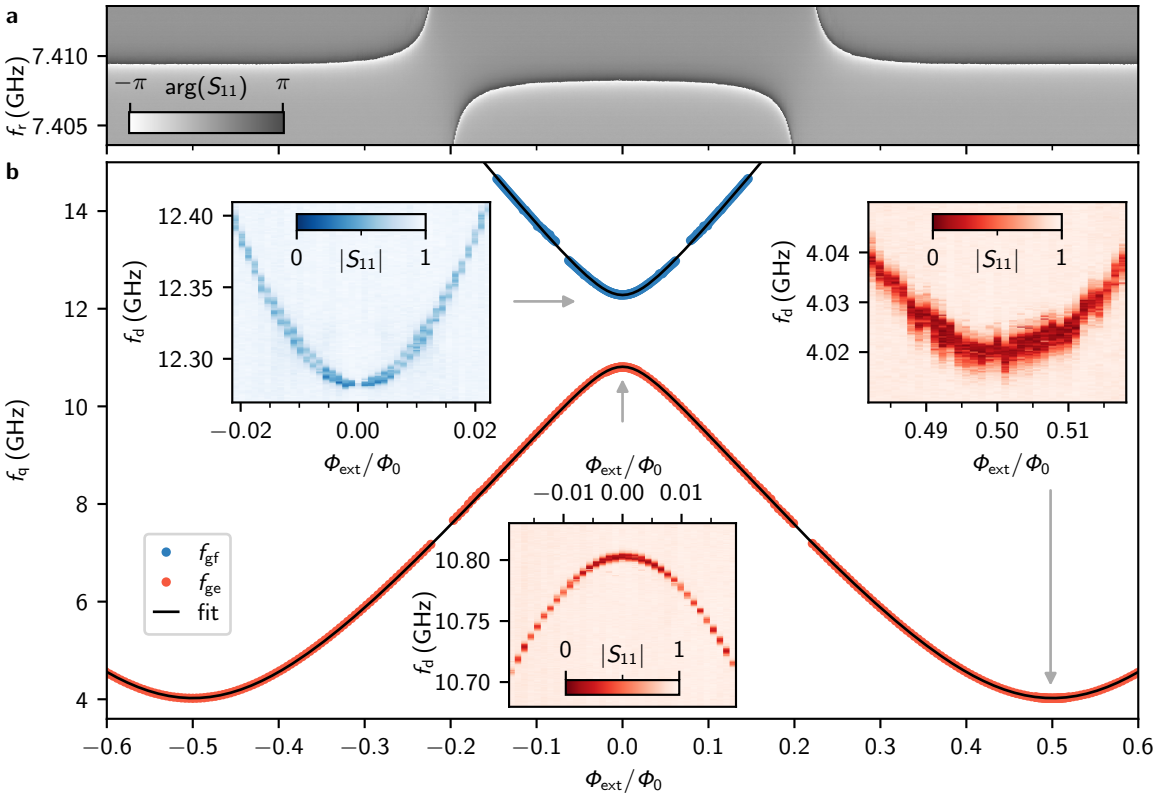

Figure 3.3: Gralmonium Spectroscopy. **a** Phase response $\arg(S_{11})$ of the readout resonator as a function of external magnetic flux Φ_{ext}, measured in single-port reflection. Avoided level crossings appear in the flux sweep at small qubit-resonator detuning, indicating a periodic modulation of the qubit frequency (cf. Fig. 5.1). **b** Gralmonium spectrum vs. external flux, extracted from continuous-wave two-tone spectroscopy. The markers show the fluxonium transitions from $|g\rangle \rightarrow |e\rangle$ (red) and $|g\rangle \rightarrow |f\rangle$ (blue). Hybridization with the readout resonator near 7.4 GHz and with the first mode of the grAl superinductor around 13.1 GHz prevents reliable extraction of the qubit frequency, resulting in gaps in the extracted spectrum. From a fit (black lines) of the fluxonium Hamiltonian H_{flux} (cf. Eq. (1.7)) to the spectrum, we extract $E_L/h = 0.574$ GHz (i.e. inductance $L_q = 285$ nH), $E_J/h = 23.4$ GHz (i.e. critical current $I_c = 47.1$ nA) and $E_C/h = 15$ GHz (i.e. total qubit capacitance $C_q = C_{\parallel} + C_J = 1.26$ fF) for the qubit parameters (cf. Fig. 3.2). **Insets:** Raw two-tone spectroscopy trace measured at $\Phi_{ext}/\Phi_0 = 0$ (top left and bottom) and $\Phi_{ext}/\Phi_0 = 1/2$ (top right), acquired by applying a second drive tone at frequency f_d while monitoring the readout resonator response, encoded in the amplitude of the reflection coefficient $|S_{11}|$ (color scale). As expected from fluxonium selection rules [99, 101, 122], the $|g\rangle \rightarrow |f\rangle$ transition vanishes in the vicinity of $\Phi_{ext} = 0$ (top left inset) At half-flux $\Phi_{ext}/\Phi_0 = 1/2$ (top right inset), the qubit frequency toggles between traces, i.e. on minutes timescale. Adapted from Ref. [3].

the readout resonator, and are absent in devices where the nanojunction is either discontinuous or excessively wide (cf. Section 5.1). Given the limited fabrication yield associated with the nanojunction's nanoscale confinement (cf. Section 3.1.1), these measurements are particularly valuable as a practical screening method for identifying operational devices. It is important to note that SEM imaging is performed only after cryogenic measurements, as carbon deposition during SEM can degrade qubit performance. This precludes SEM as a reliable method for pre-selecting functional nanojunctions. Importantly, the periodic repetition of the avoided level crossings with magnetic flux (cf. Section 5.1) confirms the periodic modulation of the fluxonium transition frequency across the resonator frequency. This allows to distinguish the system response from spurious modes coupled to

the resonator, induced for example by exceeding the geometry-dependent threshold for out-of-plane magnetic fields within the cooldown [139] (cf. Appendix B.2).

We further characterize the gralmonium by performing continuous-wave (CW) two-tone (TT) spectroscopy, acquired by applying a second drive tone at frequency f_d while monitoring the readout resonator response. The resulting gralmonium spectrum, shown in Fig. 3.3b up to 14 GHz, reveals $|\mathrm{g}\rangle \rightarrow |\mathrm{e}\rangle$ transition frequencies of $f_\mathrm{ge} = 4.0\,\mathrm{GHz}$ and $f_\mathrm{ge} = 10.8\,\mathrm{GHz}$ at the half-flux and zero-flux sweet spot, respectively. The overall structure closely resembles that of conventional fluxonium qubits [6, 99, 101, 122–124], indicating that the grAl nanojunction embedded within the gralmonium circuit retains conventional fluxonium characteristics. In particular, the suppression of the $|\mathrm{g}\rangle \rightarrow |\mathrm{f}\rangle$ transition near zero flux (see top-left inset in Fig. 3.3b) is consistent with fluxonium selection rules [99]. We model both the extracted $|\mathrm{g}\rangle \rightarrow |\mathrm{e}\rangle$ and $|\mathrm{g}\rangle \rightarrow |\mathrm{f}\rangle$ transition simultaneously, utilizing a numerical diagonalization of the fluxonium Hamiltonian (Eq. (1.7)). The agreement between the fit (black line in Fig. 3.3b) and the extracted qubit spectrum confirms that Eq. (1.7) accurately describes the gralmonium circuit. In total, we spectroscopically characterized more than 20 working gralmonium devices based on the qubit design in Fig. 3.2 across 11 wafers, consistent with the fluxonium Hamiltonian in Eq. (1.7). This provides the first evidence for a remarkably conventional sinusoidal CφR of the grAl nanojunction within the gralmonium qubit. We further test the robustness of this hypothesis by using slightly slanted CφR to model the spectroscopy in Section 5.2, confirming the SIS CφR of the nanojunction.

From the fit to the qubit spectrum, we extract a Josephson energy of $E_\mathrm{J}/\mathrm{h} = 23.4\,\mathrm{GHz}$, in agreement with the order of magnitude of our estimation for the nanojunction E_J in Section 3.1.1. The remaining deviation by a factor of ~ 3 is likely attributed to a combination of several effects, including but not limited to:

- The nanojunction cross-section, which is rounded (cf. Fig. 3.1a) rather than resembling an ideal $20\,\mathrm{nm} \times 20\,\mathrm{nm}$-square, reducing the critical current for a given current density.
- An increased surface-to-volume ratio compared to a planar grAl film, potentially leading to increased local resistivity and surface oxide thickness at the nanojunction position.
- The specific grain configuration within the nanojunction.
- The (yet unknown) origin of fluctuations in critical current between cooldowns of the same device (cf. Section 5.3).
- The onset of the suppression of superconductivity due to dimensions only two to four times larger than the grAl coherence length [141, 193, 194].

The fit also yields a qubit inductance of $L_\mathrm{q} = 285\,\mathrm{nH}$ and a total qubit capacitance of $C_\mathrm{q} = C_\parallel + C_\mathrm{J} = 1.26\,\mathrm{fF}$. The extracted value of L_q, which is significantly lower than expected based on the grAl sheet inductance and the number of squares in the meandered geometry, confirms that the meandered geometry partially charges up, behaving capacitive rather than purely inductive, as indicated in Fig. 3.2b. Furthermore, the extracted qubit

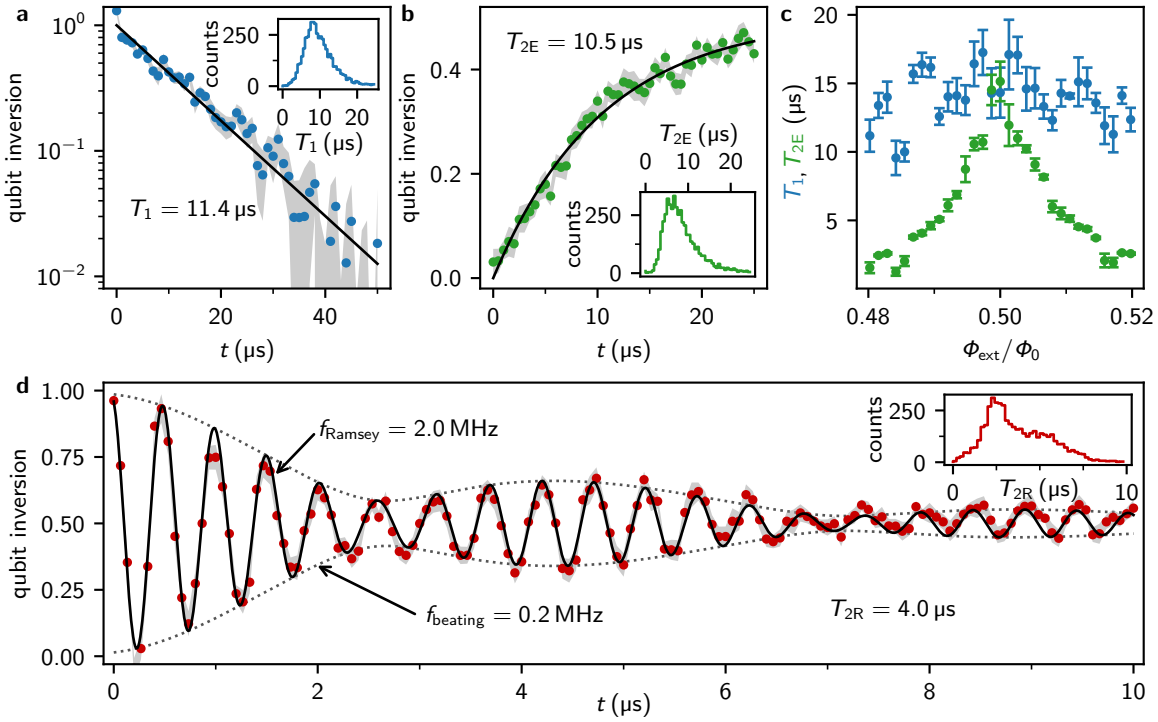

Figure 3.4: Energy relaxation and coherence of the gralmonium at half-flux bias. **a** Free decay energy relaxation and **b** Hahn echo experiments, both fitted with exponential decays (black lines), yielding relaxation and echo coherence times of $T_1 = 11.4\,\mu s$ and $T_{2E} = 10.5\,\mu s$, respectively. **c** Extracted T_1 (blue) and T_{2E} (green) decay times as a function of external flux ϕ_{ext}, in the vicinity of the half-flux sweet spot. Data points represent the mean values, with error bars indicating the standard error of the mean over five consecutive flux sweeps. **d** Ramsey fringes measured at a detuning of $f_{Ramsey} = 2\,MHz$ reveal a beating pattern, indicative of qubit frequency fluctuations between two distinct values. A two-frequency fit (black lines) yields a beating frequency of $f_{beating} = 0.2\,MHz$ and a Ramsey coherence time of $T_{2R} = 4.0\,\mu s$. A detailed analysis of these frequency fluctuations is provided in Section 5.3. **Insets:** Histograms of extracted relaxation and coherence times over 5000 repetitions:T_1 energy relaxation (panel a), T_{2E} Echo coherence (panel b) and T_{2R} Ramsey coherence (panel d), where each repetition contains 100 single-shot qubit measurements per data point. In panels a, b, and d, markers and gray error bands indicate the mean and standard error of the mean over 20 repetitions. Adapted from Ref. [3].

capacitance C_q reveals a small intrinsic nanojunction capacitance $C_J \approx 0.46\,fF$, with C_q dominated by the geometric contribution of the interdigitated shunt capacitor, consistent with design expectations. The resulting ratio E_J/E_C leads to a delocalization of the $|g\rangle$ and $|e\rangle$ wavefunctions across multiple potential wells, even at zero-flux bias (cf. Section 5.4.2). Surprisingly, the linewidth of the $|g\rangle \rightarrow |e\rangle$ transition does not narrow near the half-flux sweet spot (see top-right inset in Fig. 3.3b), suggesting the presence of a decoherence mechanism beyond the expected flux noise. Indeed, TT spectroscopy shows a toggling of the qubit frequency on a timescale of minutes between consecutive traces, consistent with fluctuations in the critical current. This observation foreshadows the presence of critical current noise, which is discussed in further detail in Fig. 3.4 and Section 5.3.

We complete the initial characterization of the gralmonium by evaluating its energy relaxation and coherence at half-flux bias in Fig. 3.4. While such metrics are established

figures of merit for quantum information processing (QIP), they are equally critical for assessing the suitability of gralmonium for the detection of individual spins. Specifically, these quantities directly influence the achievable resolution in measurements of the qubit transition frequency, which encodes the spin state (cf. Section 2.3). The qubit energy relaxation time T_1 enters directly into the Ramsey and Hahn Echo coherence times $1/T_2 = 1/(2T_1) + 1/T_\varphi$, thereby determining the spectral resolution of Ramsey-based frequency measurements. In addition, T_1 affects the readout fidelity, as it governs the decay of the qubit population during the measurement window, consequently impacting the accuracy of frequency determination over a given time interval, such as a fraction of the spin T_1. Beyond the contribution from energy relaxation, the ultimate frequency resolution is set by the pure dephasing time T_φ, which quantifies the fluctuations in the qubit transition frequency. In the rotating frame, this corresponds to a dephasing between different single-shot qubit measurements.

From free decay energy relaxation, we extract an average relaxation time of $\bar{T}_1 = 10.5\,\mu s$ using a single-exponential fit to the decay. Although this value is below the performance of state-of-the-art superconducting qubits optimized for QIP [101], it is comparable to that of devices based on SIS junctions that are not yet fully optimized for such applications [34, 117, 124, 176, 177], especially when considering the relatively high gralmonium half-flux frequency and assuming a constant quality factor Q such that the energy relaxation scales as $T_1 = Q/\omega_q$. Notably, energy relaxation times extracted from quantum jump measurements (cf. Section 5.4.3) are in close agreement with those obtained from free decay. This consistency indicates QND readout and suggests photon-number-independent energy relaxation, as previously observed in other grAl-based fluxonium devices [103].

To investigate qubit dephasing, we begin by isolating fast frequency noise through spin Hahn echo measurements, where a single refocusing π-pulse suppresses contributions from low-frequency fluctuations in the qubit frequency. We measure an average Hahn echo coherence time of $\bar{T}_{2E} = 9.2\,\mu s$ (cf. Fig. 3.4b). The maximum T_{2E} is reached at the $\Phi_{ext}/\Phi_0 = 0.5$ sweet spot, where the qubit spectrum is first-order insensitive to flux noise (cf. Fig. 3.4c). Note that the coherence times T_{2E} presented in Fig. 3.4c correspond to $1/e$-decay times extracted from single-exponential fits, which provide a unified figure of merit encompassing both exponential and Gaussian dephasing components. A comprehensive analysis of the decoherence budget, including the impact of flux noise, is provided in Section 5.4.1, revealing photon shot noise in the resonator as a likely limitation of the qubit coherence.

In Fig. 3.4d, we present a representative Ramsey interference measurement, which serves as a primary figure of merit for the single-spin detection in our proposed longitudinal coupling scheme (cf. Section 2.3). Due to additional sensitivity to low frequency noise in the Ramsey sequence, we observe a reduced average coherence time of $\bar{T}_{2R} = 3.9\,\mu s$ compared to Echo experiments. Interestingly, the Ramsey fringes exhibit a beating pattern with a beating frequency of $f_{beating} = 0.2\,MHz$, which we account for by performing a two-frequency fit. This beating corresponds to a 0.2 MHz toggling of the qubit frequency, attributed to critical current fluctuations in the nanojunction. These conspicuous fluctuations persist

and increase in amplitude on longer timescales (cf. Section 5.3), reminiscent of the typically observed $1/f$-like noise [30–34, 177, 195, 196].

Although such fluctuations are unconventional in the context of superconducting qubits, their presence in the gralmonium is not entirely unexpected, given that the low-energy fluxonium transitions are governed by quantum tunneling through the Josephson barrier(cf. Fig. 5.11). Approximating the $|g\rangle \rightarrow |e\rangle$ transition using the phase-slip rate in Eq. (2.4) highlights the exponential sensitivity of the transition frequency to the ratio E_J/E_C. Accordingly, these fluctuations - despite being detrimental to qubit performance - provide direct evidence of the susceptibility of the gralmonium transition frequency to microscopic changes within the $(20\,\mathrm{nm})^3$ volume of the grAl nanojunction and its close vicinity. This observation is consistent with the design considerations discussed in Section 3.1.1 and Section 2.3, where maximizing the susceptibility to individual spins positioned atop the nanojunction was a key objective. Additionally, the interdigitated shunt capacitance, which bounds the charging energy, renders the spectrum particularly sensitive to changes in E_J, as further detailed in Section 5.3. This is advantageous for single-spin detection, since the spin state is encoded via a suppression the Josephson energy alone. Nevertheless, we observe that the fluctuations of E_J and E_C are not entirely independent but appear correlated (cf. Fig. 5.6), indicating that the quasiparticle capacitance [197] of the nanojunction, which we estimate in the range of 0.05 fF, plays a non-negligible role in the gralmonium.

The source of the intrinsic fluctuations of the nanojunction critical current cannot be conclusively determined without further experiments and includes several possible origins. A first class of mechanisms involves intrinsic structural changes within the nanojunction volume. These may include tunneling two-level systems such as crystalline defects, vacancies, interstitial impurities, or local rearrangements within the metallic grains or the surrounding oxide [33, 35, 91]. In addition, external perturbations, such as adsorbed molecules or surface contaminants, can alter the local superconducting properties of the nanojunction [35, 91]. Another prominent candidate is charge noise arising from dynamically trapped charges, which couple to the superconducting phase via the Aharonov-Casher effect [198–200]. In this scenario, randomly trapped charges in the grain boundaries or substrate induce phase shifts in the tunneling paths of Cooper pairs. Reconfiguration of these charges leads to fluctuating interference conditions and, consequently, modulates the effective Josephson coupling. In light of the proposed longitudinal single-spin coupling scheme, another potential origin involves paramagnetic defects near or within the nanojunction. Unpaired spins located at material interfaces, in the substrate, or embedded within the oxide may undergo spin flips or reorientations, thereby modifying the local gap suppression and, in turn, the Josephson energy. This mechanism raises a particularly intriguing possibility: that the nanojunction may already be coupled to individually addressable spins. We will address this hypothesis in Section 3.3.1 by applying high magnetic fields to polarize these potential spins. Further experiments to disentangle these candidate mechanisms are discussed in Part III.

3.2 Resilience of the Gralmonium to High Magnetic Fields

In the preceding chapter, we demonstrated coherent operation of the gralmonium qubit, a milestone for the implementation of single-spin detection within our longitudinal coupling architecture. Beyond the nanoscopic footprint of the nanojunction, spin qubit operation requires high magnetic fields to tune the spin transition frequencies in the GHz-regime. In this chapter, we investigate the magnetic field resilience of the gralmonium and demonstrate coherent qubit performance in magnetic fields up to 1 T in-plane. We also describe the required modifications to the qubit design to maintain coherence under such conditions.

3.2.1 Gradiometric Fluxonium Design

Superconducting qubits have traditionally been incompatible with high magnetic fields, which significantly alter both the qubit spectrum and its coherence properties. This limitation applies not only to conventional SIS JJs [175–177], but also to more unconventional junction platforms, including those based on semiconducting nanowires [125, 181–183] or graphene [184]. The gralmonium may appear inherently resilient to magnetic fields owing to two key features: the high critical field of granular aluminum ($B_c \approx 6\,\mathrm{T}$ [139]) and the nanoscopic footprint of the nanojunction, which exposes a minute cross-section to Fraunhofer interference. However, despite these intrinsic advantages, several mechanisms remain that can degrade qubit performance in high magnetic fields. These include:

- Magnetic-field-induced variations in the Josephson energy, potentially driven by the same mechanism responsible for temporal fluctuations of the nanojunction E_J (similar to Refs. [181, 182])
- Vortex motion in the superconducting leads [175, 184]
- Elevated levels of flux noise [177]

Microwave loss measurements of grAl resonators in the single photon regime have already demonstrated magnetic field resilience [4, 139] (cf. Section 4.1), rendering increased quasiparticle-induced losses less likely in our case. However, the use of a flux-tunable qubit renders the gralmonium circuit in Fig. 3.2 vulnerable to global flux noise, e.g. stemming from fluctuations of the perpendicular magnetic field component $B_\perp$ when operating in high magnetic fields $B_\parallel \sim 1\,\mathrm{T}$. Such variations can for instance originate from current noise in the vector magnet or from thermally activated magnetic vortices in the magnet coils.

To reduce the sensitivity to these perpendicular magnetic field fluctuations, we implement a gradiometric qubit design [6, 125, 201, 202], shown in Fig. 3.5. The device comprises two flux loops (highlighted in violet and ocher in Fig. 3.5a), threaded by external fluxes $\Phi_{\mathrm{ext},1}$ and $\Phi_{\mathrm{ext},2}$, respectively. Similar to the gralmonium design presented in Section 3.1, the entire circuit is patterned from a single 20 nm-thick grAl film with a sheet inductance of $L_\square = 0.75\,\mathrm{nH}/\square$ and resistivity $\rho = 2000\,\mu\Omega\,\mathrm{cm}$ (cf. Appendix A.3). The qubit is

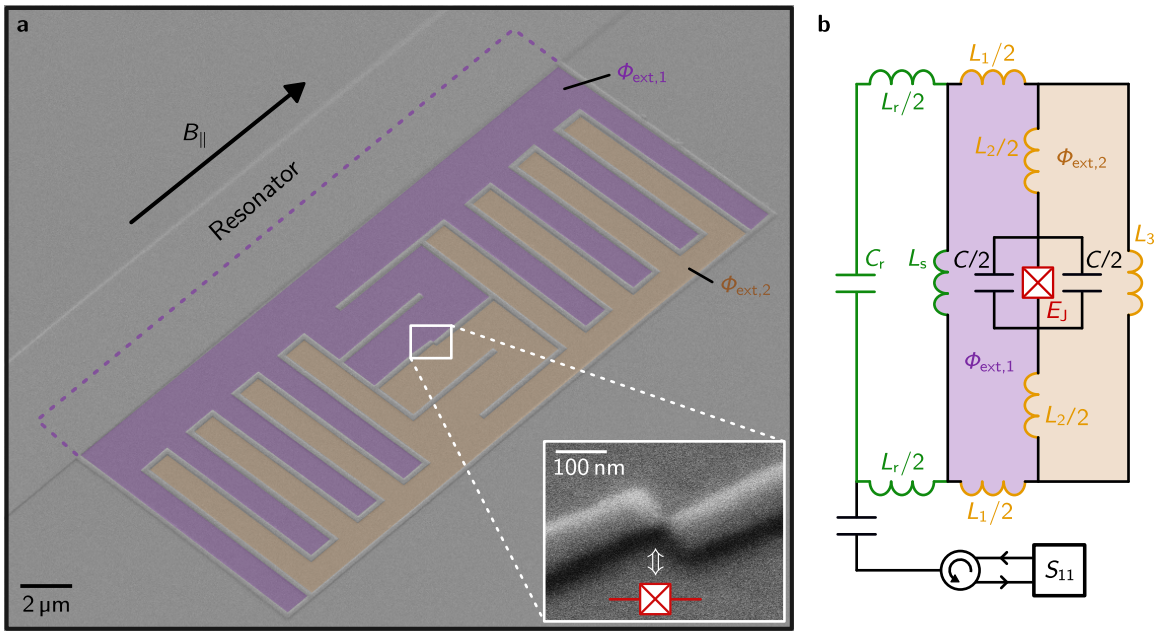

Figure 3.5: Gradiometric gralmonium qubit. **a** False-colored SEM image of the gradiometric qubit circuit. The nanojunction, shunted by an interdigitated capacitor, is enclosed by two flux loops threaded by external fluxes $\Phi_{ext,1}$ and $\Phi_{ext,2}$, respectively. This implements a gradiometric qubit design [6] with effective flux Φ_{ext} (cf. Eq. (3.2)), where both loops share a meandered superinductor. The colored regions (violet & ocher) illustrate a deliberate 10% mismatch in loop areas, enabling controlled flux biasing. The readout resonator is galvanically coupled to one loop and participates in $\Phi_{ext,1}$, as indicated by the violet dashed line, due to the spatial current distribution within the resonator. The device is patterned from a single 20 nm-thick grAl film (similar to Fig. 3.2). An in-plane magnetic field $B_\parallel$ is applied within the substrate plane. **Inset:** Zoom-in on the grAl nanojunction. **b** Lumped-element circuit representation of the gradiometric gralmonium qubit in panel a: The two flux loops contain inductances $L_1 + L_s$ and L_3, respectively, and share a common segment with inductance L_2 that embeds the JJ (with Josephson energy E_J) shunted by a capacitance C. The qubit is inductively coupled via L_s to the readout resonator (inductance L_r, capacitance C_r) for which we measure the single-port reflection coefficient S_{11}.

galvanically coupled to a 1 mm long readout resonator, which shares a 21 µm segment with the qubit circuit.

The equivalent lumped-element circuit schematic in Fig. 3.5b can be mapped to the standard fluxonium Hamiltonian in Eq. (1.7) [6, 202]. This allows to describe the qubit with an effective qubit inductance

$$L_q = \frac{L_{1,s}L_2 + L_2L_3 + L_3L_{1,s}}{L_{1,s} + L_3}, \quad \text{with} \quad L_{1,s} = L_1 + L_s, \tag{3.1}$$

and an effective external flux Φ_{ext}, given by

$$\Phi_{ext} = \Phi_\Delta - \alpha\Phi_\Sigma, \tag{3.2}$$

where, $\Phi_{\Sigma/\Delta} = \frac{\Phi_{ext,1}}{2} \pm \frac{\Phi_{ext,2}}{2}$ denote the mean and difference of fluxes in the two loops, respectively. The asymmetry parameter α quantifies the inductance imbalance between the two flux paths, given by $\alpha = \frac{L_{1,s}-L_3}{L_{1,s}+L_3}$.

While the gradiometric design is intended to reduce the qubit's susceptibility to global magnetic field fluctuations, it is essential that the flux modulation remains below the threshold field $B_{\perp,\text{thres}}$ of the resonator, above which the device exhibits enhanced microwave losses and a hysteretic frequency response ($B_{\perp,\text{thres}} \approx 1\,\text{mT}$ for a 10 µm-wide resonator), most likely due to the introduction of vortices [139]. An additional source of uncertainty in the effective flux modulation arises from the distributed nature of the qubit design. In particular, segments of the meandered inductor may charge up capacitively (similar to the design in Fig. 3.2), thereby reducing the effective inductance and complicating precise predictions of the inductive asymmetry. This asymmetry, however, directly enters into Eq. (3.2) through Φ_Σ.

Consequently, we design the flux loops with a conservative 10% mismatch in the enclosed areas (cf. colored regions in Fig. 3.5). Assuming approximately uniform current flow through the 4 µm-wide shared inductance segment (dashed line in Fig. 3.5a), we estimate the loop areas as $A_1 = 145\,\mu\text{m}^2$ and $A_2 = 82\,\mu\text{m}^2$. This corresponds to the reduction of the magnetic flux susceptibility by a factor of $\Phi_{\text{ext},1}/\Phi_\Delta = 4.6$ in our gradiometric design. Surprisingly, we observe a similar suppression in our experiments (cf. Section 6.1), indicating negligible inductive asymmetry $\alpha \approx 0$.

3.2.2 Qubit Spectroscopy in Magnetic Field

Figure 3.6a presents the spectrum of the gradiometric gralmonium qubit, measured via TT spectroscopy up to 13 GHz. We obtain qubit frequencies of $f_\text{q}(\Phi_\text{ext} = \Phi_0/2) = 2.38\,\text{GHz}$ and $f_\text{q}(\Phi_\text{ext} = 0) = 8.82\,\text{GHz}$ at the sweet spot working points in zero magnetic field, $B_\parallel = 0\,\text{T}$, illustrated in TT spectroscopy measurements in Fig. 3.6b, d. A joint fit of the $|\text{g}\rangle \rightarrow |\text{e}\rangle$ and $|\text{g}\rangle \rightarrow |\text{f}\rangle$ transitions using a numerical diagonalization of the fluxonium Hamiltonian (Eq. (1.7)) yields typical fluxonium parameters: $E_\text{J} = 32.2\,\text{GHz}$, $E_\text{c} = 14.1\,\text{GHz}$ and $E_\text{L} = 0.454\,\text{GHz}$. These values are consistent with those obtained for the non-gradiometric gralmonium implementation described in Section 3.1. To assess the stability of the qubit spectrum in high magnetic field, we track the evolution of the sweet spot frequencies to $B_\parallel = 1.2\,\text{T}$ (the limit of our vector magnet) in Fig. 3.6c, e. We observe a parabolic decrease of the zero-flux frequency by $\delta f_\text{q}(\Phi_\text{ext} = 0) = -236\,\text{MHz}$ and an increase of the half-flux frequency by $\delta f_\text{q}(\Phi_\text{ext} = \Phi_0/2) = +32\,\text{MHz}$ in 1.2 T, respectively. Remarkably, these changes correspond to relative variations of only 2.7% and 1.3%, respectively, confirming that the gradiometric gralmonium qubit remains spectrally stable and illustrating its compatibility with high magnetic fields. Notably, the TT spectroscopy data acquired under applied magnetic field appears increasingly blurred compared to zero field (see insets in Fig. 3.6), which we attribute to elevated levels of low-frequency flux noise. This broadening is likely caused by mechanical vibrations of the sample holder within the vector magnet (cf. Appendix B.1).

From TT spectroscopy in magnetic field, we extract the qubit spectrum in the vicinity of the sweet spots for each value of $B_\parallel$. To assess the effect of magnetic field on the fluxonium parameters, we fit this subset of the spectrum at each $B_\parallel$ using numerical diagonalization of the fluxonium Hamiltonian (Eq. (1.7)). Since this analysis is restricted to

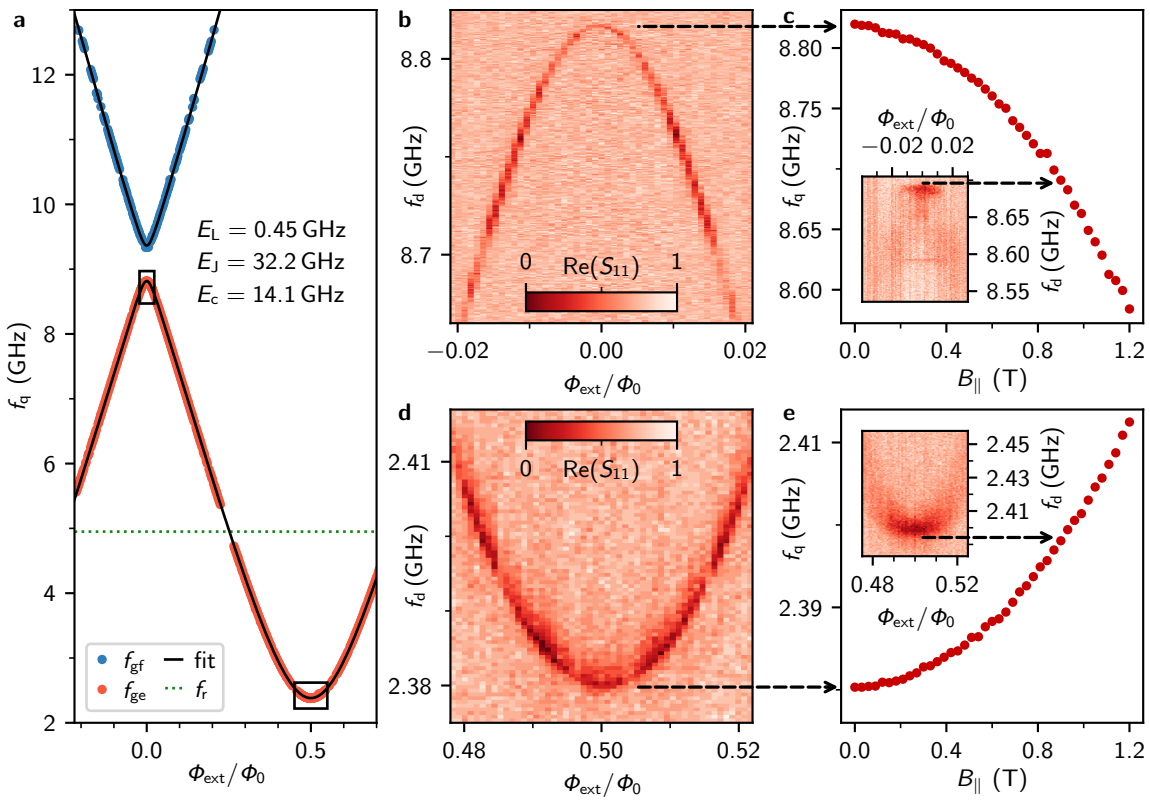

Figure 3.6: Gradiometric gralmonium spectroscopy in magnetic fields. **a** Qubit spectrum obtained from TT spectroscopy. Markers indicate the fluxonium transitions $|g\rangle \rightarrow |e\rangle$ (red) and $|g\rangle \rightarrow |f\rangle$ (blue). From a fit (black line) to the fluxonium Hamiltonian (Eq. (1.7)), yields the qubit parameters: $E_J/h = 32.2$ GHz (i.e. critical current $I_c = 64.9$ nA), $E_C/h = 14.1$ GHz ($C = 1.37$ fF) and $E_L/h = 0.454$ GHz ($L_q = 360$ nH). The absence of extracted qubit frequencies around the readout resonator frequency $f_r = 4.95$ GHz (dotted green line) results from avoided level crossings. **b, d** TT spectroscopy at the half-flux $\Phi_{ext} = \Phi_0/2$ (**b**) and zero-flux $\Phi_{ext} = 0$ (**d**) sweet spots in zero magnetic field ($B_\parallel = 0$ T) (black boxes in a). Spectra were acquired by applying a second drive tone f_d while monitoring the resonator response, encoded in reflection coefficient S_{11}. **c, e** Magnetic field dependence of the qubit frequency f_q at $\Phi_{ext} = 0.5\,\Phi_0$ (**c**) and $\Phi_{ext} = 0$ (**e**) as, extracted from TT spectroscopy measurements analogous to panels b and d, respectively. Notably, the qubit frequency at $\Phi_{ext} = 0.5\,\Phi_0$ exhibits only a 32 MHz increase in $B_\parallel = 1.2$ T, demonstrating the resilience of the gradiometric gralmonium to parallel magnetic fields $B_\parallel$. **Insets in c, e:** TT spectroscopy in $B_\parallel = 0.9$ T. Adapted from Ref. [1].

a limited frequency range near the sweet spots, we fix the qubit capacitance at $C = 1.37$ fF, obtained from the fit to the full spectrum in zero field. This approach is justified by the geometric origin of the capacitance, which is not expected to vary with $B_\parallel$. As shown in Fig. 3.7a, the extracted parameters reveal a suppression of the Josephson energy E_J and an increase in the qubit inductance L_q, consistent with a magnetic-field-induced suppression of the superconducting gap $\Delta(B_\parallel)$: According to the Ambegaokar-Baratoff relation (cf. Section 1.3.3 and Ref. [130]), the Josephson energy scales as $E_J \propto \Delta(B_\parallel)$, while the kinetic inductance of the superinductor follows $L_{kin} \propto 1/\Delta(B_\parallel)$ within the framework of the Mattis-Bardeen theory (cf. Eq. (1.10)).

Assuming that the observed shifts arise solely from changes in the superconducting gap, we map the relative shifts in E_J, L_q, and the resonator inductance L_r to corresponding relative

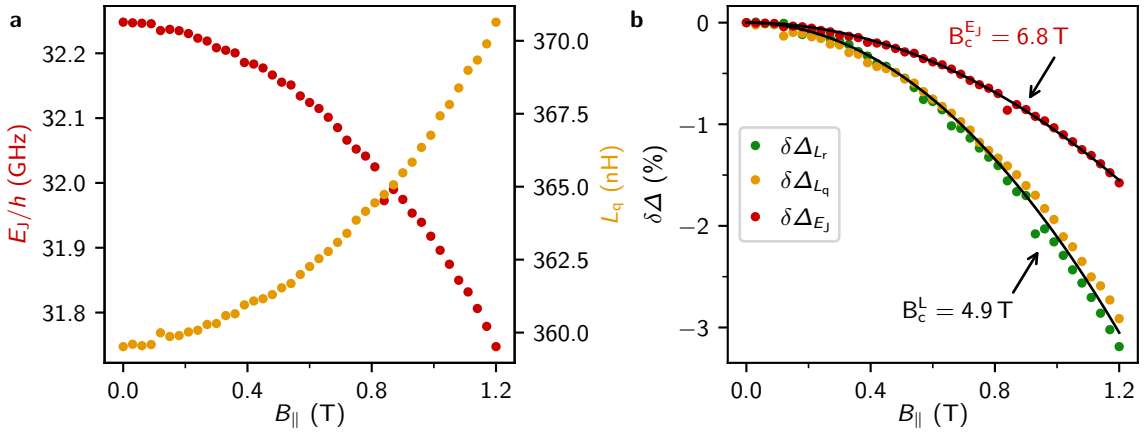

Figure 3.7: Geometry-dependent magnetic field resilience of gralmonium circuit elements. **a** Extracted values of the Josephson energy E_J (red) and qubit inductance L_q (ocher) as functions of the in-plane magnetic field $B_\parallel$. E_J and L_q are obtained from fits to the qubit spectrum (cf. Fig. 3.6a) by assuming a constant qubit capacitance C_q, fixed to the fit value obtained in $B_\parallel = 0$ T (cf. Fig. 3.6a). **b** Relative suppression of the grAl superconducting gap $\delta\Delta = \Delta(B_\parallel)/\Delta_0$ in magnetic field $B_\parallel$. The suppression is extracted from changes in the Josephson energy E_J of the nanojunction (red), the inductive energy E_L of the superinductor (ocher), and the readout resonator inductance L_r (green). Fits to the field dependence of the superconducting gap in Eq. (3.3) (black lines) yield critical fields of $B_c^{E_J} = 6.8$ T and $B_c^{L} = 4.9$ T for the Josephson and inductive elements, respectively, indicating a 40% higher critical field for the nanojunction. Notably, the agreement between the fit and the $\delta\Delta$ values extracted from qubit spectroscopy confirms that the magnetic field primarily affects the qubit spectrum via suppression of the superconducting gap. Adapted from Ref. [1].

gap suppressions in the nanojunction ($\delta\Delta_{E_J}$), the superinductor ($\delta\Delta_{L_q}$) and the resonator ($\delta\Delta_{L_r}$), respectively. Interestingly, as shown in Fig. 3.7b, the nanojunction exhibits an even higher resilience to magnetic field than both the grAl resonator and superinductor. This indicates that Fraunhofer interference is negligible in the nanojunction, consistent with its nanoscopic dimensions. Moreover, the enhanced critical field observed for the nanojunction suggests a connection to its reduced physical scale compared to the other circuit elements, reminiscent of the dependence of the critical temperature on film thickness found in Ref. [203] To assess this quantitatively, we fit the extracted gap suppression to orbital pair-breaking model [204]

$$\Delta(B_\parallel)/\Delta_0 = \sqrt{1 - (B_\parallel/B_c)^2}\,, \tag{3.3}$$

where Δ_0 is the superconducting gap in zero field. From this fit, we extract an orbital critical magnetic field of $B_{E_J}^c = 6.8$ T for the nanojunction and $B_L^c = 4.9$ T for the resonator and qubit inductance (cf. Fig. 3.7c). Moreover, these extracted critical fields allow us to estimate the coherence length of our grAl elements within the framework of the Ginzburg-Landau theory to $B_c = \Phi_0/(2\pi\xi^2)$ [193]. This yields coherence lengths of $\xi_{E_J} = 7$ nm for the nanojunction and $\xi_L = 8.2$ nm for the resonator and superinductor. The reduced coherence length in the nanojunction may be attributed to its geometric confinement, which is only a factor of 2-3 larger than the extracted ξ. An alternative explanation is a locally increased normal-state resistivity ρ in the nanojunction, which would also reduce ξ and thereby increase the critical field B_c [193] As discussed in Section 3.1.3, such a local increase in

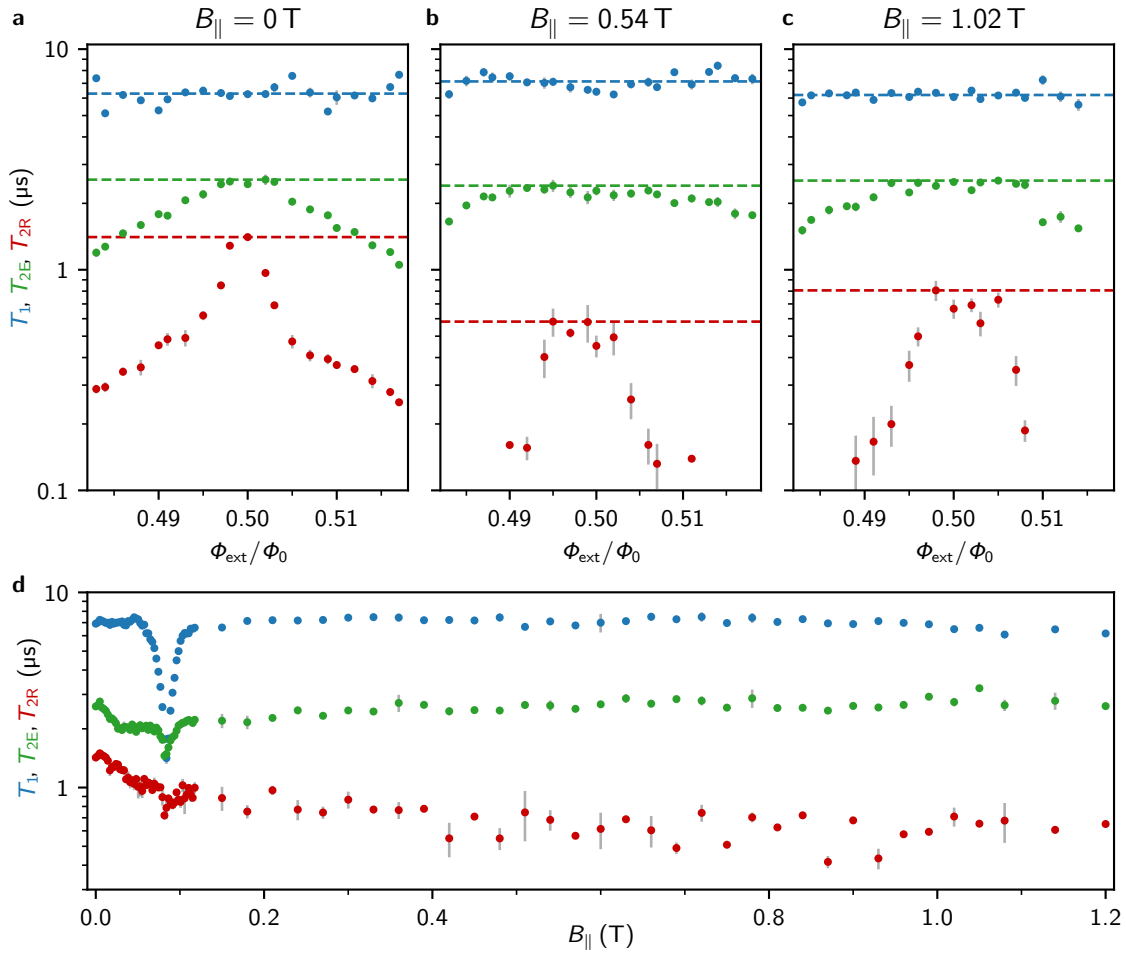

Figure 3.8: Qubit energy relaxation and coherence in magnetic field. **a-c** Energy relaxation time T_1 (blue), Hahn echo coherence time T_{2E} (green) and Ramsey coherence time T_{2R} (red) as a function of external flux in $B_\parallel = 0\,\mathrm{T}$ (**a**), $B_\parallel = 0.54\,\mathrm{T}$ (**b**) and $B_\parallel = 1.02\,\mathrm{T}$ **c**. Markers and error bars represent the mean and standard error of the mean of six consecutive measurements, respectively. Dashed lines correspond to the mean T_1 (blue), and the maximum values of T_{2E} (green) and T_{2R} (red). **d** Qubit energy relaxation (T_1, blue) and coherence times (T_{2E}, green; T_{2R}, red) of the gradiometric gralmonium as a function of in-plane magnetic field up to 1.2 T. The decay times correspond to the mean T_1 (blue) and the maximum T_{2E} (green) and T_{2R} (red) values taken from measurements vs. flux (top row, dashed lines). Markers and error bars display the mean and standard deviation of decay times from 3 flux sweeps. The drop in T_1 at $B_\parallel = 80\,\mathrm{mT}$ corresponds to electron spin resonance (ESR) with spin $s = 1/2$ matching the qubit frequency (see Fig. 3.9). Adapted from Ref. [1].

resistivity may result from enhanced oxide formation during nanojunction deposition, driven by its increased surface-to-volume ratio relative to planar grAl films.

3.2.3 Coherence and Stability in Magnetic Field

We continue the characterization of the gradiometric gralmonium qubit by evaluating its energy relaxation and coherence times under magnetic field. At the half-flux sweet spot, we measure energy relaxation times of $T_1 = 7\,\mu\mathrm{s}$. This value is slightly lower than

that observed for the non-gradiometric implementation in Section 3.1.3, likely due to dielectric losses in the interdigitated shunt capacitor. This interpretation is supported by the observed frequency dependence of the sweet-spot relaxation time in supplementary cooldowns (cf. Section 6.2), where the qubit frequency changes due to $\Delta E_J \sim$ GHz-changes in the nanojunction energy after thermal cycling (cf. Section 5.3) Similarly, the Ramsey and Hahn echo coherence times of $T_{2R} = 1.5\,\mu s$ and $T_{2E} = 2.6\,\mu s$, respectively, are also reduced compared to those obtained in Section 3.1.3. While increased critical current noise in the nanojunction remains a possible explanation, the dominant contribution is more likely due to photon shot noise in the readout resonator. This conclusion is reinforced by the fact that all measurements of the gradiometric device were conducted in the absence of dedicated infrared shielding around the sample holder (cf. Appendix B.1). A detailed analysis of the decoherence budget for the echo experiment is provided in Section 3.3.1.

Figure 3.8a shows the qubit decay times as a function of external flux near the half-flux sweet spot at zero magnetic field ($B_{\parallel} = 0$). The coherence times T_{2E} and T_{2R} in Fig. 3.8a-c correspond to the $1/e$-decay times extracted from single-exponential fits. As such, they capture both exponential and Gaussian dephasing contributions within a single figure of merit (see Section 3.3.1). While the energy relaxation time T_1 remains stable across the measured flux range, the maximum Ramsey and echo coherence times are consistently achieved at the half-flux sweet spot. To facilitate robust comparisons at high magnetic fields, we use the mean T_1 and the maximum values of T_{2R} and T_{2E} extracted from flux-dependent measurements as standardized coherence metrics (indicated by dashed lines in Fig. 3.8a). This choice ensures insensitivity to small magnetic flux drifts occurring within the time frame of individual sets of measurements vs. flux. Measurements of decay times vs. flux in magnetic field, shown in Fig. 3.8b,c, confirm the validity and stability of this approach.

Remarkably, the energy relaxation time T_1 and Hahn echo coherence time T_{2E} remain robust across the entire range of applied magnetic fields up to 1.2 T, the upper limit of our vector magnet (cf. Fig. 3.8d). In contrast, the Ramsey coherence time T_{2R} exhibits a moderate reduction, decreasing from a maximum of $T_{2R} = 1.5\,\mu s$ to $T_{2R} = 0.7\,\mu s$ at fields above 1 T. We attribute this degradation to enhanced low-frequency flux noise induced by the applied magnetic field. This interpretation is consistent with the broadening observed in TT spectroscopy data in magnetic field (cf. Fig. 3.6) and further reinforced by the evolution of the T_{2R} flux dependence with increasing field. While the overall flux dependence does not weaken, the sharp peak in T_{2R} observed at $\Phi_{ext} = 0.5\,\Phi_0$ in zero field (Fig. 3.8a) becomes flattened into a broad plateau with lower T_{2R} centered around $\Phi_{ext} \approx 0.5\,\Phi_0$ in applied magnetic field (Fig. 3.8b,c), before eventually decreasing further with flux detuning. These observations of elevated levels of low-frequency flux noise in magnetic field are likely caused by global flux fluctuations induced by mechanical vibrations of the sample holder within the vector magnet and vortex activation in the magnet windings [205]. Additional contributions may arise from local flux noise sources such as spin clusters [177].

Interestingly, while the maximum value of T_{2E} remains unaffected under magnetic field, the flux dependence of the echo coherence time weakens (cf. Fig. 3.8b, c). In contrast to the observations from T_{2R}, this T_{2E} stability rules out flux-noise-induced broadening as

the primary cause, since increased it would manifest as both a flattened flux dependence and a reduced coherence time. The persistence of long T_{2E} values despite suppressed flux dependence therefore points to an alternative, field-dependent decoherence mechanism affecting the echo signal. A detailed analysis of the flux-dependent echo decoherence budget in magnetic field is presented in Section 3.3.1.

3.3 Sensing Spins with a Gralmonium Qubit

In the preceding sections, we established the gralmonium as a coherent superconducting qubit with exponential sensitivity to changes within a nanoscopic volume, thereby providing single spin sensitivity. Furthermore, the gradiometric design exhibited remarkable resilience to high magnetic fields up to 1.2 T, crucial for spin qubit operation and in-situ tuning of spin properties. As a result, the gralmonium emerges as a promising platform for probing spin polarization phenomena in magnetic fields. In this section, we leverage this capability to first investigate spin signatures originating from the mesoscopic environment of the qubit. In the second part, we quantitatively assess the gralmonium's potential for single-spin detection.

3.3.1 Spin Environment of a Superconducting Qubit in High Magnetic Fields

We probe the magnetic susceptibility of the gralmonium's mesoscopic environment, which serves as a valuable extension of the device characterization before deliberately integrating individual spins into a gralmonium-spin hybrid architecture. As indicated by the Ramsey beating pattern in Section 3.1.3, the gralmonium may already be sensitive to signatures of individual spins in its environment. On the other hand, high magnetic fields offer a powerful tool to characterize and tune microscopic degrees of freedom (DOF) that are coupled to superconducting qubits. These various spurious environmental DOFs include quasiparticles [23, 24, 26, 27], charge offsets [23, 25], paramagnetic spins [28–34] and other two-level-system (TLS) environments [7, 35–37]. Despite their pervasiveness in superconducting circuits, their magnetic field susceptibilities are often unknown due to the incompatibility of conventional aluminum-based devices with high magnetic fields. Consequently, characterizing these DOFs in field is essential to inform strategies for mitigating their detrimental impact on qubit performance.

Signatures of Electron Spin Resonance

We begin our characterization by revisiting the gralmonium relaxation and coherence times in magnetic field in Fig. 3.9. A pronounced reduction in the energy relaxation time T_1 is observed at the magnetic field where electron spin resonance (ESR) of a spin-$s = 1/2$, $g = 2$ ensemble becomes resonant with the qubit transition frequency. By exploiting the $\sim$ GHz variations in the nanojunction Josephson energy E_J across cooldowns, we access a broad range of qubit sweet spot frequencies. This enables the observation of the T_1 dip at different values of magnetic field for the same device, i.e. same mesoscopic environment (cf. inset in Fig. 3.9). The extracted magnetic field values at which these relaxation minima occur exhibit a linear dependence on the qubit frequency, consistent with the ESR condition $B_{\mathrm{ESR}} = hf_{\mathrm{q}}/g\mu_{\mathrm{B}}$ for a $g = 2$, spin-$s = 1/2$ ensemble. This identifies the presence of a paramagnetic spin ensemble coupled to the gralmonium qubit. While this provides the first direct evidence of a superconducting qubit coupling to paramagnetic impurities,

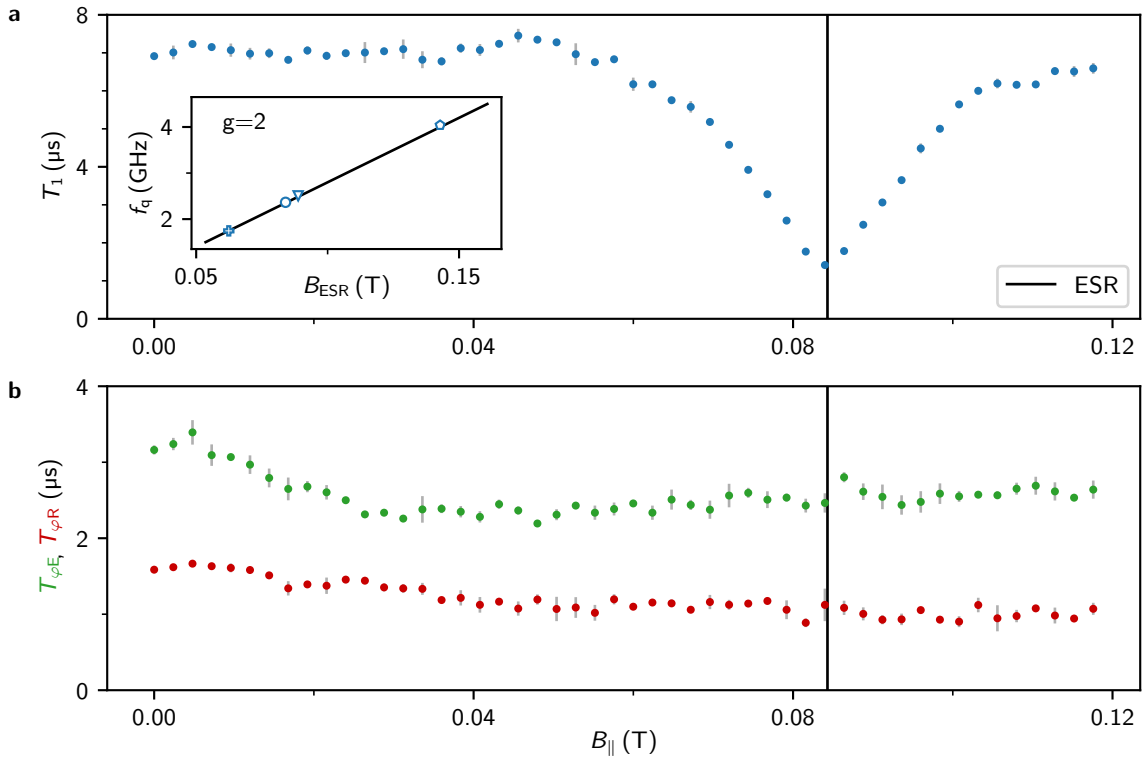

Figure 3.9: Signatures of electron spin resonance (ESR) in gralmonium qubit relaxation. **a** Qubit energy relaxation time T_1 as a function of parallel magnetic field $B_\parallel$ up to 120 mT. A pronounced drop in T_1 occurs when the qubit transition frequency f_q matches the ESR condition for a $g = 2$, spin-$s = 1/2$ ensemble (black line), indicating coupling to a bath of paramagnetic impurities of unknown origin. **Inset:** Qubit frequency f_q at $\Phi = 0.5\,\Phi_0$ across multiple cooldowns plotted against the magnetic field $B_{ESR} = hf_q/g\mu_B$ at which the relaxation time minimum is observed (cf. Section 6.2). The black line corresponds to the expectation $B_{ESR} = hf_q/g\mu_B$ for a spin $s = 1/2$, $g = 2$ system. Note that the qubit frequency shifts between cooldowns due to variations in the nanojunction energy $\Delta E_J \sim$ GHz (cf. Section 5.3), allowing to measure the same device with different ESR conditions. **b** Ramsey ($T_{\varphi R}$, red) and Hahn echo ($T_{\varphi E}$, green) dephasing times as functions of magnetic field remain unaffected by the ESR tuning in resonance with f_q. Adapted from Ref. [1].

similar ESR signatures have been observed in magnetic-field-dependent microwave loss measurements on superconducting resonators [134, 135, 139].

Importantly, this ESR feature does not affect the Ramsey or Hahn echo dephasing times, as expected in the regime where the coupling strength is much smaller than the qubit linewidth [206]. The observed $g = 2$, spin-$s = 1/2$ impurities are typically attributed to unpaired electrons localized in disordered aluminum oxide, adsorbed oxygen radicals, or dangling bonds at the sapphire-metal interface [28, 91, 207], highlighting their ubiquity in superconducting quantum circuits. Beyond confirming a long-hypothesized source of decoherence, the ESR-mediated reduction in T_1 illustrates the gralmonium's value as a built-in spectrometer for surface spins. This opens a pathway not only to diagnose but also to actively engineer the magnetic environment of superconducting qubits.

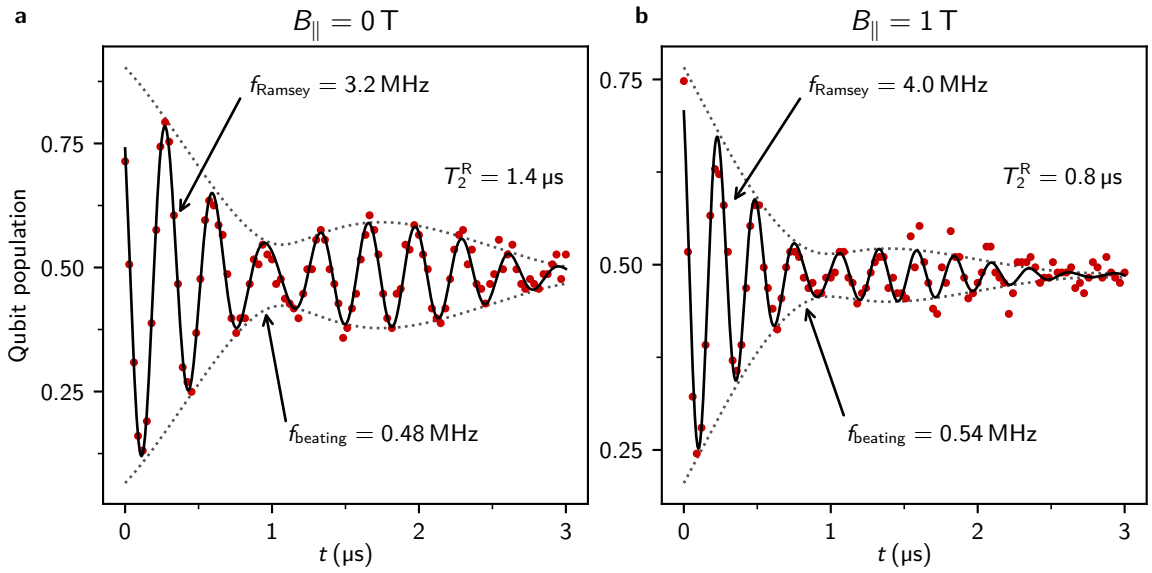

Figure 3.10: Discrete qubit frequency fluctuations in magnetic field. Ramsey fringes of the qubit measured in zero magnetic field $B_{\parallel} = 0$ (**a**) and in $B_{\parallel} = 1\,\mathrm{T}$ (**b**), at nominal detunings of $f_{\mathrm{Ramsey}} = 3.2\,\mathrm{MHz}$ and $f_{\mathrm{Ramsey}} = 4.0\,\mathrm{MHz}$, respectively. A two-frequency fit (black lines) reveals nearly identical beating frequencies of $f_{\mathrm{beating}} = 0.48\,\mathrm{MHz}$ and $f_{\mathrm{beating}} = 0.54\,\mathrm{MHz}$, respectively, as illustrated by the dotted envelope. This invariance indicates that the observed discrete qubit frequency fluctuations are independent of the applied magnetic field, suggesting a non-magnetic origin for the underlying mechanism. Adapted from Ref. [1].

Ramsey fringes beating pattern in magnetic field

As discussed in Section 3.1.3 and Section 5.3, the gralmonium exhibits discrete critical current fluctuations across a broad range of timescales. These fluctuations are potentially linked to structural defects, local charge noise, or paramagnetic impurities. Critical current fluctuations are also observed in conventional overlap Al/AlO_x/Al Josephson junctions and have been attributed to two-level systems (TLS) residing in the amorphous aluminum oxide barrier [35, 91, 196]. We use the beating pattern in the Ramsey fringes (cf. Fig. 3.10a) as a sensitive proxy for such fluctuations and investigate their susceptibility to magnetic field. If these fluctuations originate from a single spurious spin coupled to the nanojunction, as intended by the nanojunction's design goal of enabling single-spin sensitivity, a strong dependence on magnetic field would be expected.

However, Ramsey measurements performed at $B_{\parallel} = 1\,\mathrm{T}$ (cf. Fig. 3.10b) reveal a beating pattern nearly identical to that observed at zero field. This observation demonstrates that the discrete fluctuations in E_{J} persist even under strong magnetic fields, effectively excluding magnetically susceptible sources - such as a local spin environment - as their origin. To further elucidate the microscopic mechanism behind these fluctuations, additional experimental controls will be necessary. Promising approaches include applying an external electric field or mechanical strain to the substrate, both of which have previously been shown to tune TLS coupled to superconducting qubits [35, 144].

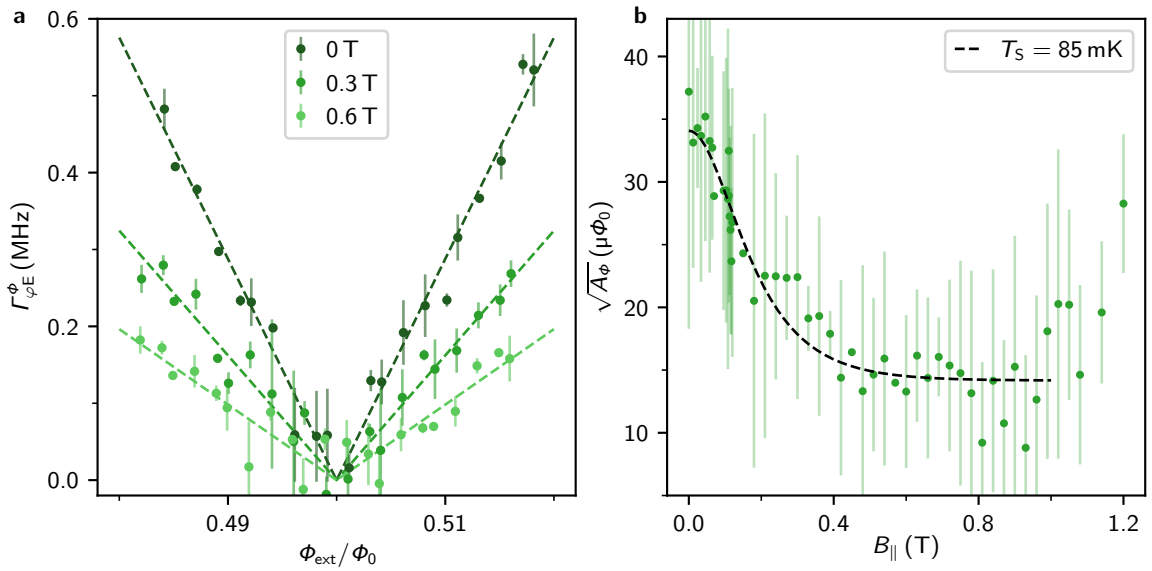

Figure 3.11: Freezing of fast flux noise in magnetic field. **a** Flux noise echo dephasing rate $\Gamma^{\Phi}_{\varphi E}$ as a function of external flux near $\Phi = 0.5$ at three values of magnetic field $B_\parallel$. The dephasing rate $\Gamma^{\Phi}_{\varphi E}$ corresponds to the Gaussian component of the Hahn echo decay and quantifies the contribution from fast flux noise (see main text). Dashed lines represent fits of the flux dependence to Eq. (3.5), from which the flux noise amplitude $\sqrt{A_\Phi}$ is extracted. Markers and error bars denote the mean and standard deviation from six consecutive measurements per flux point. **b** Flux noise amplitude $\sqrt{A_\Phi}$ as a function of applied magnetic field $B_\parallel$, extracted from fits as in panel a. A fit of the magnetic field dependence $\sqrt{A_\Phi(B_\parallel)}$ to Eq. (3.7) (dashed line) reveals a magnetic freezing of the flux noise consistent with a spin temperature of $T_S = 85$ mK. Markers and error bars display the mean and standard deviation of flux noise amplitudes obtained from three independent flux sweeps. Adapted from Ref. [1].

Freezing of Fast Flux Noise

While we have excluded a magnetically susceptible origin of the discrete critical current fluctuations, flux noise is a promising candidate for exhibiting magnetic field sensitivity. Ubiquitous in superconducting circuits, flux noise continues to be one of the dominant sources of decoherence and is therefore the subject of intense ongoing investigation. It is widely attributed to fluctuating magnetic moments, located on the surfaces or interfaces of superconducting materials, giving rise to a characteristic $1/\omega$ noise spectrum. Despite the prevailing consensus on the spin origin of flux noise, the precise microscopic mechanism remains under debate. In particular, whether spin-spin interactions are essential or whether the noise can be modeled by independent fluctuators is still an open question. Several theoretical models, both incorporating and omitting spin-spin interactions, have been proposed to explain experimental data [30–34, 177, 195]. Leveraging the magnetic field resilience of the gralmonium qubit allows us to explore the field dependence of flux noise in a regime previously inaccessible to conventional aluminum-based circuits. This capability offers a new perspective that could help clarify the microscopic origin of flux noise.

Figure 3.11a shows the flux dependence of the Hahn echo flux noise dephasing rate $\Gamma^{\Phi}_{\varphi E}$ in the vicinity of the half-flux sweet spot $\Phi_{ext} = \Phi_0/2$ for three in-plane magnetic fields

($B_\parallel = 0$, $B_\parallel = 0.3\,\mathrm{T}$, $B_\parallel = 0.6\,\mathrm{T}$). Off the sweet spot, we observe a Gaussian decay component in the Hahn echo signal, consistent with the $1/\omega$ spectral profile of the flux noise, where ω is the frequency of the spectral decomposition. This Gaussian contribution vanishes at the sweet spot, where the qubit is first-order insensitive to flux noise. To quantify the flux dependent Gaussian envelope $\exp^{-(\Gamma_{\varphi\mathrm{E}}^{\Phi} t)^2}$ in the decay, we extract $\Gamma_{\varphi\mathrm{E}}^{\Phi}$ on top of a purely exponential decay $e^{-(\Gamma_1/2+\Gamma_{\varphi\mathrm{E}}^{\mathrm{const}})t}$ evaluated at $\Phi_{\mathrm{ext}} = \Phi_0/2$, where the flux dependent contribution $\Gamma_{\varphi\mathrm{E}}^{\Phi}$ vanishes. This is justified by the observed flux independence of the energy relaxation near $\Phi_{\mathrm{ext}} \approx \Phi_0/2$ (cf. Fig. 3.8). The flux-independent dephasing rate $\Gamma_{\varphi\mathrm{E}}^{\mathrm{const}}$ is likely dominated by a combination of critical current noise and photon shot noise, both of which exhibit minimal flux dependence within the observed flux range. Assuming the entire $\Gamma_{\varphi\mathrm{E}}^{\mathrm{const}}$ contribution originates from photon shot noise, we estimate the average residual thermal photon number in the resonator $\bar{n}_{\mathrm{th}} = 0.27$ using the expression [208, 209]

$$\Gamma_{\bar{n}} = \frac{\bar{n}_{\mathrm{th}} \kappa \chi^2}{\kappa^2 + \chi^2} \tag{3.4}$$

where $\chi/(2\pi) = 0.5\,\mathrm{MHz}$ is the qubit-resonator dispersive shift $\kappa/(2\pi) = 1.2\,\mathrm{MHz}$ is the resonator linewidth. This corresponds to an effective resonator temperature of 150 mK, consistent with the qubit temperature extracted from IQ cloud histograms (cf. Section 6.4).

Interestingly, the flux dependence of the flux noise dephasing rate $\Gamma_{\varphi\mathrm{E}}^{\Phi}(\Phi_{\mathrm{ext}})$ weakens in magnetic field, as shown in Fig. 3.11a, reminiscent of earlier observations in flux qubits at lower fields up to 10 mT [177]. To quantify the flux noise, we extract the amplitude $\sqrt{A_\Phi}$ assuming a $1/\omega$ power spectral density for the flux noise, $S_\Phi(\omega) = 2\pi A_\Phi/\omega$, and fit the dephasing rate using the relation [32, 195] (cf. discussion in Section 6.3)

$$\Gamma_{\varphi\mathrm{E}}^{\Phi} = \sqrt{A_\Phi \ln 2} \left| \frac{\partial \omega}{\partial \Phi_{\mathrm{ext}}} \right| , \tag{3.5}$$

where $\sqrt{A_\Phi}$ is the flux noise amplitude, and $|\partial\omega/\partial\Phi_{\mathrm{ext}}|$ is the flux sensitivity of the qubit frequency. Figure 3.11b displays the evolution of $\sqrt{A_\Phi}$ in parallel magnetic fields up to $B_\parallel = 1.2\,\mathrm{T}$. We observe a reduction in flux noise amplitude by a factor of two, saturating around $B_\parallel = 400\,\mathrm{mT}$, which holds across different qubit frequencies in several cooldowns (cf. Section 6.3). We attribute the increase of $\sqrt{A_\Phi}$ for fields above $B_\parallel \gtrsim 1\,\mathrm{T}$ to the onset of an additional, competing mechanism, likely driven by vortex dynamics in the superconducting windings of the vector magnet.

To model the magnetic field dependence of flux noise, we consider a bath of magnetic two-level fluctuators. Each fluctuator is described as a source of asymmetric random telegraphic noise (RTN), i.e. exhibits a Lorentzian power spectrum. A single fluctuator contributes a Lorentzian power spectrum given by:

$$S(\omega) \propto \left(\frac{\Gamma_1}{\Gamma_\uparrow} + \frac{\Gamma_1}{\Gamma_\downarrow} \right)^{-1} \cdot \frac{\Gamma_1}{\Gamma_1^2 + \omega^2} , \tag{3.6}$$

where $\Gamma_1 = \Gamma_\uparrow + \Gamma_\downarrow$ denotes the total transition rate, and $\Gamma_\uparrow$, $\Gamma_\downarrow$ are the excitation and relaxation rates, respectively [210]. The corresponding power spectrum remains Lorentzian in the limit of identical fluctuators (i.e. identical Γ_1), while it maps on a $S(\omega) \propto 1/\omega$ dependence for fluctuators with log-uniform distribution of the switching rate (i.e. probability density $P(\Gamma_1) \propto 1/\Gamma_1$, cf. [195]), both of which have been observed for flux noise in superconducting qubits [177]. For any distribution, the amplitude of the power spectrum $A_\Phi \propto (\Gamma_1/\Gamma_\uparrow + \Gamma_1/\Gamma_\downarrow)^{-1}$ scales with magnetic field as (cf. Section 6.3)

$$A_\Phi \propto 1/\cosh^2\left(\frac{\mu_B B}{k_B T_S}\right). \tag{3.7}$$

Here, $2\mu_B B$ is the Zeeman energy difference of $g = 2, s = 1/2$ paramagnetic impurities and μ_B, k_B and T_S denote the Bohr magneton, Boltzmann constant and effective spin bath temperature, respectively. A fit of Eq. (3.7) aligns with the measured flux noise amplitude up to $B_\parallel = 1\,\mathrm{T}$ (see black line in Fig. 3.11b) and reveals a spin temperature of $T_S = 85\,\mathrm{mK}$.

This result indicates that the observed reduction in fast flux noise originates from the magnetic freezing, i.e. or polarization, of a bath of paramagnetic surface spins with $g = 2$ spin-$s = 1/2$: the suppression of excitation rates $\Gamma_\uparrow$ with increasing field reduces the number of spin flips, thereby lowering the flux noise amplitude. This freezing mirrors the spin polarization effects observed in the magnetization measurements in Section 2.2.1. Notably, our model is based on non-interacting spins, consistent with either intrinsically weak spin-spin interactions or a suppression of collective dynamics under applied magnetic field. Presumably, these spins constitute the same $g = 2$ spin-$s = 1/2$ environment responsible for the ESR signal in the qubit energy relaxation (cf. Fig. 3.9), a hypothesis that should be explored in future work.

Long-Lived Two-Level Systems

In Fig. 3.12, we leverage the field resilience of the gralmonium to probe the magnetic susceptibility of long-lived two-level systems (TLS) present in its environment. These TLSs were recently identified as a dominant relaxation channel in superconducting qubits [7, 206], with their signatures independently confirmed across various superconducting device architectures [7, 37, 211]. Due to their long intrinsic lifetimes, exceeding $1/\Gamma_{TLS} \geq 50\,\mathrm{ms}$, these TLSs induce non-Markovian relaxation dynamics in the qubit. Such memory effects of the environment are particularly detrimental to quantum error correction schemes in superconducting quantum processors, making a deeper understanding of their microscopic origin a pressing concern. Given their longevity, spins in the immediate vicinity of the qubit (e.g., surface spins or spin-based defects) present a natural candidate for these TLSs. We test this hypothesis by probing their magnetic field dependence. Importantly, the intrinsic decay time Γ_{TLS} of the TLS ensemble is much longer than their effective cross-relaxation rate with the qubit, estimated as $\sum_k \Gamma_{qt}^k \sim 40\,\mathrm{kHz}$ [7]. As a result, the qubit acts as the dominant relaxation channel for the TLSs. Since the TLSs are not directly accessible for independent manipulation or readout, we employ an indirect approach based on the cross-relaxation with the qubit, following the protocol introduced in Ref. [7]. This method

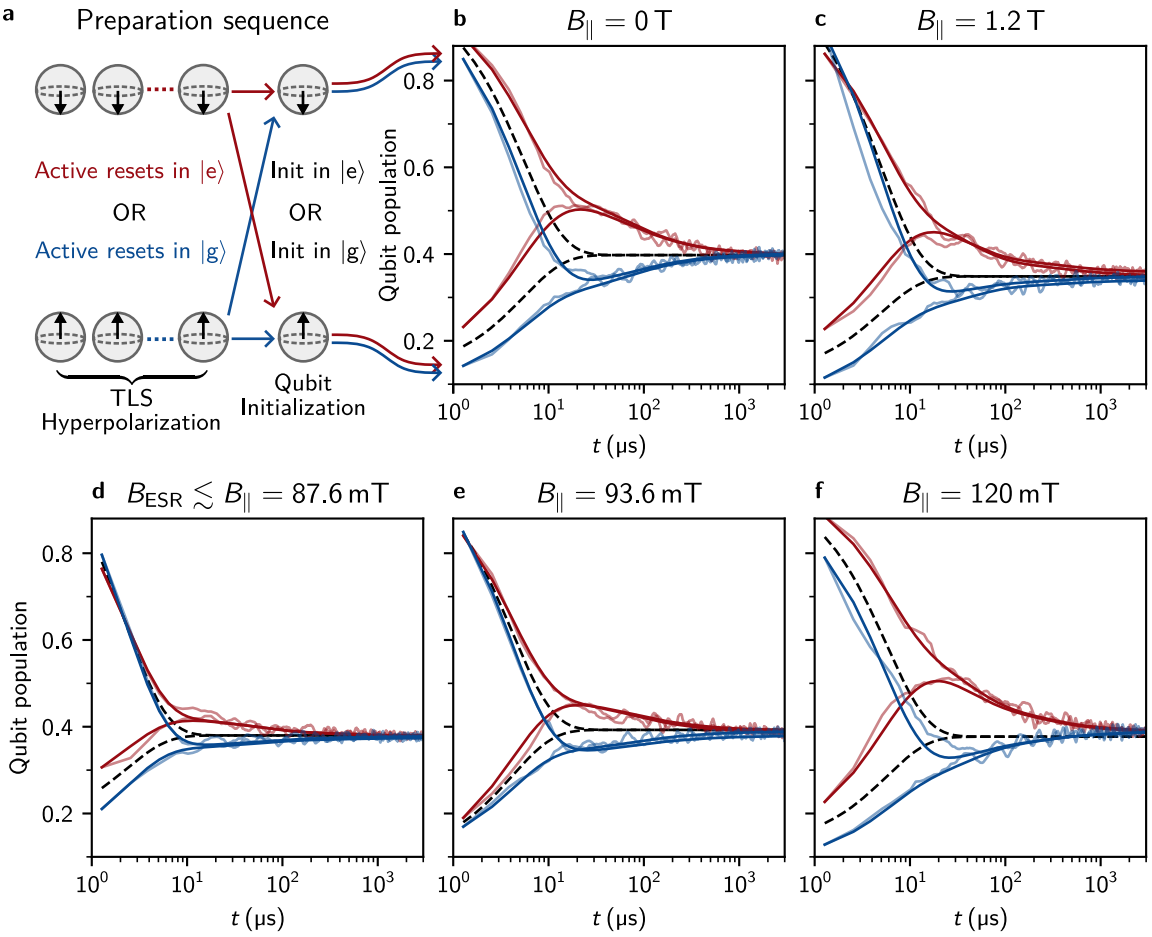

Figure 3.12: Hyperpolarization of long-lived two-level systems (TLS) in magnetic field. **a** Sketch of the preparation sequence used for TLS hyperpolarization. The qubit is actively reset to either the ground state $|g\rangle$ or excited state $|e\rangle$ over $N = 10^4$ repetitions to polarize the surrounding long-lived TLS ensemble via qubit-TLS cross-relaxation [7]. The final step consists of a single initialization into $|g\rangle$ or $|e\rangle$, independent of the prior state preparation, before beginning the relaxation measurement shown in panels b-f. **b-f** Qubit population relaxation following the hyperpolarization sequence, measured at different magnetic fields $B_{\parallel}$. Red and blue traces correspond to qubit preparation in $|g\rangle$ and $|e\rangle$, respectively. Semi-transparent lines show raw data; opaque lines represent fits to a TLS-based theoretical model (cf. [7, 206]). For reference, the black dashed lines indicate a single-exponential decay with the qubit energy relaxation rate Γ_1. **b** In zero field, deviations from the single-exponential decay - manifesting as overshoot (red) and undershoot (blue) - reproduce the hallmark signatures of TLS hyperpolarization previously observed in other superconducting qubits [7, 37, 211]. **c** These hyperpolarization features persist even in magnetic fields exceeding 1 T, indicating that the long-lived TLS ensemble is largely insensitive to magnetic field. **d-f** In the vicinity of the ESR resonance field $B_{\mathrm{ESR}} = 84\,\mathrm{mT}$ the hyperpolarization signatures are suppressed due to enhanced energy relaxation from the qubit into the paramagnetic spin ensemble (panel d). As the field increases beyond resonance, the TLS-induced signatures gradually re-emerge. In all panels, we use a 540 ns rectangular readout pulse and a 32 ns Gaussian shaped π-pulse. Adapted from Ref. [1].

enables both the preparation and observation of TLS hyperpolarization dynamics through qubit state evolution, which we outline in the following.

As illustrated in Fig. 3.12a, we implement a TLS hyperpolarization protocol by repeatedly applying active feedback-based state preparation of the qubit over $N = 10^4$ iterations, stabilizing it in either the ground state $|g\rangle$ or excited state $|e\rangle$. Through repeated cross-relaxation between the qubit and TLS ensemble, this sequence induces hyperpolarization of TLSs near the qubit frequency. As a result of the qubit-TLS cross-relaxation and the intrinsically long TLS lifetime, this sequence hyperpolarizes the set of TLS in the vicinity to the qubit frequency. Subsequent to this polarization sequence, the qubit is initialized in either $|g\rangle$ or $|e\rangle$, and its population is monitored using stroboscopic quantum jump measurements. Due to the TLS being a dominant relaxation channel for the qubit, its population relaxes to the TLS ensemble population on a T_1 timescale, after which it reflects the slow millisecond-scale decay of the TLS ensemble.

Figure 3.12b shows the resulting relaxation traces in zero magnetic field, revealing the characteristic signatures of a hyperpolarized TLS ensemble coupled to the gralmonium, consistent with previous observations in Ref. [7]. Regardless of the qubits initial state, the population relaxes towards a common equilibrium value on a microsecond timescale. When the TLSs are polarized in the excited state, the qubit exhibits an overshoot beyond its thermal equilibrium value; conversely, TLS polarization in the ground state results in an undershoot. These features are clearly distinguishable from the expected single-exponential relaxation, as indicated by the dashed black line in Fig. Fig. 3.12b. By modeling the qubit coupled to an equidistant ladder of 10^2 TLSs [7], we extract a gralmonium relaxation $\Gamma_1 = 1/5.4\,\mu s$, of which TLS cross-relaxation accounts for $\sum_k \Gamma_{qt}^k = 1/22\,\mu s$. While the model confirms the hyperpolarization of a set of long-lived TLSs at the origin of the observed signatures, it does not capture the exact TLS configuration, and variations in TLS positions or coupling strengths can introduce small discrepancies between datasets. As a result, we adopt the over- and undershoot of the qubit population relative to its thermal equilibrium value as a robust qualitative signature for characterizing TLS hyperpolarization. This provides a reliable metric to compare experiments at different magnetic fields.

As illustrated in Fig. 3.12c-f, the hyperpolarization signatures persist under applied magnetic field. Notably, the relaxation traces measured at 1.2 T (cf. Fig. 3.12c) are qualitatively similar to those obtained at zero field, indicating that the TLS bath is not susceptible to magnetic field. This observation rules out the initially intuitive hypothesis that the TLSs arise from electronic spins. Instead, non-magnetic microscopic origins such as subgap states or localized trapped quasiparticles [212] remain plausible candidates.

As shown in Fig. 3.12d, the TLS hyperpolarization signatures become less pronounced in the vicinity of the ESR resonance field $B_{\parallel} \approx B_{ESR} = 84\,mT$, where the qubit energy relaxation rate is enhanced by a factor of 7 (cf. Fig. 3.9). Consistent with the linewidth of the paramagnetic impurities probed with the qubit energy relaxation rate in Fig. 3.9, the characteristic overshoot and undershoot features of TLS hyperpolarization gradually re-emerge at higher magnetic fields (Fig. 3.12e,f) These observations suggest that we are still able to hyperpolarize the long-lived TLSs, while we cannot hyperpolarize the paramagnetic spin ensemble, as evidenced by the suppressed hyperpolarization features. This indicates

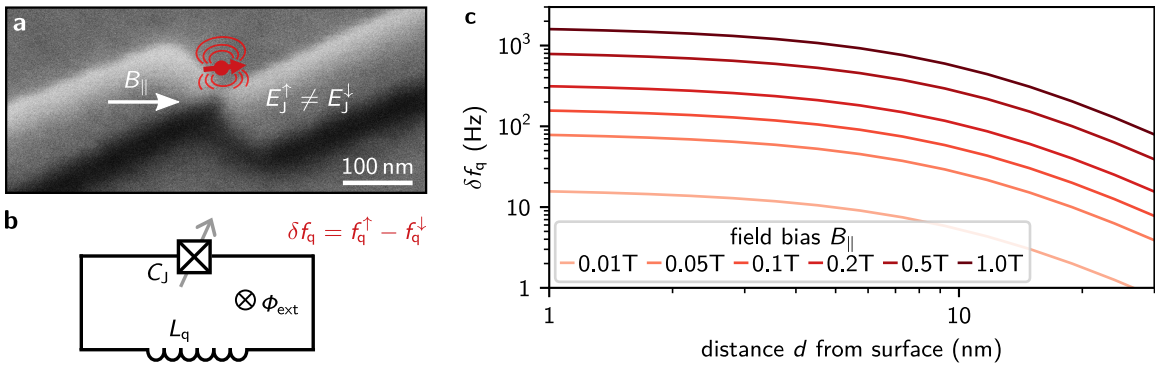

Figure 3.13: Longitudinal coupling between a superconducting qubit and a single spin. **a** Proposed implementation of a spin-state modulated Josephson Junction: SEM image of a grAl nanojunction with a spin sketched on top. When biased in magnetic field $B_\parallel$, the two spin orientations $|\uparrow\rangle$, $|\downarrow\rangle$ generate different magnetic fields leading to a spin-state dependent Josephson energy $E_J^\uparrow \neq E_J^\downarrow$ via a different local suppression of the grAl superconducting gap Δ. **b** Embedding the spin modulated JJ into a fluxonium circuit, such as the gralmonium, encodes the spin state in the fluxonium transition frequency f_q. **c** Quantitative feasibility of single-spin detection: Simulation of the qubit frequency shift δf_q for a spin-flip versus distance d from the nanojunction surface for several field bias values $B_\parallel$. Note that for the calculation we used a spin with magnetic moment $\mu = 10\mu_B$ [45] on top of a gralmonium with the circuit parameters corresponding to Section 3.1.3. Adapted from Ref. [2].

that the spin ensemble is large enough or sufficiently coupled to the environment that it embodies a Markovian bath. In contrast, the long-lived TLS environment appears to remain isolated from the spin ensemble, as evidenced by the fits in Fig. 3.12d-f with practically unchanged cross-relaxation rates:

- $\sum_k \Gamma_{qt}^k(B_\parallel = 87.6\,\mathrm{mT}) = 1/33\,\mu\mathrm{s}$
- $\sum_k \Gamma_{qt}^k(B_\parallel = 93.6\,\mathrm{mT}) = 1/33\,\mu\mathrm{s}$
- $\sum_k \Gamma_{qt}^k(B_\parallel = 120\,\mathrm{mT}) = 1/19\,\mu\mathrm{s}$

3.3.2 Towards Longitudinal Coupling to a Single Spin

Revisiting the longitudinal coupling scheme proposed in Section 2.3, we now assess the feasibility of detecting a single spin using a superconducting qubit. As illustrated in Fig. 3.13a, we consider placing a single spin directly atop a grAl nanojunction, which implements a coherent Josephson element confined to a $(20\,\mathrm{nm})^3$ volume. The spin-state dependent local magnetic field threading the nanojunction modulates the grAl superconducting gap $\Delta(B)$ (cf. Eq. (3.3)), resulting in a quadratic suppression of the nanojunction energy E_J and thereby a spin-state dependent Josephson coupling $E_J^\uparrow \neq E_J^\downarrow$. As a result, the Josephson energy becomes a function of both the external bias field $B_\parallel$ (cf. Section 3.2.2) and the spin state σ_z, i.e. $E_J = E_J(B_\parallel, \sigma_z)$. Embedding this spin-sensitive nanojunction into a fluxonium circuit such as the gralmonium encodes the spin state in the qubit frequency, in particular leading to a spin-flip induced qubit frequency shift δf_q at half-flux bias. Importantly, this implements a longitudinal interaction between the spin and the superconducting qubit,

since σ_z commutes with the fluxonium Hamiltonian H_{flux} (Eq. (1.7)). This mechanism leverages the exponential sensitivity of f_q to variations in E_J at half-flux (cf. Eq. (2.4)), as observed in the previous sections via discrete two-level fluctuations of the qubit frequency on different timescales, likely originating from the nanojunction microstructure. Despite this promising development enabled by the nanoscopic confinement of the Josephson element, the magnetic dipole field generated by a single spin decays significantly over tens of nanometers. Thus, to realistically assess the viability of single-spin detection requires to estimate the expected qubit frequency shift δf_q induced by a spin flip in a representative experimental configuration.

We model the spin as a point-like magnetic dipole with a magnetic moment $\mu = 10\mu_B$ oriented (anti-) parallel to the bias field $B_\parallel$. Such spins can be engineered in single molecule magnets with strong anisotropy, forming an effective two-level-system with large magnetic moment [45]. For a spin centered at a distance d from the nanojunction, we numerically evaluate the local gap suppression [204]

$$\frac{\Delta(\vec{B}_\uparrow(\vec{r}) + \vec{B}_\parallel)}{\Delta(0)} = \sqrt{1 - (|\vec{B}_\uparrow(\vec{r}) + \vec{B}_\parallel|/B_c)^2}\,, \tag{3.8}$$

at a position $\vec{r}$ within the $(20\,\text{nm})^3$ nanojunction volume. Following the analogy between Josephson junctions and disordered superconductors (cf. Section 3.1.1 and Section 1.3.3), we treat the nanojunction as a homogeneous superconducting volume. Accordingly, we integrate the local gap suppression in Eq. (3.8) over the nanojunction volume to infer the Josephson energy, assuming $E_J \propto \iiint_{V_{JJ}} d\vec{r}\Delta(\vec{r})$. Specifically, we compute the relative change in nanojunction energy $(E_J^\uparrow - E_J^\downarrow)/E_J^0$ caused by a spin flip, and then numerically solve the fluxonium Hamiltonian (Eq. (1.7)) to determine the resulting qubit frequency shift δf_q at the half-flux sweet spot. The spin-flip-induced E_J-shift is modeled using the gralmonium parameters extracted in Section 3.1.3.

Figure 3.13c shows the simulated δf_q as a function of spin distance d from the nanojunction for different bias fields $B_\parallel$. While the magnetic dipole field generated by the spin decays sharply with distance, the integrated effect across the nanojunction volume remains appreciable up to effective distances comparable to the nanojunction size. This explains the relatively flat dependence of δf_q on spin distance up to $d \sim 10\,\text{nm}$. As expected, δf_q increases significantly with the applied bias field $B_\parallel$, driven by the enhanced susceptibility $\partial\Delta/\partial B \sim B_\parallel/B_c$ of the gap suppression and the intrinsic symmetry $|B_\uparrow| = |B_\downarrow|$ at zero bias field (i.e. only local perturbations of $B_\parallel$ generate a finite δf_q). Consequently, reducing the nanojunction critical field (cf. Fig. 3.7), for example by lowering the grAl resistivity, could amplify the spin-induced δf_q. However, achieving the same Josephson energy E_J under these conditions would necessitate narrower nanojunction confinement, pushing nanofabrication limits. Nonetheless, positioning the spin as close as possible to the nanojunction, at least within $d < 10\,\text{nm}$, and operating in the $B_\parallel \sim 10^2\,\text{mT}$ range enables kHz-level spin-induced qubit frequency shifts (cf. Fig. 3.13c). Given that state-of-the-art superconducting qubits routinely achieve kHz frequency resolution [101, 213, 214], and that advanced frequency detection protocols developed for quantum sensing applications [215, 216] could further enhance this precision, promises to enhance this

resolution, the detection of a spin-state-dependent δf_{q} is well within experimental reach. This supports the prospect of single-shot, QND readout of individual spins via kinetic inductance-mediated longitudinal coupling.

Part II

Device Characterization & Extended Results

4 Details on Longitudinal Spin-Resonator Coupling

In this chapter, we present additional experiments and an extended device characterization supporting the molecular spin ensemble measurements in Chapter 2. We begin by validating the resilience of the grAl resonator to high magnetic fields when interfaced with molecular crystals using vacuum grease. Electron spin resonance (ESR) signatures from the spin ensemble are imprinted in the resonator decay rate and identified as valuable in-situ markers for magnetic field calibration. We further assess the reliability of the background correction method used to extract the ensemble magnetization, presenting an extended magnetization measurement up to 1 T. While the adjacent niobium (Nb) drive resonator induces minor additional frequency shifts in the grAl readout, we demonstrate that these effects do not compromise the accurate extraction of the spin ensemble magnetization. Finally, we present detailed two-tone spectroscopy of the spin ensemble and show that the longitudinal magnetization readout can be reliably distinguished from Kerr-induced shifts in the grAl readout resonator arising from excitation of the Nb drive. These results collectively affirm the compatibility of the grAl-Nb hybrid resonator system with high-field spin ensemble spectroscopy and establish robust protocols for magnetic and spectroscopic calibration in this hybrid platform. This chapter is adapted in parts from Ref. [2].

4.1 Microwave Losses of GrAl and Transverse Coupling

The longitudinal coupling scheme (cf. Section 1.4) preserves both the spin state and the resonator photon number without relying on coherent excitation exchange. Consequently, spin-state readout becomes independent of the spin-resonator detuning and applied magnetic field $B_{\parallel}$, while the always-on coupling introduces no additional losses to either the spin ensemble or the superconducting resonator. We confirm this magnetic field resilience of the grAl resonator in Fig. 4.1.

Microwave loss measurements distinguish between intrinsic mode losses and coupling to external circuitry, captured by the internal and coupling quality factors Q_i and Q_c, respectively. Due to Fano interference in the measurement chain, primarily caused by limited isolation in the microwave circulator, a systematic uncertainty arises in the extracted internal loss rate $\Gamma_\mathrm{i} = \omega_\mathrm{r}/Q_\mathrm{i}$ [4]. This uncertainty manifests as a non-Gaussian error band, spanning from $Q_\mathrm{i,min}$ to $Q_\mathrm{i,max}$ with a median value Q_i (error band and blue markers in Fig. 4.1, respectively). With a high coupling coefficient $Q_\mathrm{i}/Q_\mathrm{c} \approx 10^1 \gg 1$,

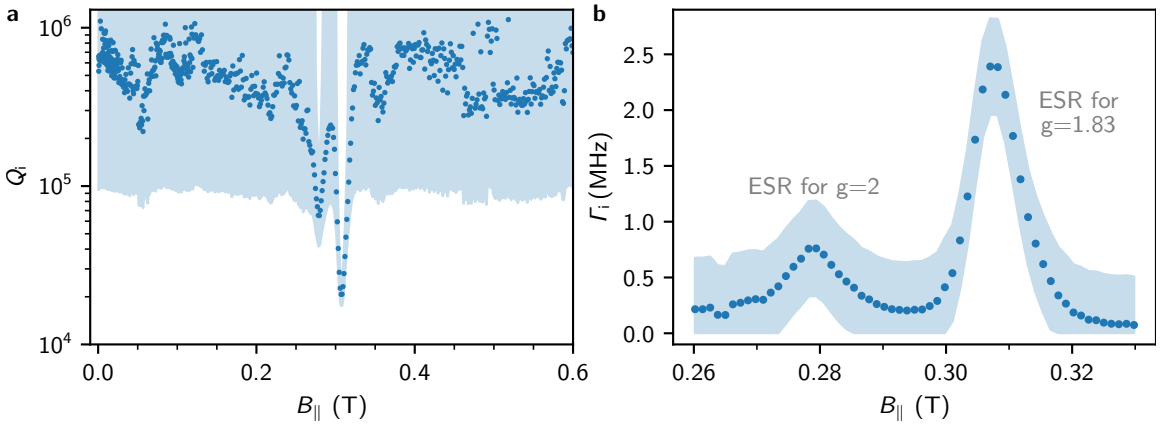

Figure 4.1: GrAl microwave losses in magnetic field $B_\parallel$. **a** Internal quality factor Q_i as a function of in plane magnetic field $B_\parallel$, measured at an average photon number $\bar{n} \approx 10$ with a coupling quality factor $Q_c = 25 \times 10^3$. The shaded region indicates systematic uncertainty introduced by Fano interference in the measurement chain [4]. **b** Internal loss rate $\Gamma_i = \omega_r/Q_i$ near the magnetic fields B_{ESR}, highlighting ESR features from the spin $s = 1/2$, $g = 1.83$ molecular spin ensemble (right peak) and spurious paramagnetic impurities with $g = 2$ spin $s = 1/2$ (left peak), commonly observed in superconducting circuits [134, 135, 139]. The corresponding resonance frequency shift for this measurement is presented in Fig. 4.3. Adapted from Ref. [2].

this uncertainty dominates the microwave loss measurements shown in Fig. 4.1, resulting in an infinite upper bound on Q_i, $Q_{i,max} = \infty$. Importantly, measurements with varying resonator frequency, such as the measurement vs. magnetic field shown in Fig. 4.1, can lead to deceptive trends in the extracted internal quality factor Q_i.

Nonetheless, the extracted internal quality factor remains robust in magnetic field, maintaining a median $Q_i \approx 5 \times 10^5$ and a lower bound of $Q_{i,min} \gtrsim 1 \times 10^5$. Notably, the internal losses of the grAl resonator are not affected by the *Apiezon N* [167] vacuum grease atop the resonator, used to thermalize and attach the molecular crystal (cf. Fig. 2.1). Within the systematic uncertainty, our extracted internal losses (cf. Fig. 4.1) align with previously reported values [4, 72, 124, 145]. Further improvement can be achieved by optimizing the geometry, substrate and cleaning procedure, as recently demonstrated in Ref. [146].

In addition to a moderately fluctuating internal loss baseline (cf. median Q_i in Fig. 4.1a), a pronounced reduction in Q_i is observed at magnetic fields B_{ESR} where the resonator frequency matches the ESR of the $g = 1.83$ spin $s = 1/2$ ensemble (cf. Fig. 4.1a). A second distinct reduction occurs on resonance with ESR of spurious $g = 2$ spin $s = 1/2$ paramagnetic impurities, which are commonly observed in superconducting devices [134, 135, 139] and previously identified in the gralmonium qubits energy relaxation in magnetic field (Fig. 3.9). Figure 4.1b highlights these loss peaks in terms of the internal decay rate $\Gamma_i = \omega_r/Q_i$, which arise from residual transverse coupling of these spin ensembles to the grAl resonator's geometric inductance. The increased losses illustrate the drawbacks of transverse interaction, as it leads to photon loss in the resonator and simultaneously renders the resonator a loss channel for the spin system, since neither the spin state nor the resonator photon number is conserved.

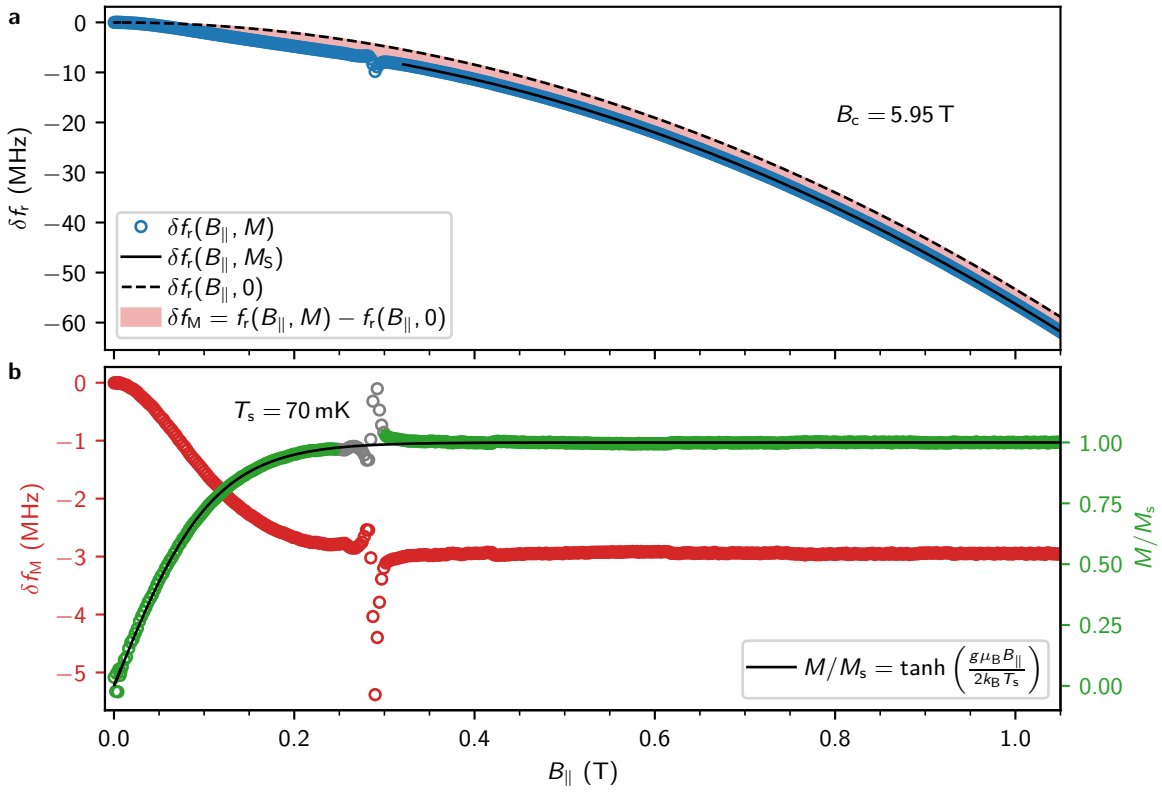

Figure 4.2: Readout of the spin ensemble magnetization up to 1 T. **a** Resonance frequency shift $\delta f_r(B_\parallel, M)$ (blue markers) of the grAl readout resonator and fit to the quadratic tail $\delta f_r(B_\parallel, M_S)$ for saturated crystal magnetization ($B_\parallel > 0.32\,\mathrm{T}$). The fit yields a grAl critical field of $B_c = 5.95\,\mathrm{T}$. **b** Extracted magnetization-induced frequency shift δf_M (red markers and shaded region in **a**), and corresponding crystal magnetization $M \propto \sqrt{\delta f_M}$ (green) up to $B_\parallel = 1\,\mathrm{T}$. Gray markers denote regions affected by hybridization with $g = 2$ and $g = 1.83$ spin ensembles, where reliable magnetization extraction is not possible. Data up to $B_\parallel = 0.6\,\mathrm{T}$ correspond to the magnetization measurements in Fig. 2.2. Adapted from Ref. [2].

Despite these drawbacks, the ESR features serve as precise, in-situ markers for magnetic field calibration and accurate extraction of the molecular spin ensemble's g-factor. Beyond calibrating magnetic field amplitude, we also ensure strict alignment of $B_\parallel$ with the substrate plane, preventing hysteretic or non-monotonic resonance shifts due to perpendicular field components $B_\perp$ which would otherwise obscure extraction of the frequency shift δf_M. The flat internal loss baseline in Fig. 4.1a confirms effective perpendicular field compensation (cf. Appendix B.2), as no degradation in Q_i is observed from spurious microwave modes, which would be introduced by perpendicular magnetic field beyond a certain threshold field [139].

4.2 Additional magnetization curves

To validate the background subtraction method for isolating the magnetization-induced frequency shift δf_M, as introduced in Section 2.2.1, we extend the measurement of the grAl resonator frequency shift $\delta f_r(B_\parallel, M)$ up to $B_\parallel = 1\,\mathrm{T}$, as shown in Fig. 4.2. The commonly

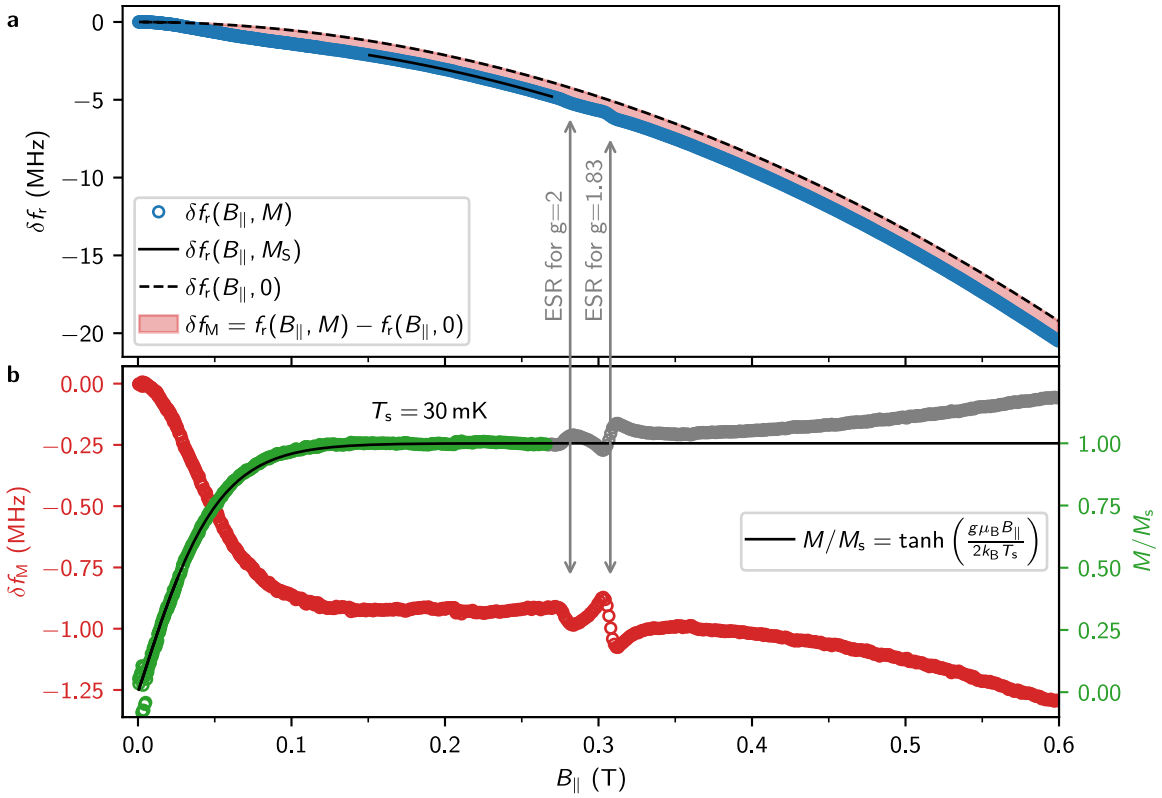

Figure 4.3: Readout of the magnetization in the presence of on-chip Nb drive resonators. **a** Resonance frequency shift $\delta f_r(B_\parallel, M)$ of the grAl resonator (blue markers), composed of a magnetization-induced component δf_M (red shaded area) and a shift $\delta f_r(B_\parallel, 0)$ arising from the suppression of the grAl superconducting gap $\Delta(B_\parallel)$. These contributions are separated by fitting the parabolic tail $\delta f_r(B_\parallel, M_S)$ for saturated spin crystal magnetization ($M = M_S$) in the range $B_\parallel = 150$–270 mT. The adjacent Nb drive resonators (cf. Fig. 2.1) remain undriven during this measurement. **b** Extracted magnetization-induced frequency shift δf_M (red markers and shaded area in **a**) and corresponding crystal magnetization $M \propto \sqrt{\delta f_M}$ (green markers). At $B_\parallel = 0.27$ T, hybridization with $g = 2$ and $g = 1.83$ spins (gray arrows) as well as screening fields from the superconducting Nb structures distort the extracted δf_M, preventing a reliable extraction of the magnetization (gray markers). This measurement provides calibration for the TT spectroscopy shown in Fig. 2.3. Adapted from Ref. [2].

used quadratic approximation of the magnetic-field dependence of the resonator frequency shift (cf. [139])

$$\delta f_r(B_\parallel, M) \approx -\frac{1}{4} f_{r,0} \left(\frac{B_\parallel}{B_c}\right)^2 + \delta f_M \tag{4.1}$$

introduces a systematic deviation of approximately 50 kHz in the extracted δf_M due to its limited accuracy. To improve this, we fit the measured frequency shift at saturated magnetization $\delta f_r(B_\parallel, M_S)$ to the exact form of gap suppression (cf. Eq. (3.3)), yielding

$$\delta f_r(B_\parallel, M) = f_{r,0} \left(\left(1 - \left(\frac{B_\parallel}{B_c}\right)^2\right)^{1/4} - 1 \right) + \delta f_M \,. \tag{4.2}$$

A fit to the parabolic tail using Eq. (4.2) determines a grAl critical field of $B_c = 5.95\,\mathrm{T}$ (cf. Fig. 4.2a). The resulting magnetization-induced shift δf_M, and the inferred normalized magnetization M/M_S remain flat for saturated ensemble magnetization (cf. Fig. 4.2b), confirming the robustness of the background subtraction procedure in isolating spin polarization, independent of spin-resonator detuning.

Figure 4.3 demonstrates that the adjacent Nb drive resonator (cf. Fig. 2.1) does not impede the reliable extraction of ensemble magnetization. The extracted shift δf_M saturates for $B_\parallel \gtrsim 100\,\mathrm{mT}$, consistent with measurements on a sample without the Nb resonator (cf. Fig. 2.2). The saturated frequency shift $\delta f_M(M_S)$ is roughly three times smaller than in Fig. 2.2 due to the use of a slightly smaller molecular crystal[1]. Compared to Fig. 2.2, we also note a slightly earlier saturation of the magnetization in magnetic field. Fitting the magnetization to the paramagnetic response (Eq. (2.3)) yields an effective spin temperature of $T_S = 30\,\mathrm{mK}$, compared to $T_S = 70\,\mathrm{mK}$, extracted for measurements in Fig. 2.2. We attribute this lower spin temperature to the higher surface-to-volume-ratio of the smaller crystal, which enhances phonon decay into the substrate.

For $B_\parallel > 100\,\mathrm{mT}$, an additional shift in δf_M arises from out-of-plane magnetic fields $B_\perp$ generated by screening currents in the niobium structures of the drive resonators. These shifts persist even when extending the fit range for superconducting gap suppression, though they are partially averaged out due to symmetric deviations. Importantly, the ensemble remains saturated at high fields, as shown in Fig. 4.2. We therefore use δf_M at saturated magnetization as a reference for the TT spectroscopy in Fig. 2.3.

4.3 Spin Ensemble Two-Tone Spectroscopy

In this section, we demonstrate that the longitudinal readout of the spin ensemble excitation can be unambiguously distinguished from parasitic Kerr interaction when driving the spins via the Nb drive resonator. Figure 4.4 presents continuous-wave TT spectroscopy on the molecular spin ensemble, where we monitor the frequency shift δf_r of the grAl readout resonator, while applying a drive tone f_d near the fundamental mode of the Nb drive resonator, $f_{Nb1} = 9.84\,\mathrm{GHz}$.

Two distinct mechanisms contribute to the observed shift δf_r of the grAl resonance. First, excitation of the fully polarized spin ensemble results in a positive frequency shift, reversing the magnetization-induced shift δf_M. This effect is consistent with the magnetization curve shown in Fig. 4.3. Second, a negative shift arises from a cross-Kerr interaction between the fundamental modes of the Nb and grAl resonators when driving the Nb resonator. These opposite signatures, positive for spin excitation and negative for Kerr-induced shift, allow clear separation of the two effects. As shown in Fig. 4.4, the Kerr-induced negative shift is most pronounced when f_d lies within the Nb resonator linewidth ($\kappa/2\pi = 2\,\mathrm{MHz}$).

[1] To prevent degradation of the molecular crystal from thermal cycling, we replace the crystal between successive cooldowns.

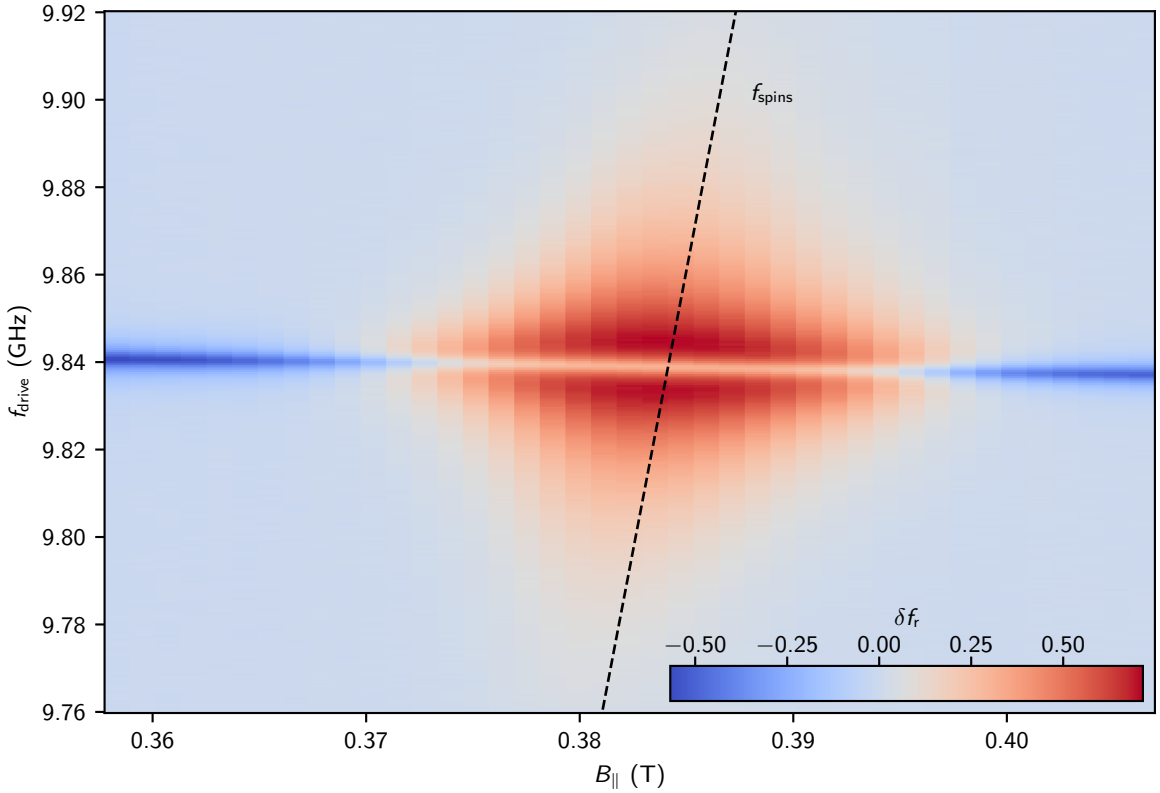

Figure 4.4: Two-tone spectroscopy of the spin ensemble 2 GHz detuned from the readout. A continuous-wave drive tone at frequency f_{d} is applied near the fundamental mode of the Nb resonator $f_{\mathrm{Nb1}} = 9.84\,\mathrm{GHz}$, while monitoring the frequency shift δf_{r} of the grAl resonator at $f_{\mathrm{r}} = 7.87\,\mathrm{GHz}$. The dashed line indicates the expected spin transition frequency $\mathrm{h}f = g\mu_{\mathrm{B}}B_{\parallel}$ with $g = 1.83$. A negative frequency shift (blue) results from the cross-Kerr interaction between modes of the driven Nb resonator and the grAl resonator, most pronounced for f_{d} within the linewidth $\kappa/2\pi = 2\,\mathrm{MHz}$ of the Nb mode around its resonance f_{Nb1}. In contrast, excitation of the initially polarized spin ensemble induces a positive shift (red). The strongest spin-induced response occurs when the drive tone is resonant with both the spin transition and the Nb resonator.

Simultaneously, the spin transition $\mathrm{h}f = g\mu_{\mathrm{B}}B_{\parallel}$ tunes through the Nb resonance, generating a positive shift in δf_{r}. On resonance, these contributions partially overlap, producing a characteristic narrow dip at the center of the spin-induced feature.

To isolate the spin contribution, we calibrate the drive-frequency-dependent Kerr background by measuring δf_{r} with the spin transition far detuned from the drive (e.g. at $B_{\parallel} = 0.36\,\mathrm{T}$ in Fig. 4.4). This reference is subtracted from all datasets. The resulting corrected shift δf_{r} is then converted into a relative magnetization change $\delta M/M_{\mathrm{S}}$ using the calibration curve from Fig. 4.3, yielding the spin excitation pattern presented in Fig. 2.3a.

5 Gralmonium Qubit Characterization

In this chapter, we provide an additional extensive characterization of the gralmonium qubit. First, we introduce a rapid in-situ method to identify the operating regime of the grAl nanojunction based on resonator flux sweep measurements. We then assess the current-phase relation of the nanojunction embedded within the gralmonium circuit and provide a comprehensive analysis of the qubit frequency fluctuations on multiple timescales. By combining time-domain measurements and two-tone spectroscopy, we establish the nanojunction as the origin of these fluctuations and model them through variations in the Josephson energy. Finally, we present an extended time-domain characterization of the qubit, including coherence measurements at zero- and half-flux bias. We quantify the impact of flux noise and photon shot noise on qubit dephasing and analyze individual quantum jumps of the qubit. This chapter is adapted in parts from Ref. [3].

5.1 In-Situ GrAl Nanojunction Characterization

The first indication of a gralmonium qubit operating at the desired frequency range is the observation of periodic avoided level crossings with the readout resonator, as discussed in Section 3.1.3. These crossings, evident in the extended resonator flux sweep in Fig. 5.1, repeat periodically as a function of the applied external flux Φ_{ext}. This periodicity, which matches the area of the qubit flux loop, serves as a robust signature of coherent qubit-resonator coupling, clearly distinguishing it from spurious interactions with potentially magnetic-field-sensitive TLS or other parasitic modes [144]. In addition to the avoided crossings, the resonator frequency is suppressed by 200 kHz over ten flux periods in Fig. 5.1 due to screening currents in the resonator.

Figure 5.2 further illustrates how flux-dependent avoided level crossings provide a rapid diagnostic of the grAl nanojunction regime. We compare flux sweeps from three devices, all fabricated on the same chip and sharing nominally identical nanojunction designs. The observed regimes - ranging from excessively wide grAl confinement, through fluxonium junctions in the desired regime, to electrically disconnected junctions - arise from variability in the fabrication process (cf. Section 3.1.1 and Appendix A.2). To address this variability and improve yield, multiple gralmonium devices are patterned per chip, typically yielding one operational qubit per chip.

Figure 5.2a shows the flux sweep of a device with excessively wide grAl confinement, exhibiting no avoided level crossings and a resonator frequency shift of $\delta f_{\text{r}} = 1\,\text{MHz}$. This is explained by the high sensitivity of the nanojunction $E_{\text{J}}/E_{\text{C}}$ ratio to the nanojunction

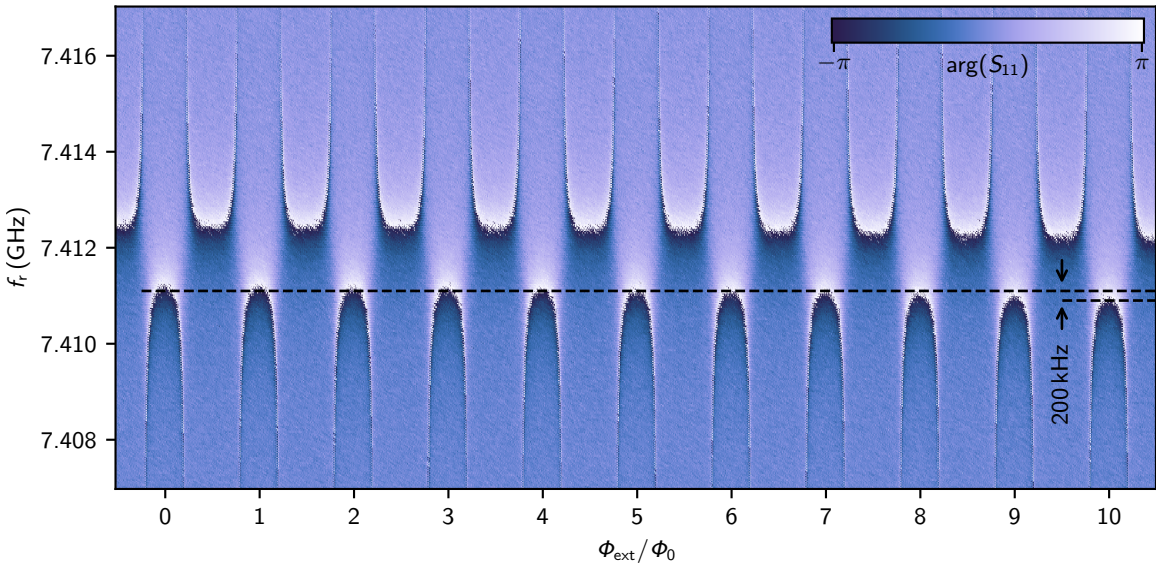

Figure 5.1: Periodicity of avoided level crossings in the qubit flux sweep. Readout resonator phase response $\arg(S_{11})$ in the vicinity of the resonance frequency f_r, measured as a function of external flux Φ_{ext}. The extended flux sweep up to $\Phi_{ext}/\Phi_0 = 10$ displays strictly periodic qubit-resonator avoided level crossings. The systematic shift by $\delta f_r(10\,\Phi_0) \approx 200\,\text{kHz}$ (dashed lines) is attributed to screening currents in the antenna (cf. Section 2.2.1). This dataset was acquired during a previous thermal cycle (cooldown #3 in Fig. 5.6), resulting in a 2.5 MHz higher resonator frequency than that reported in Section 3.1. Adapted from Ref. [3].

width ε. For too wide nanojunctions leading to $E_J/E_C \gg 1$, quantum fluctuations of the phase are suppressed. The applied magnetic flux instead generates persistent currents in the flux loop, shifting the resonator frequency, reminiscent of the magnetically induced shifts observed in grAl resonators coupled to spin ensembles in Chapter 2. Notably, the $\delta f_r = 1\,\text{MHz}$ shift exceeds the screening-induced frequency modulations shown in Fig. 5.1. Indeed, the corresponding SEM image (cf. Fig. 5.2b) confirms an excessively wide nanojunction confinement width of $\varepsilon \approx 50\,\text{nm}$.

In contrast, the flux sweep presented in Fig. 5.2c displays clear periodic avoided level crossings (with no δf_r shift visible in this flux range). The corresponding nanojunction (Fig. 5.2d) features a confinement width of $\varepsilon \approx 20\,\text{nm}$, placing it within the optimal operating regime comparable to the devices characterized in Fig. 3.2 and Fig. 3.5. Finally, devices with interrupted nanojunctions (Fig. 5.2f) exhibit no flux dependence in the resonator response, consistent with the absence of qubit-resonator interaction.

5.2 Sinusoidal Current Phase Relation of the Nanojunction

While the sinusoidal CφR defined in Eq. (1.4) is widely employed to model JJs in superconducting quantum circuits, it represents an approximation valid in the limit of many low-transparency conduction channels. This condition is typically met in conventional tunnel junctions, where a thin oxide barrier ensures low transparency. In contrast, other

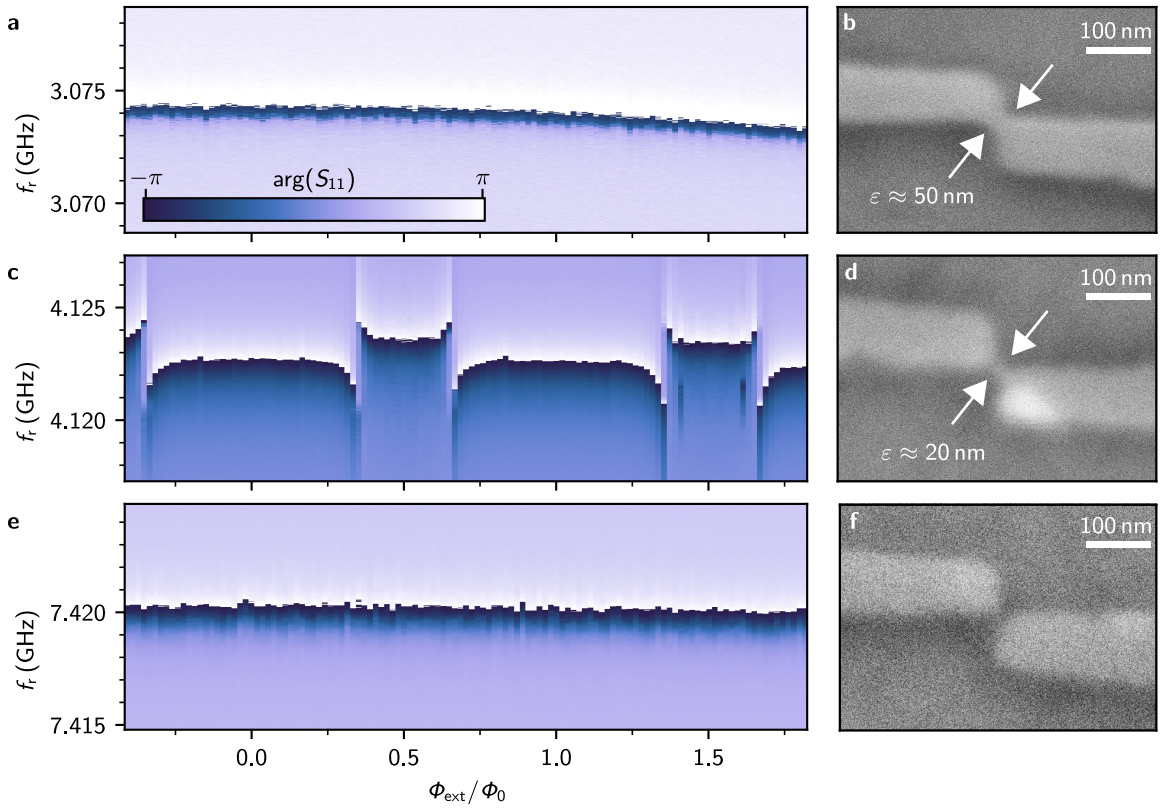

Figure 5.2: GrAl nanojunction regimes. **a, c, e** Readout resonator phase response arg(S_{11}) as a function of external flux Φ_{ext} for three nominally identical grAl nanojunctions, embedded into qubit circuits on the same chip. **b, d, f** SEM micrograph of the grAl nanojunction corresponding to the flux sweeps in the left column, imaged after the cooldown. **a, b** Excessively wide grAl confinement: A confinement width of $\varepsilon \approx 50$ nm results in large screening currents in the flux loop and a consequent reduction of the resonator frequency. **c, d** Optimized grAl confinement for fluxonium JJ: A confinement of $\varepsilon \approx 20$ nm yields well-defined periodic avoided level crossings between the qubit and resonator, consistent with a conventional fluxonium JJ. **e, f** Disconnected grAl electrodes: An interrupted nanojunction results in a flat resonator frequency response (apart from small shifts due to screening currents in the antenna, cf. Fig. 5.1). Adapted from Ref. [3].

types of weak links with higher transparency channels exhibit slanted CφRs characterized by contributions from higher-order harmonics (e.g. $\sin(2\varphi)$, $\sin(3\varphi)$) in the CφR, corresponding to the coherent tunneling of multiple Cooper pairs [92].

Notably, even conventional Al/AlO_x/Al tunnel junctions have recently been shown to deviate slightly from a purely sinusoidal CφR, likely originating from inhomogeneity of the oxide barrier or from an inductive contribution of the leads, or both. As we report in Ref. [8], higher harmonics propagate into the EφR, subtly modifying the energy spectrum of superconducting qubits and influencing key qubit properties such as anharmonicity and charge dispersion.

In Section 3.1 we modeled the grAl nanojunction as a single effective JJ with sinusoidal CφR. The good agreement between the fit to the fluxonium Hamiltonian H_{flux} (Eq. (1.7)) and the measured gralmonium spectroscopy provides preliminary support for this approximation. To more rigorously assess its validity, we quantify how well the conventional sinusoidal

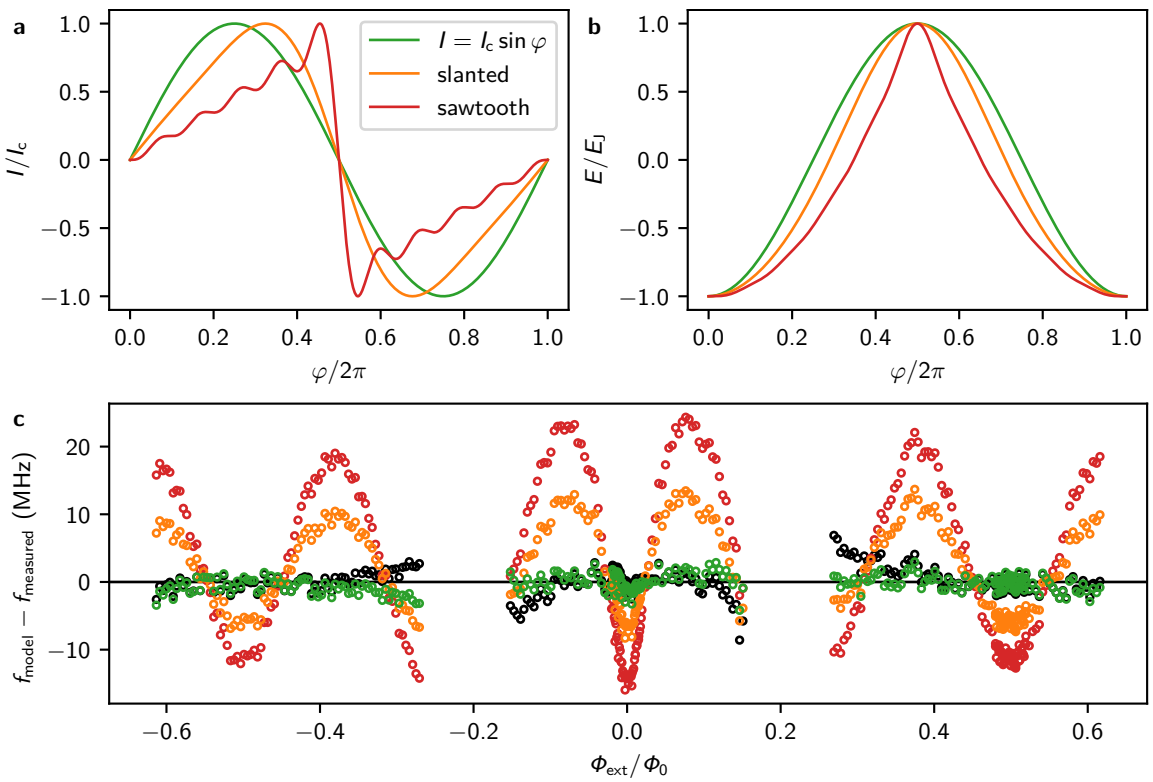

Figure 5.3: Modeling the nanojunction current-phase-relation (CφR). **a** Modeled current-phase-relations (CφRs) for the nanojunction, showing the normalized current I/I_c as a function of the phase φ across the junction. In addition to the ideal sinusoidal relation for an SIS junction, $I = I_c \sin(\varphi)$ (green, Eq. (1.4)), two modified CφRs incorporating higher-order Josephson harmonics are considered: a slanted CφR $I = I_c(\sin\varphi - 0.25\sin 2\varphi + 0.05\sin 3\varphi)$ (orange), and a sawtooth-like CφR approximated by the Fourier series $I = I_c \sum_{n=1}^{10}(-1)^{(n+1)} \sin(n\varphi)/n$ (red). **b** Corresponding energy-phase-relations (EφRs), plotted as the normalized junction energy E/E_J as a function of phase φ. **c** Deviation between the measured qubit transition frequency $f_{measured}$ and the model predictions f_{model}. The latter are obtained by substituting the EφRs into the standard fluxonium Hamiltonian H_{flux} (Eq. (1.7)) and fitting it to $f_{measured}$, using a numerical diagonalization of the respective Hamiltonian. For the standard sinusoidal CφR, fits are performed for both the fully coupled qubit-resonator system (green) as well as the qubit only (black), enabling direct comparison with the higher-harmonic models (orange and red), for which coupled fits are computationally prohibitive. Data within a ±1 GHz interval of the qubit-resonator avoided level crossing ($|\Phi_{ext}/\Phi_0| \approx 0.2$) are excluded from the fit. The residual discrepancy between the purely sinusoidal CφR-model and the experiment constrains higher-order Josephson harmonics in the nanojunction CφR to $\leq 5\%$, limited by the resolution of the measured qubit spectroscopy. Adapted from Ref. [3].

CφR in H_{flux} describes the gralmonium qubit and specifically the nonlinearity of the grAl nanojunction.

Using the spectroscopy data presented in Fig. 3.3, we fit a model to a numerical diagonalization of H_{flux}, incorporating three different CφR (specifically their respective EφR) (cf. Fig. 5.3a, b). In addition to the purely sinusoidal CφR, we construct a slightly slanted CφR with small second and third harmonic contributions and one resembling a sawtooth pattern containing higher harmonics up to tenth order, $\sin(n\varphi)$ ($n > 1$) [8, 92]. The diagonalization is performed for each CφR individually, using an extension of the numerical diagonalization used for the standard fluxonium Hamiltonian in Eq. (1.7). For the sinusoidal

case, we fit both the coupled qubit-resonator system and the qubit alone. In contrast, for the more complex CφRs with higher harmonics, we restrict the fit to the qubit system due to computational limitations.

In Fig. 5.3c, we present the deviation between the modeled $|g\rangle \rightarrow |e\rangle$ transition and the measured qubit spectrum. Remarkably, the model using a standard $\sin(\varphi)$-CφR matches the measured qubit spectrum within 2 MHz. In contrast, the models incorporating higher harmonics exhibit significant systematic deviations that exceed the spread in the experimental data. Based on the spread of the measured $|g\rangle \rightarrow |e\rangle$ transitions, we infer an upper bound of 5% on the amplitude of higher-order Josephson harmonics in the CφR of the grAl nanojunction, limited by the resolution of the spectroscopy. This bound can be refined with further measurements improving the resolution of the qubit spectroscopy by using the computational methods presented in Ref. [8]. Importantly, the magnitude of higher harmonic contributions in the grAl junction appears comparable to those in conventional SIS tunnel junctions, reinforcing the notion that grAl nanojunctions exhibit effective SIS JJ characteristics.

5.3 Fluctuations of the Gralmonium

In this section, we analyze the conspicuous fluctuations of the gralmonium qubit frequency initially observed in the Ramsey measurement in Section 3.1.3. As shown in Fig. 5.4a, Ramsey fringes obtained at half-flux bias exhibit a beating pattern with a beating frequency of $f_{\text{beating}} = 0.2\,\text{MHz}$, corresponding to discrete toggling of the qubit frequency between two values separated by 0.2 MHz. These fluctuations occur on a timescale faster than the acquisition time of a single data point, i.e. 100 single-shot qubit measurements of the same Ramsey sequence with delay time τ, placing an upper bound on the order of milliseconds. At the same time, the fluctuations must be slower than individual single-shot Ramsey measurements, as faster fluctuations would average out, resulting in a single effective detuning without a visible beating pattern. This constrains the switching rate to lie between the inverse Ramsey acquisition time and the Ramsey coherence time $1/T_{2\text{R}}$.

On a timescale of minutes, the qubit frequency additionally exhibits discrete jumps of $\delta f_{\text{q}} = 1.5\,\text{MHz}$, which is visible both in the continuous-wave TT spectroscopy in Fig. 3.3 and in the two Ramsey measurements in Fig. 5.4a, performed under nominally identical conditions. Note that the dwell time at both qubit frequencies is not identical, as shown in the inset in Fig. 5.4a. This is similar to the case of the beating pattern, where non-equivalent dwell times lead to imperfect destructive interference. To quantify the dynamics of these fluctuations, we compute the power spectral density (PSD) of the qubit frequency evolution using:

$$S(f) = \mathcal{F}^2(f_{01}) \cdot 2T\,, \tag{5.1}$$

where $\mathcal{F}(f_{01})$ is the normalized discrete Fourier transform and T is the total measurement duration. Using a two-frequency fit, Ramsey and beating frequencies (f_{Ramsey} and f_{beating}) are extracted for 400 contiguous Ramsey measurements, spanning a total duration of

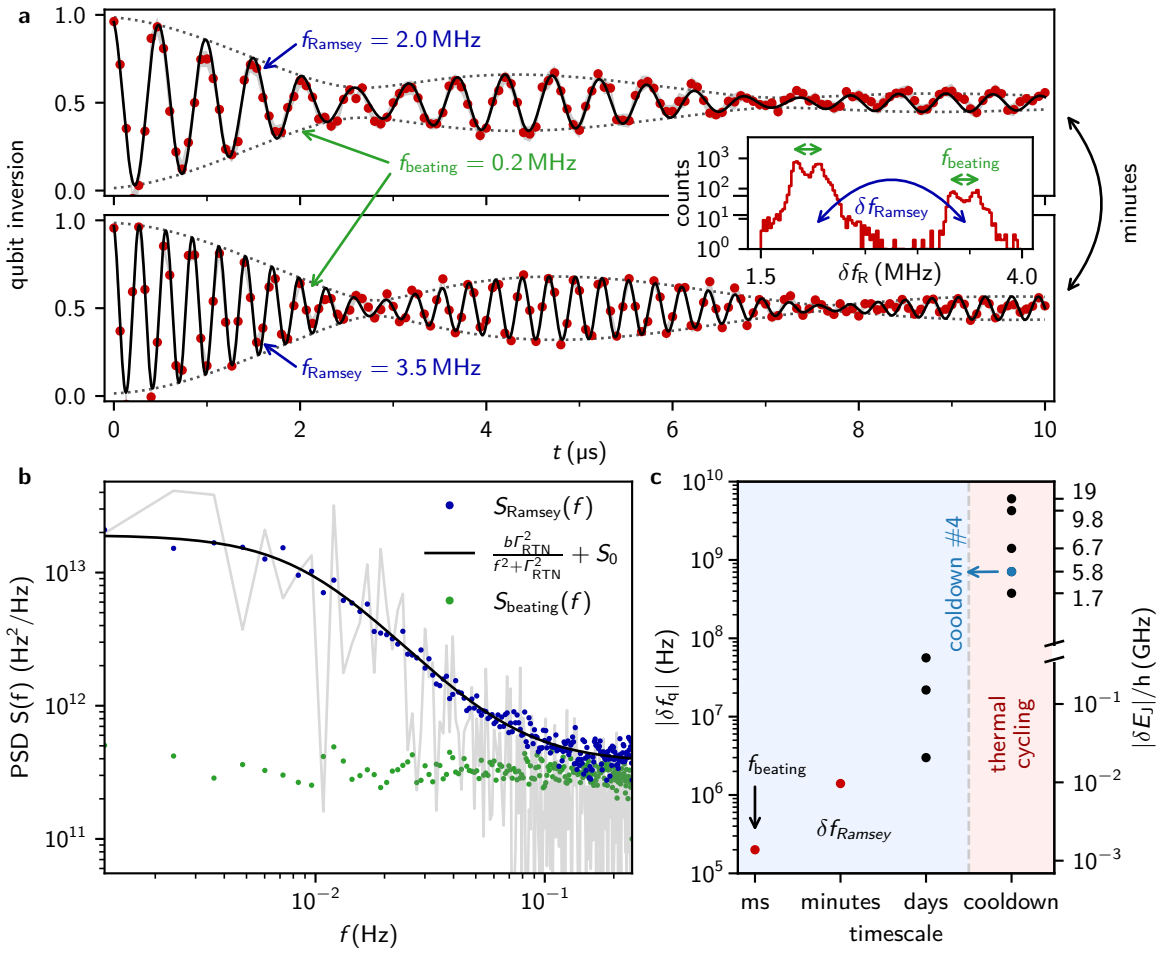

Figure 5.4: Nanojunction induced qubit frequency fluctuations across timescales. **a** Ramsey fringes measured at a nominal detuning $f_{\text{Ramsey}} = 2\,\text{MHz}$ exhibit a beating pattern, indicating bistable switching of the qubit frequency by $f_{\text{beating}} = 0.2\,\text{MHz}$ (dotted lines), extracted using a two-frequency fit (black lines). Over a timescale of minutes, repeated measurements acquired under identical conditions display a shift in the average Ramsey frequency to $f_{\text{Ramsey}} = 3.5\,\text{MHz}$, corresponding to a discrete jump of $\delta f_{\text{Ramsey}} = 1.5\,\text{MHz}$. **Inset:** Histogram of the extracted qubit detuning frequencies from 5000 Ramsey experiments, showing both components of the two-frequency fit at $\delta f^{\text{R}} = f_{\text{Ramsey}} \pm f_{\text{beating}}/2$. **b** Power spectral density (PSD) $S(f)$ of the gralmonium frequencies f_q extracted from two-frequency fits across 400 contiguous Ramsey measurements. The PSDs of f_{Ramsey} and f_{beating} ($S_{\text{Ramsey}}(f)$ and $S_{\text{beating}}(f)$) are averaged over 85 repetitions, shown as blue and green markers, respectively. A representative individual trace is shown in light gray. A Lorentzian fit yields a random telegraph noise (RTN) switching rate $\Gamma_{\text{RTN}} = 9.4\,\text{mHz}$, amplitude $b = 1.89 \times 10^{13}\,\text{Hz}^2/\text{Hz}$ and white noise floor of $S_0 = 3.73 \times 10^{11}\,\text{Hz}^2/\text{Hz}$. **c** Overview of discrete qubit frequency fluctuations across different timescales: The beating pattern in the Ramsey fringes corresponds to a qubit frequency toggling on a ≤ milliseconds timescale, while the detuning shift of $\delta f_{\text{Ramsey}} = 1.5\,\text{MHz}$ occurs on a minutes timescale (see panels a, b). Additional jumps by $\delta f_q \approx 10$–$100\,\text{MHz}$ are detected every few days during cooldown, and the largest shifts by $\delta f_q \sim$ GHz occur following thermal cycling of the cryostat to room temperature (cf. Fig. 5.6). These fluctuations are attributed to discrete changes in the nanojunction energy δE_J, as demonstrated in Fig. 5.5. Adapted from Ref. [3].

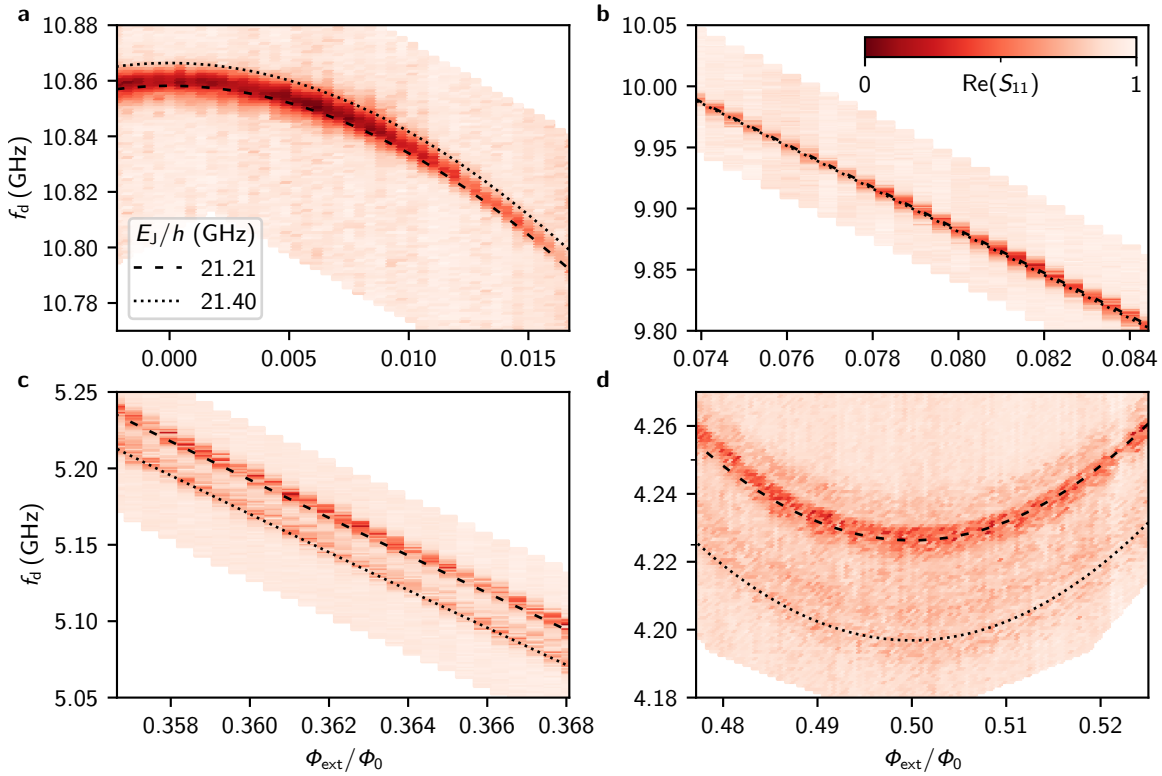

Figure 5.5: Identification of E_J toggling as the source of gralmonium frequency fluctuations. TT spectroscopy of the gralmonium qubit as a function of external flux Φ_{ext} reveals two distinct qubit frequency branches across the full flux range. These branches are well described by fits using identical qubit parameters E_C and E_L, but differing Josephson energies E_J, separated by $\delta E_J = 190\,\text{MHz}$, as indicated by the dashed and dotted curves. The relative visibility of the spectral branches varies during the measurement, reflecting fluctuations in dwell time of the qubit occupying either energy branch. **a** At zero-flux $\Phi_{ext}/\Phi_0 = 0$, the frequency difference between the two qubit spectra is $\delta f_q = 7.4\,\text{MHz}$. **b** The two branches cross at $\Phi_{ext}/\Phi_0 \approx 0.08$, consistent with model predictions. **c** Towards half-flux, two distinct qubit frequencies are visible again, with the model predictions inverted compared to zero flux (dashed above dotted curve). **d** The largest splitting occurs at half-flux $\Phi_{ext}/\Phi_0 = 0.5$ ($\delta f_q = 30\,\text{MHz}$) and multiple transition lines become visible. This spectroscopy measurement was acquired during a previous cooldown (#3 in Fig. 5.6), without a parametric amplifier, using a sweep time of 50 s per trace across 100 drive frequencies f_d. The color scale encodes the in-phase component of the reflection coefficient $\text{Re}(S_{11})$, rescaled to the $0-1$ interval for visual clarity. Adapted from Ref. [3].

$T = 832\,\text{s}$. Shown in Fig. 5.4b, the resulting averaged power spectrum, displays a Lorentzian profile, characteristic for random telegraphic noise (RTN), which can be described by

$$S(f) = \frac{b\Gamma_{\text{RTN}}^2}{f^2 + \Gamma_{\text{RTN}}^2} + S_0\,. \tag{5.2}$$

Here, Γ_{RTN} is the switching rate, b the amplitude and S_0 the frequency independent white noise floor. A fit to $S_{\text{Ramsey}}(f)$ reveals a switching rate of $\Gamma_{\text{RTN}} = 9.4\,\text{mHz}$, quantifying the timescale of the qubit frequency toggling. In contrast, the PSD of the beating frequency $S_{\text{beating}}(f)$ is frequency independent, consistent with white noise and indicating no additional structure beyond the toggling itself.

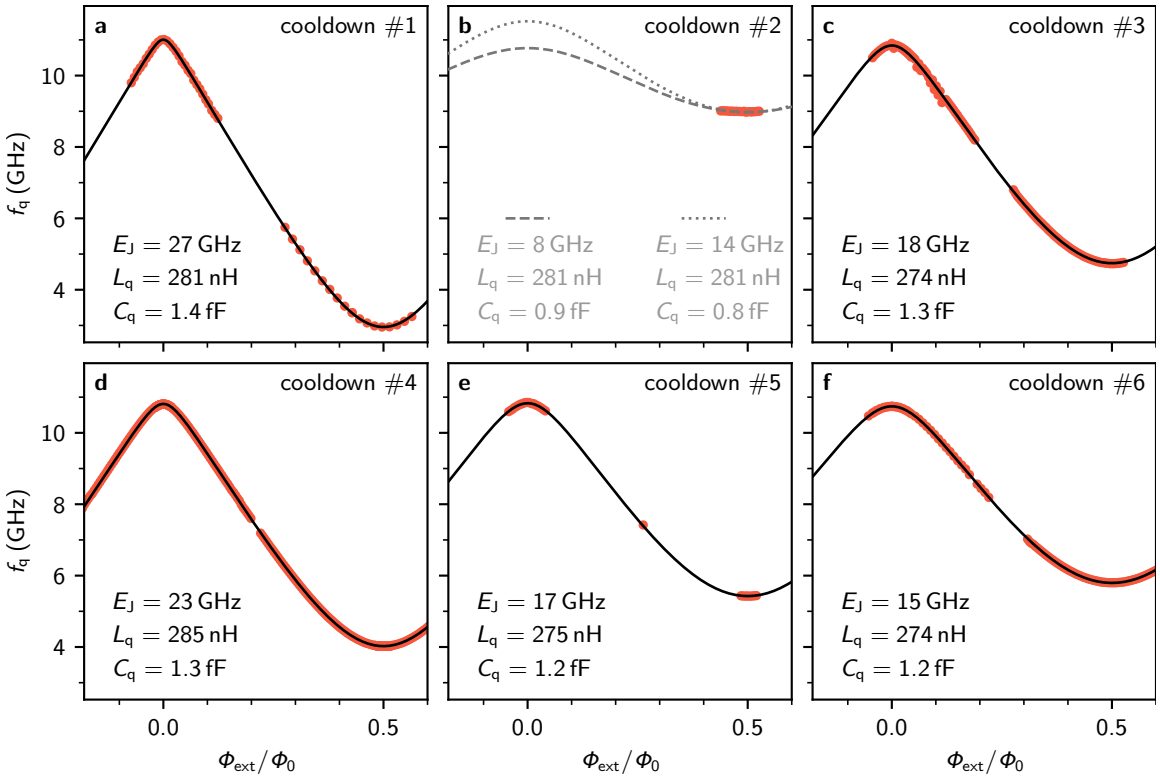

Figure 5.6: Gralmonium spectra across successive cooldowns. Extracted $|g\rangle \rightarrow |e\rangle$ qubit transition frequencies (blue markers), measured for the same device in consecutive cooldowns. The half-flux qubit frequency shifts δf_q between cooldowns are summarized in Fig. 5.4c. The black lines represent fits based on numerical diagonalization of the fluxonium Hamiltonian H_{flux} (Eq. (1.7)). Changes in E_J and C_q appear correlated; however, C_q remains constrained by the geometric shunt capacitance $C_{||}$. In contrast, the qubit inductance L_q remains constant within few percent. Cooldown #4 corresponds to the data presented in Section 3.1. **b** Gray dashed and dotted lines indicate model spectra using the L_q value from cooldown #1 and a capacitance close to the lower limit of $C_{||} \approx 0.8$ fF. In this cooldown, measurements were limited to a narrow flux range near $\Phi_{ext}/\Phi_0 \approx 0.5$, preventing an unambiguous fit of the full qubit spectrum. Adapted from Ref. [3].

Beyond these two fluctuation-timescales, we also observe jumps of the qubit frequency on the order of $\delta f_q = 10\text{–}100$ MHz every few days while the sample remains at cryogenic temperatures. The largest qubit frequency shifts, up to $\delta f_q \sim$ GHz, occur after cycling to room temperature. Importantly, these changes persist even when the cryostat remains under vacuum, ruling out post-fabrication oxidation effects. A summary of frequency fluctuations across timescales is presented in Fig. 5.4a.

We attribute all observed frequency fluctuations to variations in the nanojunction energy E_J due to the exponential sensitivity of the qubit frequency at half-flux bias on E_J/E_C. In addition, we expect a higher impact of E_J variations on the qubit frequency, since the value of E_C is bounded by the geometric shunt capacitance $C_{||}$ (cf. Section 3.1.3). We confirm that the discrete fluctuations stem from intrinsic variations in the Josephson energy rather than for instance transverse coupling to a fixed-frequency TLS, by analyzing the dependence of the toggling amplitude on the qubit frequency.

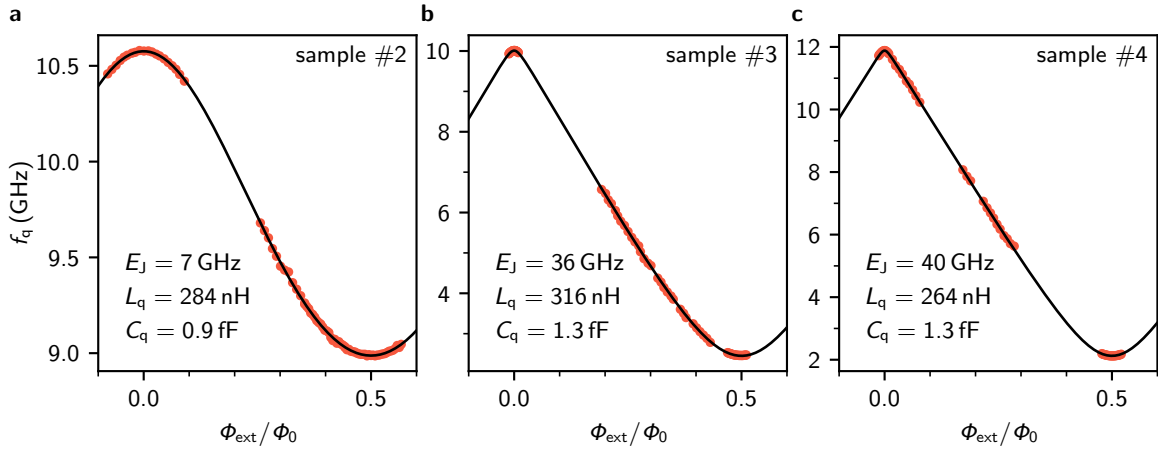

Figure 5.7: Gralmonium spectra for additional samples with nominally identical design. Extracted $|g\rangle \rightarrow |e\rangle$ qubit transition frequencies (blue markers) for gralmonium devices fabricated on a separate chip but with the same nominal design. The black lines represent fits obtained via numerical diagonalization of the fluxonium Hamiltonian H_{flux} (Eq. (1.7)). Adapted from Ref. [3].

The toggling signatures are visible in continuous-wave TT spectroscopy versus flux when the averaging time per flux-trace is comparable to the toggling timescale. This manifests as apparent frequency jumps between adjacent traces, as visible in the raw TT spectroscopy in Fig. 3.3. Figure 5.5 illustrates this concept for an averaging time increased by one order of magnitude, resulting from measurements acquired without a parametric amplifier during previous cooldown of the same sample. Under these conditions, the toggling becomes resolvable within individual flux traces, appearing as two distinct qubit transitions. Importantly, these two frequencies can be tracked across the entire qubit flux range, ruling out transverse coupling to parasitic TLS with a fixed transition frequency. To confirm the nanojunction as the source of these fluctuations, we fit the two observed branches using the fluxonium Hamiltonian H_{flux}, differing only in their value of the Josephson energy E_J.

We corroborate the nanojunction at the origin of the conspicuous fluctuations by modeling the two qubit lines with two fits to the fluxonium Hamiltonian H_{flux}, differing only in their value of the Josephson energy E_J. The resulting model accurately captures the spectral evolution of both frequency branches across the full flux range, including the merging of the two branches at $\Phi_{ext}/\Phi_0 \approx 0.08$ (Fig. 5.5b), as well as the inversion in frequency ordering between zero and half-flux bias, visible in Fig. 5.5a and Fig. 5.5c.

We conclude the discussion on the qubit frequency fluctuations by analyzing the changes of the qubit frequency between cooldowns. Figure 5.6 displays the extracted qubit spectra for the same device across six successive cooldowns. Fits to the fluxonium Hamiltonian H_{flux} (Eq. (1.7)) reveal that the most significant variation occurs in the Josephson energy E_J. These changes appear correlated with smaller variations observed in the qubit capacitance C_q. However, since C_q is bounded by the geometric shunt capacitance $C_{\parallel} \approx 0.8\,\text{fF}$, the gralmonium charging energy is limited to values below $E_C \leq E_C^{\parallel} \approx 24\,\text{GHz}$. Across

cooldowns, the vastly different qubit spectra include positive as well as negative shifts of E_J, excluding progressive device degradation, such as aging, as a source of the fluctuations.

Over the course of the gralmonium characterization, we have measured more than 20 functioning gralmonium devices across 11 wafers. From fits to H_{flux}, we confirm a sinusoidal CφR adequately describes the nanojunction nonlinearity across all devices. Figure 5.7 presents three representative spectra and their corresponding fits. In Fig. 5.7a, the Josephson energy of the grAl nanojunction is sufficiently small to lift the entire qubit spectrum of the $|g\rangle \rightarrow |e\rangle$ transition to the 10 GHz range. While the spectrum in Fig. 5.7a is similar to the one measured in cooldown #2 in Fig. 5.6b, the spectra in Fig. 5.7b, c exhibit qubit parameters similar to the gralmonium device analyzed in Section 3.1 (see Fig. 5.6d). Notably, the spread of the Josephson energies across devices (7–40 GHz) is similar to variations in nanojunctions for successive cooldowns (8–27 GHz).

5.4 Extended Time-domain Characterization

5.4.1 Decoherence budget at half-flux bias

In the following, we analyze the Hahn echo decoherence around half-flux bias $\Phi_{\text{ext}}/\Phi_0 = 1/2$. Consistent with the results presented in Section 3.3.1, we observe a Gaussian decay component in the Hahn echo signal when the qubit is biased away from the sweet spot $\Phi_{\text{ext}}/\Phi_0 \neq 0.5$, which aligns with the expectations for $1/\omega$ flux-noise-induced dephasing [30–34, 177, 195]. Accordingly, we employ the same fit procedure as presented in Section 3.3.1: for every set of Hahn echo decay measurements vs. flux, we perform a joint fit, extracting a flux-dependent Gaussian decay envelope with decay rate $\Gamma_{\varphi\text{E}}^{\Phi}$ on top of a flux-independent exponential decay with $\Gamma_{\text{exp}} = \Gamma_1/2 + \Gamma_{\varphi\text{E}}^{\text{const}}$

$$P_{|e\rangle}(t) = \frac{1}{2}\left(e^{-(\Gamma_{\varphi\text{E}}^{\Phi} t)^2} \cdot e^{-(\Gamma_1/2+\Gamma_{\varphi\text{E}}^{\text{const}})t}\right) + \frac{1}{2} \tag{5.3}$$

Figure 5.8 shows the extracted Gaussian dephasing rates, averaged over five consecutive flux sweeps. As expected, the Gaussian contribution vanishes at the sweet spot ($\Phi_{\text{ext}}/\Phi_0 = 1/2$), where the qubit is first-order insensitive to flux noise. We fit the linear dependence of $\Gamma_{\varphi\text{E}}^{\Phi}$ on flux using the model introduced in Eq. (3.5), assuming a $1/\omega$ flux noise power spectral density, $S_\Phi(\omega) = 2\pi A_\Phi/\omega$ (cf. Fig. 5.8). This yields a flux noise amplitude $\sqrt{A_\Phi} = 26\,\mu\Phi_0$, comparable to the flux noise amplitudes in zero magnetic field extracted in Fig. 3.11, but one order of magnitude larger than typically observed in JJ array flux qubits [30–32, 34, 177].

The presented analysis is based on the assumption that the exponential decay rate Γ_{exp} is independent of external flux. This assumption is supported by the measured energy relaxation rates (blue in Fig. 5.8) corresponding to an average relaxation of $\bar{\Gamma_1} = 0.075$ MHz. Minor deviations of $\Gamma_{\varphi\text{E}}^{\Phi}$ from the linear trend, particularly in the vicinity of $\Phi_{\text{ext}}/\Phi_0 = 0.48$, appear correlated with a locally increased energy relaxation Γ_1.

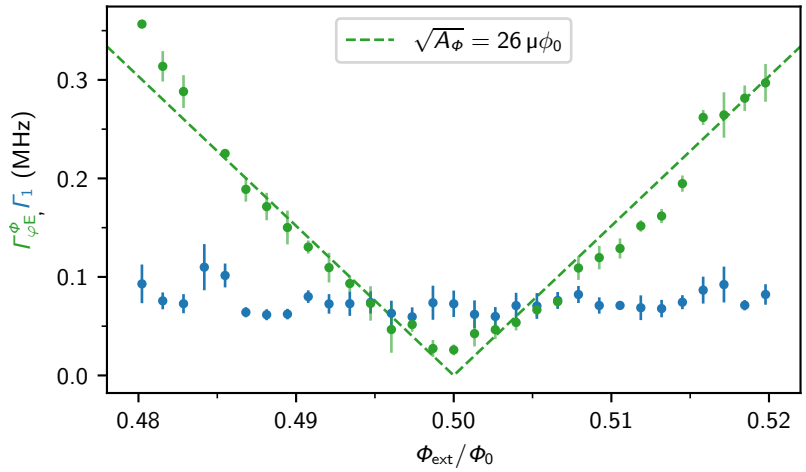

Figure 5.8: Gralmonium decoherence near half-flux bias. Flux noise Hahn echo dephasing rate $\Gamma^{\Phi}_{\varphi E}$ (green), and energy relaxation rate Γ_1 (blue), measured in the vicinity of the sweet spot $\Phi_{ext}/\Phi_0 = 1/2$. A fit to the linear increase in $\Gamma^{\Phi}_{\varphi E}$ using Eq. (3.5) yields a flux noise amplitude of $\sqrt{A_\Phi} = 26\,\mu\Phi_0$. Note that each of the five consecutive flux sweeps was fitted with a model combining a flux-dependent Gaussian decay (accounting for 1/f flux noise) and a constant exponential decay component. Adapted from Ref. [3].

We attribute the exponential component of the dephasing rate to a combination of critical current noise in the nanojunction and superinductor (Γ_{I_c}), and photon shot noise from residual thermal photons in the readout resonator ($\Gamma_{\bar{n}}$)

$$\Gamma_{\text{exp}} = \frac{\Gamma_1}{2} + \Gamma_{I_c} + \Gamma_{\bar{n}}\,. \tag{5.4}$$

Here, the shot noise contribution $\Gamma_{\bar{n}}$ is governed by the interplay between the dispersive shift χ and the resonator linewidth κ, as described in Eq. (3.4) for the shot noise induced dephasing rate in the low photon limit.

To evaluate this contribution quantitatively, we measure the dressed resonator phase responses for the qubit in both the ground ($|g\rangle$) and excited ($|e\rangle$) states, using balanced IQ histograms as a function of the readout frequency at the half-flux sweet spot (see Fig. 5.9). Fits to these resonator responses yield a linewidth of $\kappa/2\pi = 1.00$ MHz and a dispersive shift of $\chi/2\pi = -1.72$ MHz corresponding to the frequency separation between the resonator when the qubit is in states $|g\rangle$ and $|e\rangle$, respectively. Based on these values and assuming that $\Gamma^{\text{const}}_{\varphi E}$ is dominated by the photon shot noise contribution, we estimate the residual thermal population of the resonator using Eq. (3.4). We extract a residual average photon number of $\bar{n} \approx 0.008$, corresponding to an effective resonator temperature of 74 mK. These values are consistent with literature (see e.g. Refs. [209, 217]), though notably about twice the effective qubit temperature inferred from the IQ clouds (cf. Fig. 5.12d). Such elevated resonator temperatures are commonly observed in superconducting qubit systems [217], attributed to the stronger coupling of the resonator to the transmission line, in contrast to the qubit, which couples only dispersively via the resonator and consequently experiences an additional dispersive isolation.

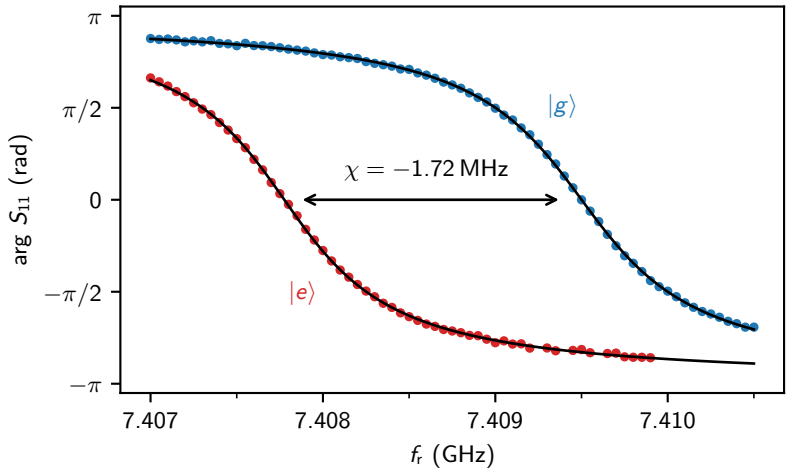

Figure 5.9: Dispersive readout of the gralmonium qubit at the half-flux sweet spot. Dressed resonator phase responses $\arg(S_{11})$ for the qubit in $|g\rangle$ (blue) and $|e\rangle$ (red). Data were acquired from IQ histograms (cf. Fig. 5.12) as a function of readout frequency f_r at half-flux bias $\Phi_{ext}/\Phi_0 = 1/2$. To balance the population of the qubit states, a $\pi/2$-pulse is applied prior to the readout pulse. Fits to the measured phase responses (black lines) yield a resonator linewidth of $\kappa/2\pi = 1.00$ MHz and a dispersive frequency shift of $\chi/2\pi = -1.72$ MHz between the $|g\rangle$ and $|e\rangle$ states. Adapted from Ref. [3].

Finally, we note that among the contributions in Eq. (5.4) only the critical current-induced dephasing Γ_{I_c} is effectively suppressed by the Hahn echo sequence. This likely accounts for the observed factor of three enhancement in T_{2E} compared to the Ramsey coherence time T_{2R}. Specifically, the echo sequence filters noise slower than 10^1 µs, corresponding to its filter function cutoff, while the single-point Ramsey measurement (i.e. 100 single-shot qubit measurements) can already capture noise on timescales slower than milliseconds.

5.4.2 Zero Flux Coherence

In Fig. 5.10, we present energy relaxation and coherence experiments at the zero-flux sweet spot, corresponding to a qubit frequency of $f_q = 10.8$ GHz. Surprisingly, the energy relaxation times are comparable to those obtained at half-flux bias, thereby excluding the possibility that a constant quality factor Q governs the T_1 limitation, $T_1 \neq Q/\omega_q$, as would be expected for example in the case of dielectric-loss-limited relaxation. In contrast, both Hahn echo and Ramsey coherence times are reduced by a factor of ~ 2 compared to those obtained at $\Phi_{ext}/\Phi_0 = 0.5$. Moreover, Ramsey measurements at zero flux do not exhibit the beating pattern, characteristic of the discrete qubit frequency switching observed at half flux. While the discrete critical current fluctuations remain present at $\Phi_{ext}/\Phi_0 = 0$ (see Fig. 5.5), the susceptibility of the qubit frequency to changes in E_J is significantly reduced at zero-flux bias compared to half-flux. This diminished sensitivity suppresses the observable beating frequency $f_{beating}$ in Ramsey fringes. Consequently, resolving such a suppressed beating pattern would require longer Ramsey coherence times. However, the experimentally observed reduction in T_{2R} further impedes any revival of the interference pattern, rendering it undetectable in our dataset. Finally, we note that at zero

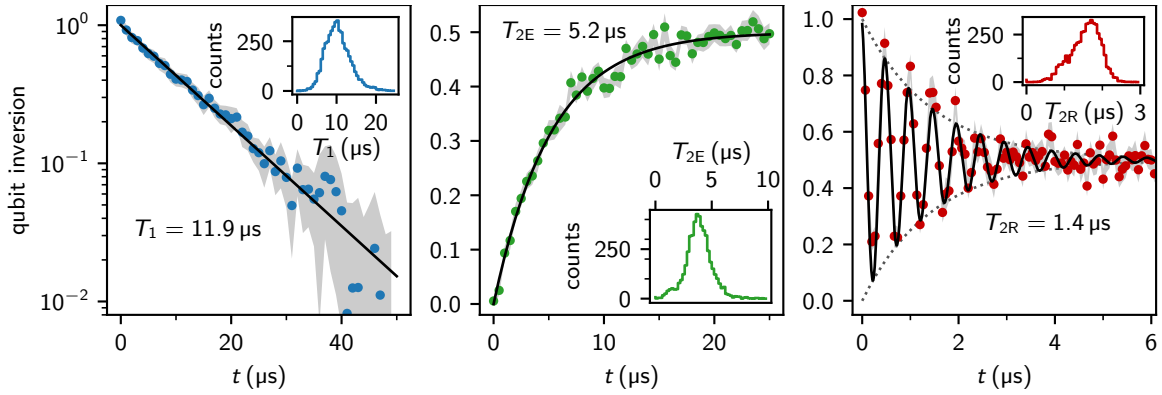

Figure 5.10: Energy relaxation and coherence of the gralmonium at zero-flux bias. **a** Free decay energy relaxation and **b** Hahn echo measurements with single exponential fits to the decay, yielding relaxation and echo coherence times of $T_1 = 11.9\,\mu s$ and $T_{2E} = 5.2\,\mu s$, respectively. **c** Ramsey fringes acquired at a nominal detuning of $f_{Ramsey} = 2\,MHz$. Unlike at the half-flux sweet spot, no beating pattern is observed, allowing a single-frequency fit that yields a Ramsey coherence time of $T_{2R} = 1.4\,\mu s$. **Insets:** Histograms of extracted relaxation and coherence times extracted from 5000 repetitions. While the average T_1 at zero flux is comparable to values measured at $\Phi_{ext}/\Phi_0 = 0.5$, both T_{2E} and T_{2R} are reduced by a factor of ~ 2. In all panels, markers represent the mean values across 20 repetitions, each comprising 100 single-shot qubit measurements per data point; shaded gray bands indicate the standard error of the mean. Adapted from Ref. [3].

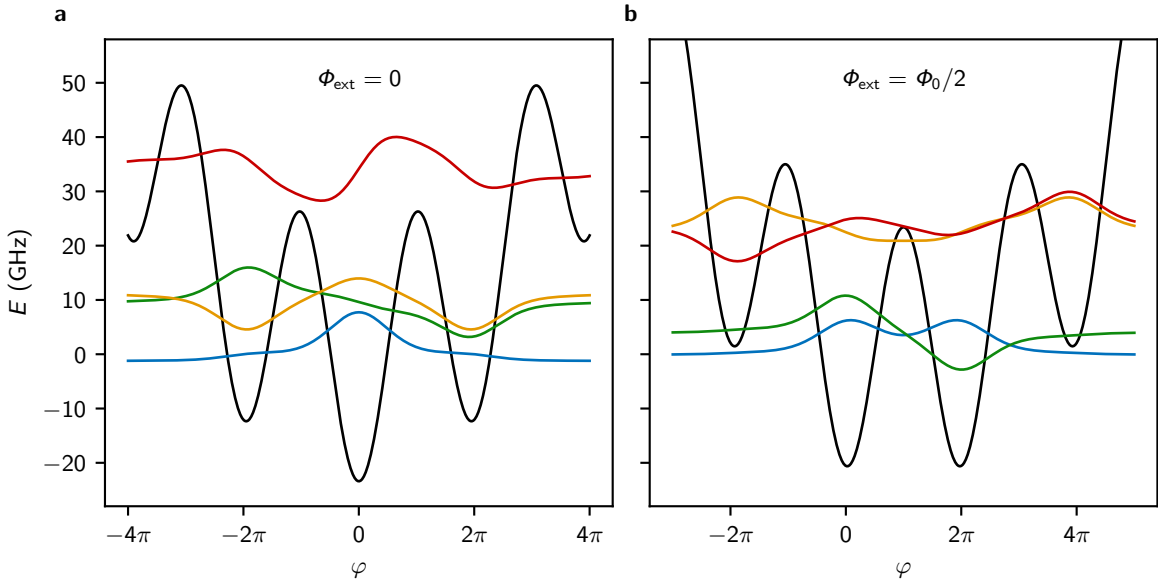

Figure 5.11: Gralmonium energy potential and wavefunctions at the flux sweet spots. Fluxonium potential energy landscape as a function of superconducting phase difference φ, shown at **a** zero flux bias ($\Phi_{ext}/\Phi_0 = 0$) and **b** half-flux bias ($\Phi_{ext}/\Phi_0 = 0.5$). The first four wavefunctions (shown in blue, green, ocher, and red) are overlaid on the potential and vertically offset by their respective eigenenergies. Device parameters are taken from the gralmonium characterized in Section 3.1: $E_L/h = 0.574\,GHz$, $E_J/h = 23.4\,GHz$ and $E_C/h = 15\,GHz$. **a** At $\Phi_{ext}/\Phi_0 = 0$, all wavefunctions are significantly delocalized over three wells of the potential, indicating that the $|g\rangle \rightarrow |e\rangle$ transition is not plasmon-like. **b** At $\Phi_{ext}/\Phi_0 = 0.5$, the wavefunctions of the $|g\rangle \rightarrow |e\rangle$ transition are determined by tunneling through the central cosinusoidal barrier at $\varphi = 0$, delocalized in the two adjacent potential wells. Adapted from Ref. [3].

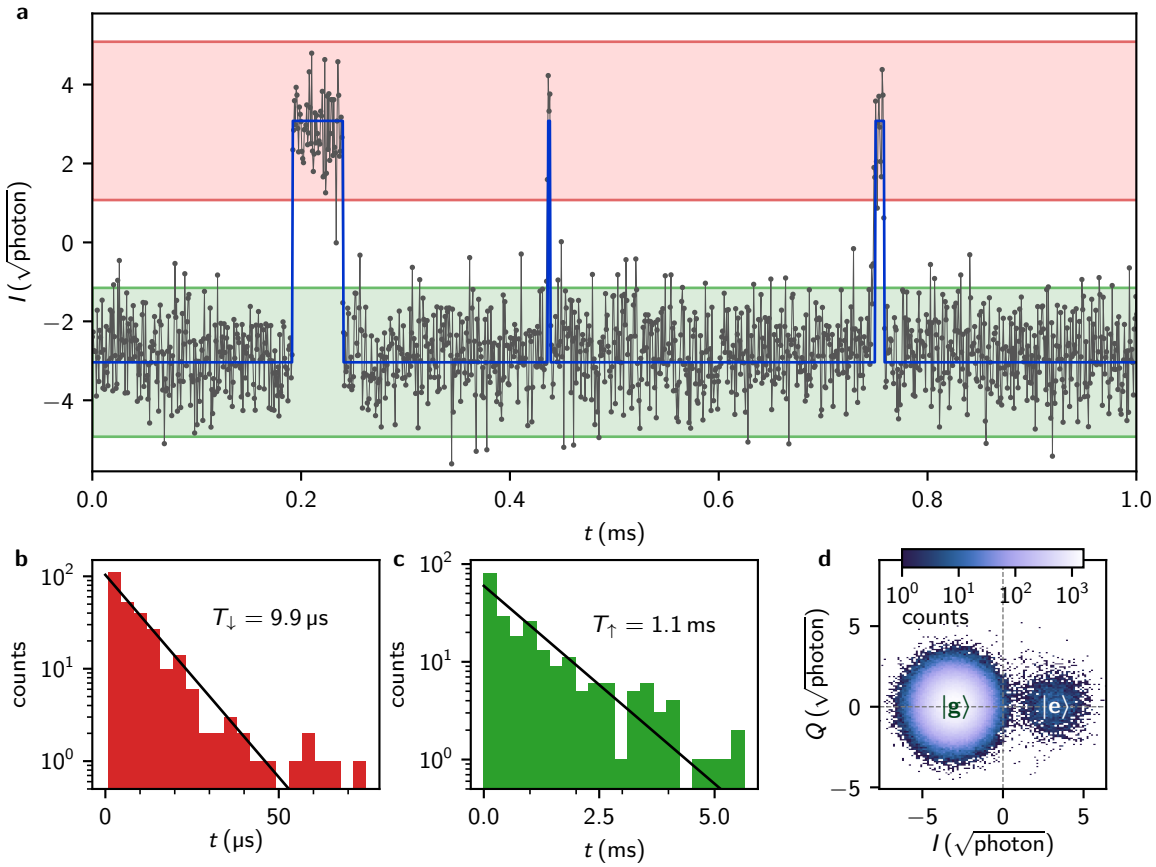

Figure 5.12: Quantum jump detection of the gralmonium at half-flux bias. **a** Example segment of the time trace of the resonator response, showing the in-phase component of the reflection coefficient $I = \mathrm{Re}(S_{11})$ (black connected markers). The qubit state (blue line) is assigned based on the $\pm 2\sigma$ bands (shaded area) around the mean response for the qubit for the ground (green) and excited (red) states. **b, c** Histograms of the qubit dwell times in the ground (**b**) and excited (**c**) states. Maximum likelihood exponential fits (black lines) yield qubit relaxation and excitation times $T_\downarrow = 9.9\,\mu s$ and $T_\uparrow = 1.1$ ms, respectively. **d** IQ histogram of the same dataset used in panels **a-c**, showing two clearly separated IQ clouds corresponding to the $|g\rangle$ and $|e\rangle$ states. Notably, the regime $|\chi| = 1.72\,\mathrm{MHz} > \kappa = 1.00\,\mathrm{MHz}$ (cf. Fig. 5.9) results in a 180° phase separation between the two states in the complex plane. For all measurements, we apply a continuous readout tone at a frequency of $f_r = 7.4086\,\mathrm{GHz}$ with a microwave power corresponding to $\bar{n} \approx 10$ circulating photons in the readout resonator. The resonator response is demodulated into contiguous segments of $\tau = 784\,\mathrm{ns}$ per data point over a total measurement time of 500 ms. Adapted from Ref. [3].

flux, the gralmonium qubit's wavefunctions are delocalized across three potential wells (cf. Fig. 5.11), indicating that the $|g\rangle \rightarrow |e\rangle$ transition is not plasmon-like in our device.

5.4.3 Quantum Jump Analysis

To characterize the relaxation dynamics of the gralmonium qubit under continuous readout, we present a quantum jump analysis in Fig. 5.12. The discrete quantum jumps between the qubit ground and excited states are illustrated in a representative 1 ms segment of the demodulated in-phase quadrature in Fig. 5.12a. For qubit state assignment, we implement

a two-point latching filter that declares a state transition whenever the I-quadrature value crosses into the $\mu \pm 2\sigma$ band associated with the opposite qubit state (shaded bands in Fig. 5.12a). From a double Gaussian fit to the marginal distribution along the I quadrature, we obtain the mean values $\mu_{\mathrm{g,e}} \approx \pm 3.0\,\sqrt{\mathrm{photon}}$ and standard deviations $\sigma_{\mathrm{g,e}} \approx 1.0\,\sqrt{\mathrm{photon}}$ for the qubit ground and excited states, respectively. Exponential fits to the dwell-time distributions in $|g\rangle$ and $|e\rangle$ (cf. Fig. 5.12b, c) reveal a relaxation time of $T_1 = (T_{\downarrow}^{-1} + T_{\uparrow}^{-1})^{-1} = 9.8\,\mu\mathrm{s}$, comparable to the free decay relaxation time in Fig. 3.4. This indicates a QND readout and a photon-number-independent energy relaxation.

In the IQ plane (Fig. 5.12d) the two qubit states form distinct Gaussian clouds, further supporting high-fidelity state discrimination. Note that we rotate the qubit state in the IQ plane to encode the state information into the in-phase quadrature I in all measurements. From the steady-state populations, we extract an effective qubit temperature of 37 mK, consistent with values in the literature [7, 9, 103, 217].

6 Characterization of the Gralmonium Qubit in High Magnetic Fields

In this chapter, we present an extended characterization of the gradiometric gralmonium qubit under applied magnetic fields. We first compare the flux periodicities of gradiometric and non-gradiometric devices to evaluate the role of inductance asymmetries in future qubit design iterations. Next, we assess the magnetic-field dependence of qubit coherence across multiple half-flux qubit frequencies obtained in successive cooldowns, confirming the robust performance of the gradiometric architecture up to 1.2 T. We further analyze the suppression of fast flux noise at high magnetic fields, corroborating its consistency across varying qubit frequencies. We highlight the characteristic Gaussian decay observed in Hahn echo measurements and provide a detailed derivation of the two-level fluctuator model introduced in Section 3.3.1, which captures the measured field dependence of the flux noise amplitude across qubit frequencies. Finally, we examine the influence of magnetic field on the readout process, identifying elevated qubit temperatures as a result of thermal photon leakage and highlighting the importance of shielding in future implementations. This chapter is adapted in parts from Ref. [1].

6.1 Flux Periodicity Reduction in the Gradiometric Gralmonium

In Section 3.2, we introduced the gradiometric qubit design to mitigate susceptibility of flux-tunable gralmonium qubits to global flux noise in large magnetic fields. Due to uncertainties in the resulting inductive asymmetry (cf. Eq. (3.2)), arising from distributed capacitance and inductance in our design as well as charging effects in the meander structures that reduce the effective qubit inductance (see Section 3.1), we conservatively implemented a 10% mismatch in the enclosed flux loop area, rather than aiming for a more flux-insensitive design. To quantify the impact of these effects, we analyze the inductive asymmetry $\alpha = \frac{L_{1,s}-L_3}{L_{1,s}+L_3}$ in the following. Understanding the variability of α is particularly relevant for the design of future devices with increased flux insensitivity, in order to mitigate the limitations imposed by low-frequency flux noise on two-tone spectroscopy (cf. Fig. 3.6) and Ramsey coherence times (cf. Fig. 3.8). To this end, we fabricated both a gradiometric fluxonium qubit (as shown in Fig. 3.5) and a non-gradiometric variant with nearly identical layout. The latter omits the connecting wire that closes the second flux

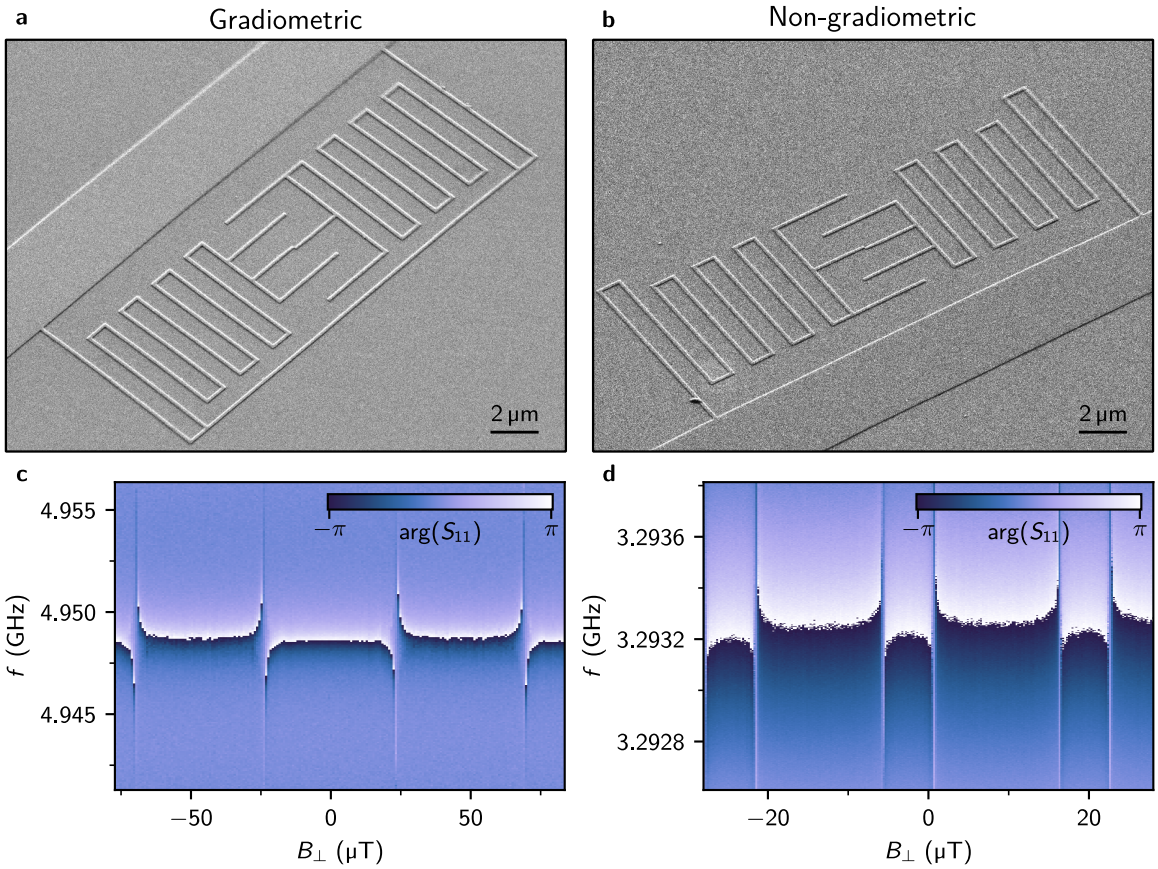

Figure 6.1: Flux periodicity in gradiometric and non-gradiometric gralmonium qubits. **a**,**b** SEM images of **a** a gradiometric and **b** a non-gradiometric qubit circuit. The non-gradiometric design omits the outer inductor closing the outer flux loop in the gradiometric design. **c**,**d** Flux dependence of the readout resonator phase response $\arg(S_{11})$, for the **c** gradiometric and **d** non-gradiometric gralmonium qubit, measured as a function of perpendicular magnetic field $B_\perp$. The gradiometric design exhibits a flux period reduced by a factor of 4.6 compared to the non-gradiometric design. Adapted from Ref. [1].

loop in the gradiometric design. We present SEM images of both implementations in Fig. 6.1a, b.

The flux sweeps of the two designs, shown in Fig. 6.1c, d, reveal flux periods of $B_{\Phi_0} = 93\,\mu\text{T}$ and $B_{\Phi_0} = 22\,\mu\text{T}$ for the gradiometric and non-gradiometric design, respectively. This corresponds to $\Phi_1/\Phi_{\text{ext}} = 4.25$, slightly below the expected value of $\Phi_1/\Phi_\Delta = 4.6$ based on the designed loop areas. From this, we infer an effective area of $A_{\text{eff}} = 34\,\mu\text{m}^2$ for the gradiometric device and an inductive asymmetry of $\alpha = -2.3\,\%$. While this value contrasts with the nominally positive design asymmetry ($L_1 \approx 1.09 \cdot L_3$, $\alpha_{\text{design}} = +4\,\%$), it confirms the aforementioned uncertainty in inductive asymmetry. At the same time, the small magnitude of α justifies the approximation of negligible inductive asymmetry $\alpha \approx 0$ throughout the manuscript.

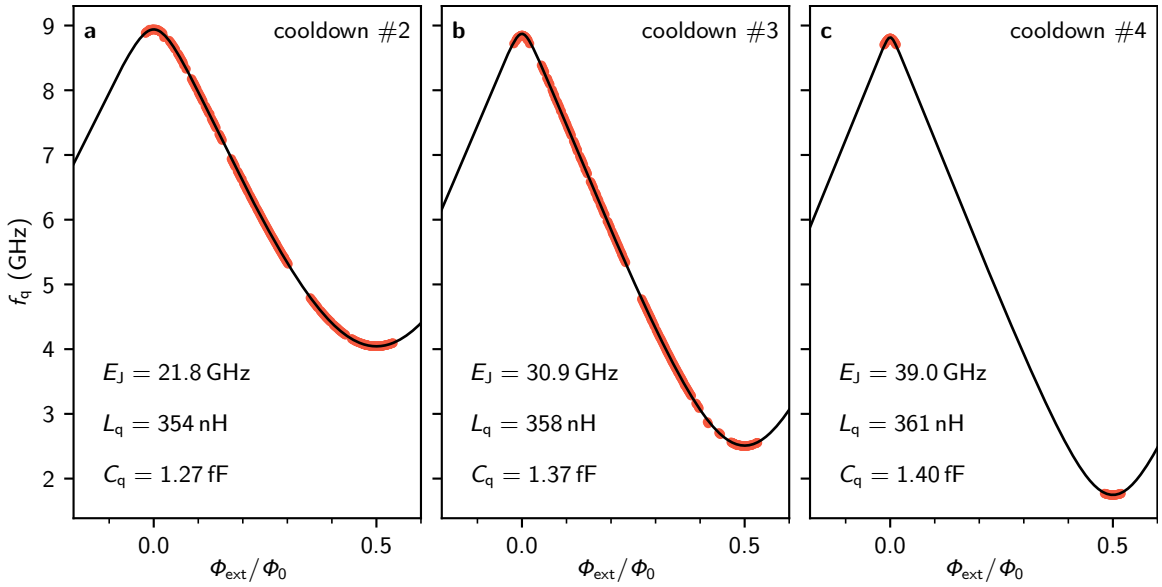

Figure 6.2: Gradiometric gralmonium spectroscopy across successive cooldowns. Extracted $|g\rangle \rightarrow |e\rangle$ transition frequencies of the same device measured over consecutive cooldowns. Black lines represent fits to the fluxonium Hamiltonian H_{flux} (Eq. (1.7)). The spectra correspond to half-flux qubit frequencies of **a** $f_q = 4$ GHz, **b** $f_q = 2.5$ GHz and **c** $f_q = 1.8$ GHz, as referenced in Fig. 6.3 and Fig. 6.5.

6.2 Qubit Characterization in Magnetic Field at Different Qubit Frequencies

Fluctuations in the nanojunction energy, as discussed in Section 5.3, enable magnetic-field characterization of the same gradiometric gralmonium device introduced in Section 3.2 at different half-flux qubit frequencies across multiple cooldowns. Figure 6.2 presents the qubit spectroscopy of the gradiometric gralmonium across three consecutive cooldowns (cooldown #1 is shown in Fig. 3.6), corresponding to qubit frequencies at the half-flux sweet spot of $f_q = 4$ GHz, $f_q = 2.5$ GHz and $f_q = 1.8$ GHz, respectively. We characterize the energy relaxation and coherence at these qubit frequencies as a function of magnetic field in Fig. 6.3. Both the energy relaxation time T_1 and the Hahn echo coherence time T_{2E} remain robust up to magnetic fields of 1.2 T, confirming the results in Section 3.2.2. Note that in our analysis, we focus on the Hahn echo coherence time T_{2E}, rather than Ramsey decay times, as T_{2E} can be reliably extracted even when the Ramsey beating frequency f_{beating} is not resolvable due to variations in f_{beating} competing with the decay envelope.

Across all cooldowns and qubit frequencies, we observe clear signatures of electron spin resonance (ESR) coupling to $g = 2$, spin-$s = 1/2$ paramagnetic impurities. These appear as sharp reductions in T_1 when the qubit frequency becomes resonant with the ESR condition. As expected, the resonance field B_{ESR} increases with qubit frequency, in agreement with the linear ESR dispersion. Furthermore, we observe a systematic reduction in T_1 with increasing qubit frequency, consistent with a frequency-dependent loss mechanism, such as dielectric loss in the qubit capacitor.

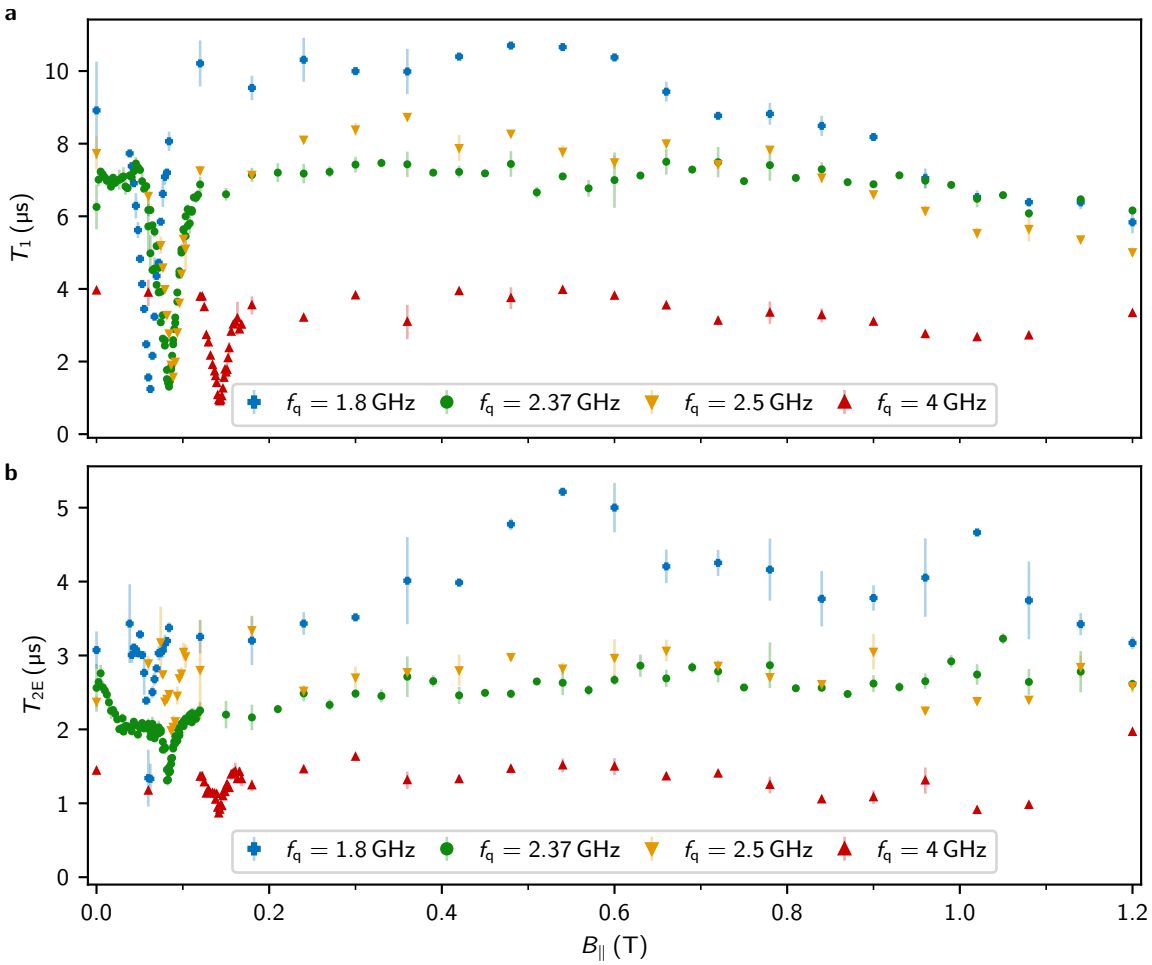

Figure 6.3: Energy relaxation and coherence in magnetic field across qubit frequencies. **a** Qubit energy relaxation time T_1 and **b** Hahn echo coherence time T_{2E} as a function of magnetic field $B_\parallel$. Markers represent measurements at different qubit frequencies at the half-flux sweet spot, using the same device across successive cooldowns (Fig. 6.2). Both T_1 and T_{2E} remain robust under magnetic field across different qubit frequencies. Notably, pronounced decreases in T_1 are observed when f_q becomes resonant with the electron spin resonance (ESR) of spurious $g = 2$ spin-$s = 1/2$ paramagnetic impurities. As expected, the magnetic field B_{ESR} of the ESR signature increases with f_q, consistent with Fig. 3.9.

6.3 Flux Noise in Magnetic Field

In Section 3.3.1, we demonstrated the suppression of fast flux noise in magnetic field. Here, we extend this analysis by incorporating additional data from multiple qubit frequencies measured across successive cooldowns, and we provide a theoretical derivation of the magnetic field dependence of the extracted flux noise amplitudes.

For Gaussian-distributed noise (see Ref. [195]), the dephasing contribution to the Hahn echo decay is governed by [195]

$$f_{\varphi E}(t) = \exp\left(-\frac{t^2}{2}\left|\frac{\partial\omega}{\partial\Phi_{ext}}\right|^2 \int_{-\infty}^{\infty}\frac{d\omega}{2\pi}S(\omega)\frac{\sin^4(\omega t/4)}{(\omega t/4)^2}\right), \tag{6.1}$$

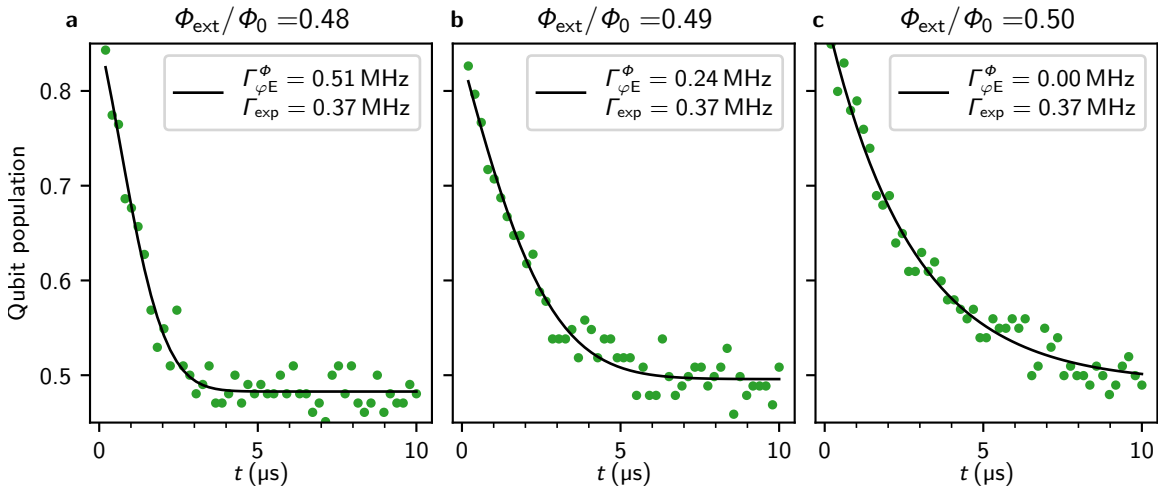

Figure 6.4: Flux-dependence of the Hahn echo decay. Time evolution of the qubit excited-state population during Hahn echo experiments, with a single refocusing π-pulse applied at $t/2$. Black lines represent a joint fit of 42 individual echo measurements acquired over the flux range $\Phi_{ext} = 0.48–0.52\,\Phi_0$, using Eq. (5.3), with a constant exponential decay rate Γ_{exp} and a flux-dependent Gaussian dephasing contribution $\Gamma^{\Phi}_{\varphi E}$. To improve the visibility of the echo signal, state initialization into the ground state $|g\rangle$ is employed, compensating for reduced readout contrast due to high thermal qubit population of $p_{th} \gtrsim 35\,\%$.

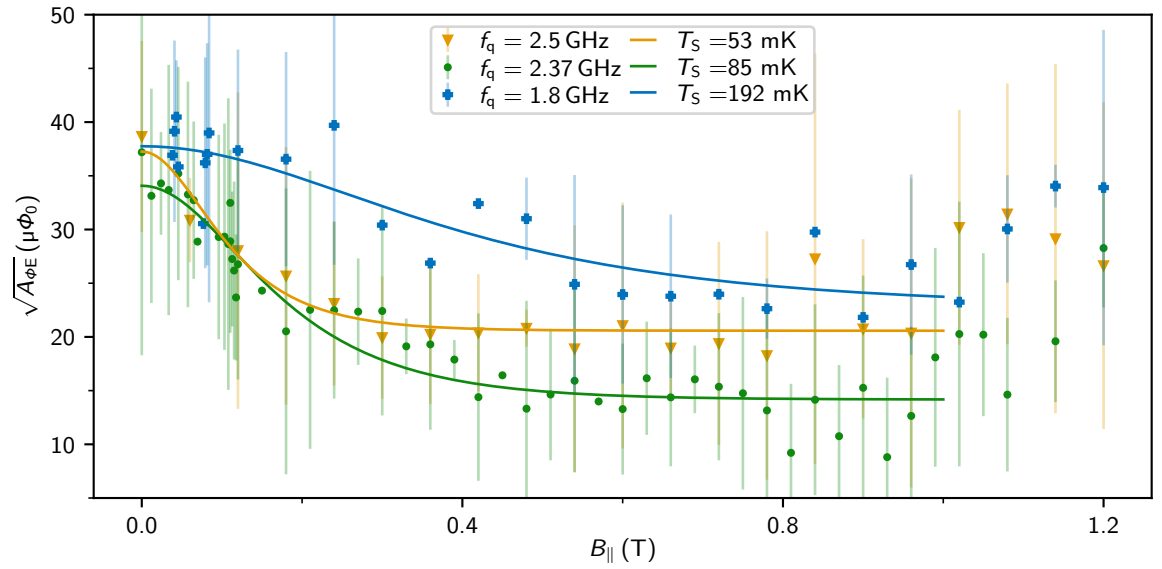

Figure 6.5: Suppression of fast flux noise in magnetic field across different qubit frequencies. Flux noise amplitude $\sqrt{A_\Phi}$, extracted from flux-dependent Hahn echo measurements (cf. Eq. (3.5)), as a function of magnetic field. Colors and marker shapes represent different qubit frequencies at the half-flux sweet spot, measured across successive cooldowns of the same device (cf. Fig. 6.2). Solid lines represent fits to the magnetic-field dependence of $\sqrt{A_\Phi}$ using Eq. (6.12), consistent with magnetic freezing of fast flux noise due to spin polarization. We extract spin temperatures of $T_S = 53$ mK, $T_S = 85$ mK and $T_S = 192$ mK. Adapted from Ref. [1].

where $S(\omega)$ denotes the noise power spectral density. For a constant (white) noise spectrum $S_\Phi(\omega) = A$, the integral evaluates to a single exponential decay:

$$f_{\varphi\mathrm{E}}(t) = \exp\left(-t\left|\frac{\partial\omega}{\partial\Phi_{\mathrm{ext}}}\right|^2 \frac{A}{2}\right). \tag{6.2}$$

In contrast, assuming a $1/\omega$ flux noise power spectrum, $S_\Phi(\omega) = 2\pi A_\Phi/\omega$, the integration in Eq. (6.1) yields

$$f_{\varphi\mathrm{E}}(t) = \exp\left(-t^2\left|\frac{\partial\omega}{\partial\Phi_{\mathrm{ext}}}\right|^2 A_\Phi \ln 2\right), \tag{6.3}$$

corresponding to a Gaussian decay envelope characterized by the flux-noise-induced dephasing rate $\Gamma^{\Phi}_{\varphi\mathrm{E}}$, as introduced in Eq. (3.5).

Indeed, this Gaussian decay characteristic is confirmed in the Hahn echo decay curves shown in Fig. 6.4. Away from the sweet spot (Fig. 6.4a), the echo signal displays clear non-exponential decay, whereas near $\Phi_{\mathrm{ext}}/\Phi_0 = 1/2$, the decay transitions to a purely exponential form (cf. Fig. 6.4b, c). The linear dependence of the dephasing rate on $|\partial\omega/\partial\Phi_{\mathrm{ext}}|$ (Fig. 3.11a) further supports a $1/\omega$ noise spectrum, as opposed to the quadratic dependence expected for white noise with an exponential decay, i.e. $\Gamma_{\varphi\mathrm{E}} \propto |\partial\omega/\partial\Phi_{\mathrm{ext}}|^2$ (cf. Eq. (6.2)).

In Fig. 6.5, we present the magnetic field dependence of the flux noise amplitude $\sqrt{A_\Phi}$, for three qubit frequencies extracted from successive cooldowns (cf. Fig. 6.2). These amplitudes were obtained by fitting the flux-dependent dephasing rates $\Gamma^{\Phi}_{\varphi\mathrm{E}}$ to Eq. (3.5), as shown in Fig. 3.11a. Across all qubit frequencies, we observe a clear suppression of the flux noise amplitude with increasing magnetic field, consistent with the trends previously reported in Section 3.3.1. Notably, we also observe the onset of an additional flux noise mechanism in magnetic fields $B_\parallel \gtrsim 1\,\mathrm{T}$ consistently across qubit frequencies.

To model the magnetic field dependence of the flux noise amplitude, we consider a bath of magnetic two-level fluctuators (TLFs), such as non-interacting localized spins. At the experimentally probed magnetic fields $B_\parallel \sim 1\,\mathrm{T}$, the high-temperature approximation $k_\mathrm{B}T \gg \mu_\mathrm{B}B$, which implies the simplification of equal excitation and relaxation rates $\Gamma_\uparrow = \Gamma_\downarrow$, no longer holds. Therefore, we model each TLF as a source of an asymmetric random telegraph signal, resulting in a Lorentzian power spectrum of the form:

$$S(\omega) \propto \frac{1}{\Gamma_1/\Gamma_\uparrow + \Gamma_1/\Gamma_\downarrow}\frac{\Gamma_1}{\Gamma_1^2 + \omega^2}, \tag{6.4}$$

where $\Gamma_1 = \Gamma_\uparrow + \Gamma_\downarrow$ denotes the total transition rate, and $\Gamma_\uparrow$, $\Gamma_\downarrow$ are the excitation and relaxation rates, respectively [210].

To extract the magnetic field dependence of the noise amplitude $A_\Phi \propto (\Gamma_1/\Gamma_\uparrow + \Gamma_1/\Gamma_\downarrow)^{-1}$, we assume Γ_1 is field-independent and apply the principle of detailed balance for the population probabilities p_0 and p_1 of the ground and excited state

$$\dot{p_0} = \Gamma_\downarrow p_1 - \Gamma_\uparrow p_0\,, \qquad \dot{p_1} = \Gamma_\uparrow p_0 - \Gamma_\downarrow p_1\,.$$

At thermal equilibrium, $\dot{p_0} = \dot{p_1} = 0$, we obtain

$$\Gamma_\uparrow = \Gamma_1 p_{\mathrm{th}} \tag{6.5}$$
$$\Gamma_\downarrow = \Gamma_1 (1 - p_{\mathrm{th}}) , \tag{6.6}$$

where $p_{\mathrm{th}} = p_1(\dot{p_1} = 0)$ denotes the excited state population probability in thermal equilibrium.

For Boltzmann-distributed populations

$$\frac{p_1}{p_0} = \frac{p_{\mathrm{th}}}{1 - p_{\mathrm{th}}} = e^{\frac{-\Delta E}{k_{\mathrm{B}} T}} , \tag{6.7}$$

with the energy difference ΔE between the ground and excited state, the flux noise power becomes

$$1/A_\Phi \propto \frac{\Gamma_1}{\Gamma_\uparrow} + \frac{\Gamma_1}{\Gamma_\downarrow} \tag{6.8}$$
$$= \frac{1}{p_{\mathrm{th}}} + \frac{1}{(1 - p_{\mathrm{th}})} \tag{6.9}$$
$$= \left(e^{\frac{-\Delta E}{k_{\mathrm{B}} T}} + 1\right)\left(e^{\frac{\Delta E}{k_{\mathrm{B}} T}} + 1\right) \tag{6.10}$$
$$= 4 \cosh^2\left(\frac{\Delta E}{2 k_{\mathrm{B}} T}\right) . \tag{6.11}$$

Assuming the bath of magnetic TLFs consists of $g = 2$ spin-$s = 1/2$ paramagnetic impurities, consistent with ESR signatures observed in qubit energy relaxation (cf. Section 3.3.1), the energy splitting is $\Delta E = 2\mu_{\mathrm{B}} B$. The magnetic field dependence of the flux noise amplitude is thus:

$$\sqrt{A_\Phi} \propto \frac{1}{\cosh\left(\frac{\mu_{\mathrm{B}} B}{k_{\mathrm{B}} T}\right)} . \tag{6.12}$$

Fits to Eq. (6.12) accurately reproduce the measured field-dependent flux noise amplitudes shown in Fig. 6.5. Nevertheless, the persistence of residual flux noise at high field indicates the presence of additional decoherence mechanisms. This suggests further measurements, including spectral analysis of the magnetic-field-dependent noise.

6.4 Qubit Readout in Magnetic Field

In this section, we examine the influence of an in-plane magnetic field on the fidelity and stability of the qubit readout process. Figure 6.6 shows histograms of single-shot qubit measurements in $B_\parallel = 0\,\mathrm{T}$ and $B_\parallel = 1.2\,\mathrm{T}$ at the half-flux sweet spot. To quantify the readout performance, we extract the signal-to-noise ratio (SNR) from double-Gaussian fits to the marginal distribution along the in-phase quadrature (lower panels in Fig. 6.6). We

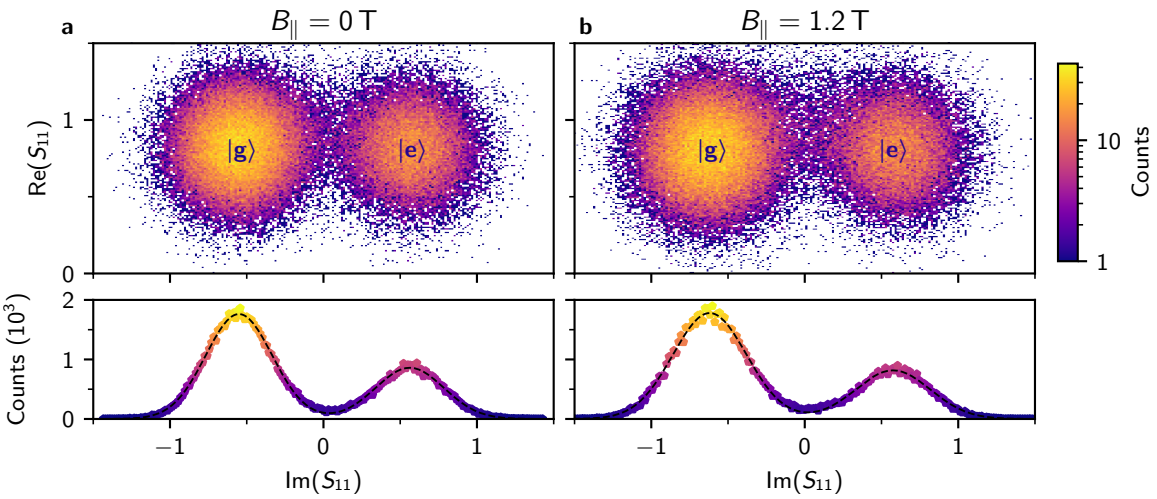

Figure 6.6: Comparison of qubit IQ histograms in magnetic field. Histograms of single-shot qubit measurements at the half-flux sweet spot for **a** $B_{\parallel} = 0\,\mathrm{T}$ and **b** $B_{\parallel} = 1.2\,\mathrm{T}$ Top panels show 2D histograms of the resonator response in the complex plane corresponding to effective qubit temperatures of 165 mK and 150 mK, respectively. Bottom panels show the corresponding marginal distributions along the $I = \mathrm{Re}(S_{11})$ quadrature with associated double-Gaussian fits. The regime $\chi/2\pi = 0.5\,\mathrm{MHz} < \kappa/2\pi = 1.2\,\mathrm{MHz}$ results in a phase separation $\varphi < 180°$ between the qubit states. Measurements were performed using a 540 ns readout pulse at a power corresponding to a steady-state average photon number of $\bar{n} = 25$. The demodulated signal, integrated over $\tau = 540\,\mathrm{ns}$, includes resonator ring-up and ring-down dynamics. Consequently, data are normalized to the amplitude of the reflection coefficient for the ground state, $|S_{11}(|g\rangle)|$. Adapted from Ref. [1].

define the SNR as the distance between $|g\rangle$ and $|e\rangle$ states in the complex plane relative to their combined standard deviation, which maps to the respective marginal distribution in the in-phase quadrature, encoded into the mean values μ and standard deviations σ from the double Gaussian fits:

$$SNR = \frac{|\mu_{|g\rangle} - \mu_{|e\rangle}|}{\sigma_{|g\rangle} + \sigma_{|e\rangle}} = 2.5\,.$$

Using an automated tune-up of the parametric amplifier, we maintain a constant SNR throughout experiments conducted in high magnetic fields.

From the steady-state populations of the $|g\rangle$ and $|e\rangle$ state, we infer an effective qubit temperature of $T_{\mathrm{q}} = 165\,\mathrm{mK}$ in zero field, corresponding to a thermal population of $p_{\mathrm{th}} = 34\,\%$. This elevated thermal population is attributed to the absence of additional thermal shielding around the sample holder (cf. Fig. B.1), allowing thermal photons to infiltrate the chip environment. Since a cryogenic infrared filter is installed directly in front of the sample holder to suppress photon inflow via the microwave lines, the dominant contribution is identified as direct infrared photon infiltration bypassing the copper dowel of the sample holder (cf. Fig. B.1). This conclusion is supported by the similarity between the extracted qubit temperature and the readout resonator temperature of $T_{\mathrm{r}} = 150\,\mathrm{mK}$, inferred from photon-shot-noise-limited dephasing at the sweet spot. This contrasts with the results reported in Section 5.4.1, where a qubit temperature approximately half that of the resonator was attributed to indirect coupling of the qubit to the transmission line via

the resonator, providing additional isolation from thermal photons in the transmission line. Such qubit-resonator temperature differences are consistent with previous observations in superconducting qubit systems [217]. The absence of such a temperature difference in the present setup suggests that the dominant source of residual qubit excitation is not the transmission line but rather a higher ambient photon population within the sample enclosure.

To mitigate the reduction in readout contrast resulting from high thermal population, we perform state initialization into $|g\rangle$ prior to all time-domain measurements, including the Hahn echo experiments illustrated in Fig. 6.4.

Part III

Conclusion and Future Directions

Conclusion and Future Directions

This work aimed to realize a magnetic-field-resilient platform for longitudinal coupling between individual spins and superconducting circuits. Towards this goal, the first result was the demonstration of a longitudinal interaction between a granular aluminum (grAl) resonator and a molecular spin ensemble, mediated by the superconductor's kinetic inductance. To extend this coupling mechanism to the nanoscopic scale required for single-spin detection, we developed a novel circuit element, which concentrates kinetic inductance within a nanoscopically confined grAl volume: the grAl nanojunction. Integrated into a fluxonium superconducting qubit fabricated entirely from a single grAl layer, the resulting gralmonium qubit retains a characteristic fluxonium spectrum and enables coherent qubit operation. We further demonstrated magnetic field resilience of the gralmonium and detected signatures of spin ensembles located in the qubit environment. Finally, numerical simulations confirmed the gralmonium's sensitivity to individual spins. In the following, we summarize the key achievements and outline future directions for achieving single-spin detection with this architecture.

Longitudinal Spin–Resonator Coupling

The first key result of this work was the realization of longitudinal coupling between a molecular spin ensemble and a grAl resonator. The interaction is mediated by persistent currents induced in grAl by the ensemble magnetization, which in turn modulates the kinetic inductance via the intrinsic grAl nonlinearity. This effect enables the measurement of the ensemble magnetization independent of spin-resonator detuning, yielding a full paramagnetic magnetization curve up to 1 T. Such measurements provide direct access to the spin temperature and offer a route towards characterizing the Zeeman energy spectrum of spin ensembles, akin to techniques based on DC SQUIDs [159].

To probe spin dynamics, we performed TT-ESR spectroscopy using on-chip, fixed-frequency niobium drive resonators operating far detuned from the readout. Transitioning to a frequency-continuous drive line would enable full mapping of the Zeeman diagram for ESR-active transitions. Furthermore, time-resolved excitation and relaxation measurements revealed a non-exponential spin relaxation, limited by phonon decay into the substrate (phonon bottleneck). When mitigating this limitation, e.g. by using diluted molecular crystals with smaller spin concentration and smaller overall sample size, the longitudinal spin coupling allows to infer the energy relaxation time T_1 without being constrained by Purcell decay or suppressed readout signal at large detunings.

Beyond this initial proof-of-concept, spin sensitivity could be further enhanced using a loop geometry similar to the implementations of kinetic inductance magnetometers [161–163]. Moreover, this interaction mechanism is not limited to grAl but can be readily implemented in microwave devices utilizing other magnetic field resilient high-kinetic-inductance superconductors such as NbN [131–133], NbTiN [134–136], InOx [137, 138]. While the present work establishes a microwave-domain, non-demolishing spin readout strategy, the ensemble-based approach remains subject to limitations, such as inhomogeneous broadening and the phonon relaxation bottleneck. Overcoming these challenges necessitates to extend this coupling scheme towards individual spin detection.

The Gralmonium Qubit

To tailor the kinetic-inductance-mediated interaction to the highly localized dipole field of a single spin, we developed a novel superconducting circuit element by confining the grAl wire within a $(20\,\mathrm{nm})^3$-volume, which we denote grAl nanojunction. Integrated into a fluxonium qubit architecture in a single grAl layer, this forms the gralmonium qubit. Employing the fluxonium energy spectrum as a sensitive probe, we confirmed a spectrum consistent with conventional fluxonium devices exhibiting a sinusoidal current-phase relation, with an upper bound of 5 % on higher Josephson harmonics. A remarkable consequence of these results is that the grAl nanojunction can be understood as a single effective Josephson junction operating in a novel mesoscopic regime. In this configuration, transport is mediated neither by tunneling between macroscopic electrodes (i.e. a conventional SIS JJ) nor by tunneling via an individual grain, but via collective inter-grain Josephson coupling across a 3D aluminum grain network.

The gralmonium demonstrated energy relaxation and coherence times on the order of 10 µs, comparable to coherence times of many SIS-JJ-based qubits, though two orders of magnitude below the current state-of-the-art. Notably, this performance surpasses that of typical constriction based devices made from disordered superconductors [131–133, 137, 186] or gate-tunable weak links [125, 178–183]. This highlights the grAl nanojunction's unique combination of the coherence of standard $\mathrm{Al/AlO}_x\mathrm{/Al}$ junctions with the field resilience of disordered superconductors and the nanoscopic footprint of ScS weak links. These coherence metrics not only serve as figures of merit for quantum information processing but also quantify the qubit frequency resolution critical to the longitudinal spin detection scheme. On timescales ranging from milliseconds to days, the nanojunction exhibits discrete critical current fluctuations manifesting as toggling between two distinct qubit transition frequencies. This further illustrates the mesoscopic junction size, observing a transition where discrete random-telegraph-switching replaces the smooth $1/f$ ensemble average seen in large $\mathrm{Al/AlO}_x\mathrm{/Al}$ junctions. Importantly, the observed frequency toggling reflects the qubit's exponential sensitivity to Josephson energy E_J — the same mechanism that enables single-spin state encoding — but concurrently limits Ramsey coherence.

Candidate mechanisms for the fluctuations include structural defects modulating the tunnel transparency and charge fluctuations coupling to the superconducting phase via the Aharonov-Casher effect. Experiments to discriminate between these effects involve

implementing a local electric field bias with a gate electrode or applying mechanical stress [35, 144]. Potential strategies to reduce the nanojunction fluctuations involve cold substrate deposition, which has been shown to yield smaller and more uniform grains [140, 203], or post processing such as hydrogen surface passivation [218] and laser annealing [219]. Beyond grAl, the chemical and structural similarity between the grAl microstructure and conventional Al/AlO_x/Al junctions suggests that insights gained from reducing fluctuations in nanojunctions may directly inform broader superconducting qubit technologies. In this context, grAl nanojunction fluctuations provide a direct metric of improvement for evaluating new fabrication strategies aimed at minimizing critical current noise. The fact that any reduction in junction fluctuations will directly enhance the resolution of single-spin detection highlights the importance of fabrication control and material engineering for future implementations of hybrid spin-superconductor quantum architectures.

A Superconducting Qubit Resilient to High Magnetic Fields

Integrating the gralmonium qubit into hybrid quantum architectures for single-spin readout requires robust operation in high magnetic fields to enable spin qubit operation. To minimize the impact of global flux noise on qubit performance, we implemented a gradiometric qubit design. We confirmed spectral stability of the gralmonium in magnetic fields up to 1.2 T, with fluxonium parameters showing only a small shift attributed to a mere percent suppression of the superconducting gap $\Delta(B_{\parallel})$. Notably, the critical magnetic field and coherence length of the grAl nanojunction, $B_c = 6.8\,\mathrm{T}$ and $\xi = 7\,\mathrm{nm}$, exceed those of the grAl superinductor and stripline resonator ($B_c = 4.9\,\mathrm{T}$ and $\xi = 8.2\,\mathrm{nm}$). This difference reflects the nanojunction's reduced dimensions and is not yet fully understood, motivating further theoretical modeling. It may arise from spatial confinement of Cooper pairs or locally increased oxidation. Since the modeling of the disorder-driven enhancement in T_c and B_c in granular aluminum remains unsettled, our measurements provide a unique data point that hints at localization as the underlying cause, rather than an intrinsic material property.

Remarkably, energy relaxation and coherence remain robust in magnetic fields up to 1.2 T. However, increased low-frequency flux noise in magnetic field results in a moderate reduction in Ramsey coherence time. This limitation can be addressed in future designs by increasing the symmetry in the gradiometric fluxonium layout to further suppress sensitivity to global flux noise. Additionally, improved frequency resolution for single-spin readout can be achieved by minimizing dielectric losses in the interdigitated capacitor and introducing infrared shielding around the sample holder to mitigate photon shot noise.

Beyond its role in hybrid quantum systems, the gralmonium's field resilience and spectral stability make it a powerful platform for probing magnetic field susceptibilities of various degrees of freedom coupled to superconducting circuits. We experimentally rule out paramagnetic defects at the origin of the discrete critical current fluctuations, as these remained unchanged in magnetic fields up to 1 T. Furthermore, we detect ESR signatures of spurious $g = 2$ spin $s = 1/2$ paramagnetic impurities coupling transversely to the

qubit, observed for the first time with a superconducting qubit. Such spin signatures are commonly attributed to unpaired electrons localized in disordered aluminum oxide, adsorbed oxygen radicals, or dangling bonds at the sapphire-metal interface [28, 91, 207]. We also confirm the long-standing hypothesis of the freeze-out of fast flux noise in high magnetic fields: Hahn echo experiments reveal a suppression of the $1/f$ flux noise amplitude, accurately captured by a model of asymmetric random telegraph fluctuators and consistent with a $g = 2$, spin $s = 1/2$ paramagnetic origin. The intriguing correlation between the ESR signatures in the qubit energy relaxation and the suppression of fast flux noise suggests a common paramagnetic origin. Validating this link through detailed spectral analyses of the flux noise evolution in magnetic fields will provide critical insights into its microscopic mechanisms. Finally, operation of the gralmonium in magnetic field allowed us to exclude the electron-spin hypothesis for the long-lived two-level system environment responsible for non-Markovian qubit dynamics [7].

Perspective on single-spin sensing

To extend the longitudinal coupling scheme towards single-spin detection, we propose to place a single spin atop a grAl nanojunction. The spin state modulates the Josephson energy E_J by locally suppressing the superconducting gap, thereby shifting the qubit frequency. Numerical simulations confirm that this configuration enables spin-induced qubit frequency shifts on the order of several kHz — a resolution routinely achieved with superconducting qubits [101, 213, 214] and potentially enhanced by advanced frequency-tracking protocols from quantum sensing [215, 216]. Further improvements can be achieved by repeated fast measurements, facilitated by the short readout time enabled by photon-number-independent readout [103]. Moreover, order of magnitude stronger interaction could be possible by miniaturizing the nanojunction by a factor of two and embedding the magnetic molecule in its center. As a result, this architecture paves the way towards single-shot, quantum non-demolition readout of individual spins.

Part IV

Appendix

A Fabrication details

A.1 GrAl Resonator Fabrication

The grAl resonators discussed in Chapter 2 and Chapter 4, are fabricated on c-plane sapphire substrates using a two-step optical lithography process to define both grAl and niobium resonators on the same chip. Each step involves patterning AZ5214E photoresist via optical lithography and development in AZ developer. Prior to metal deposition, an Ar/O_2 plasma clean is performed using a Kaufman ion source within a Plassys MEB 550S shadow evaporation system, followed by a titanium gettering step to reduce chamber pressure to $p \sim 10^{-7}$ mbar. A 20 nm thick grAl film is then deposited at 1 nm/s in a dynamic oxygen environment, yielding a sheet resistance of $R_\square = 1.1\,\mathrm{k\Omega/\square}$. In the second (optional) lithography step, a 50 nm thick niobium film is deposited to define Nb drive resonators, also at a rate of 1 nm/s. Accurate alignment of the Nb structures relative to the grAl resonators (cf. Fig. 2.1) is achieved using a Suss mask aligner.

A.2 Gralmonium Qubit Circuit Fabrication

The gralmonium qubit circuits presented in Section 3.1 and Chapter 5 are fabricated using a standard lift-off electron-beam lithography process on 330 µm, double-side polished c-plane sapphire substrates. The substrates are spin-coated with a bi-layer resist stack comprising ~ 700–800 nm MMA EL-13 and 300 nm PMMA A4, chosen for reliable lift-off and high-resolution patterning. To prevent charging during exposure, a 10 nm chromium anti-static layer is deposited prior to e-beam writing, which is conducted at 100 keV. Post-exposure, the chromium is removed by etching for 10 s, and the resist is developed in a (1 : 3) MIBK:isopropanol mixture using spray development. A subsequent Ar/O_2 plasma descum with a Kaufman ion source removes resist residues and surface contaminants. An additional titanium gettering step is used prior to deposition to further improve vacuum conditions. The 20 nm thick grAl layer is thermally evaporated at room temperature inside a Prevac deposition system, with a deposition rate of 1 nm/s in a dynamic oxygen atmosphere, yielding a chamber pressure between 10^{-5}–10^{-4} mbar. Lift-off is performed in acetone with ultrasonic agitation for seven minutes, followed by an ethanol rinse. The measured sheet resistance for the sample discussed in Section 3.1 is $R_\square = 1.5\,\mathrm{k\Omega/\square}$, corresponding to a resistivity of $\rho = 3000\,\mu\Omega\,\mathrm{cm}$.

A.3 Gradiometric Gralmonium Qubit Fabrication

The gradiometric gralmonium devices discussed in Section 3.2 and Chapter 6 were fabricated using a similar lift-off electron-beam lithography process with several key optimizations. A single-layer PMMA A4 resist is employed, covered with an 8 nm aluminum anti-static layer, which provides lower surface roughness and an easier stripping procedure compared to chromium. After 100 keV e-beam exposure, the aluminum anti-static layer is removed using tetramethylammonium hydroxide (TMAH) in MF319 developer. The resist is developed in a chilled 6 °C isopropanol/water (1:3) solution. Similar to the fabrication process described in Appendix A.2, we apply a 15 s Ar/O_2 plasma descum and a titanium gettering step prior to the metal deposition. A 20 nm grAl film is deposited using thermal evaporation in a Prevac system, yielding a sheet resistance of $R_\square = 1.0\,\mathrm{k\Omega/\square}$. The lift-off process involves sequential immersion in acetone, a 30 min N-ethyl-2-pyrrolidone (NEP) bath with ultrasonic cleaning, and a final ethanol rinse.

B Measurement setup

B.1 Sample holder

Figure B.1, depicts the readout and thermalization scheme employed for the samples investigated in this work. The superconducting circuit is patterned on a 3 mm × 10 mm sapphire chip, which is mounted inside a 3 mm copper tube that serves as a cylindrical

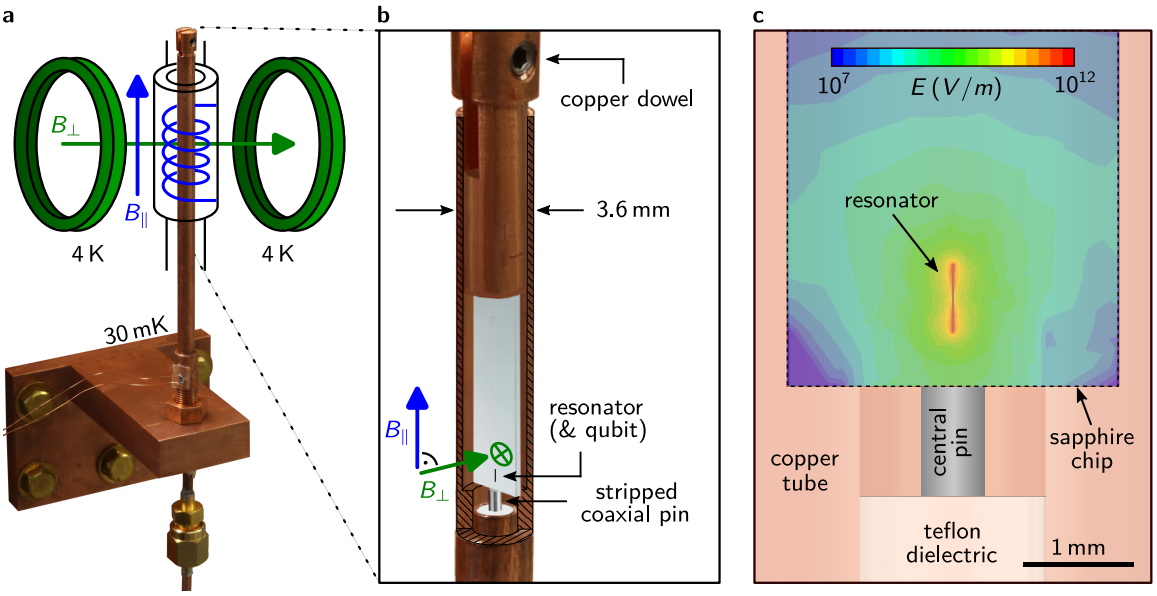

Figure B.1: Cylindrical waveguide sample holder. **a** Photograph of the cylindrical waveguide sample holder, embedded into a schematics of the vector magnet for field operation. The 2D vector magnet is thermalized on the 4 K stage of the cryostat and separated by a 1 mm gap from the cylindrical pipe of the sample holder, which is anchored at the base temperature of the cryostat. **b** Cross-sectional schematic zoom in on the sample holder. A 3 mm × 10 mm sapphire chip is mounted inside a cylindrical copper waveguide with 3 mm inner diameter and 0.3 mm wall thickness. It is secured using a copper dowel clamped against the inner wall. The copper dowel has a thin slit to enclose ~ 5 mm of the chip, which we fill with *Apiezon N* [167] vacuum grease to enhances thermal contact. The waveguide is operated below its ~ 60 GHz cut-off frequency, ensuring that microwave coupling occurs via the evanescent field of a stripped 2.2 mm coaxial cable pin, located approximately 0.5 mm from the chip's readout resonator. The coupling strength, which decays exponentially with increasing chip-pin separation, is tunable by axially adjusting the waveguide relative to the fixed coaxial pin. The solenoid coil applies magnetic fields in the substrate plane, while the Helmholtz pair is aligned perpendicular to the chip to control $B_\perp$ and enable magnetic flux tuning. No magnetic or thermal shielding is implemented between the sample holder and the vector magnet coils. **c** Finite element simulation of the electric field distribution within the sample holder. The electric field scale corresponds to an energy of 1 J. Adapted from Refs. [1, 3].

waveguide sample holder (outer diameter 3.3 mm). The sample holder is centered within a 2D vector magnet, separated by a 1 mm gap. We anchor the magnet on the 4 K stage of the cryostat to prevent heating of the base plate, which can arise for instance from ramping the magnetic field or sourcing high currents, both of which can induce dissipative vortex motion in the magnet windings. The 2D vector magnet consists of a solenoid generating a parallel magnetic field $B_{\parallel}$ in the substrate plane, and a Helmholtz pair for out-of-plane field control $B_{\perp}$. This configuration allows for precise flux biasing and compensation of residual perpendicular field components, typically arising from sample misalignment. For experiments involving large magnetic fields, the sample is not enclosed in additional magnetic shielding. In addition to external magnetic field fluctuations, sources of magnetic noise include power supply fluctuations, mechanical vibrations of the copper pipe, and vortex motion or retrapping in the magnet windings.

As shown in Fig. B.1b, the readout resonator is positioned in close proximity to the stripped inner conductor of a coaxial cable. Because we operate below the waveguide cut-off frequency of ~ 60 GHz, microwave coupling to the resonator is mediated by evanescent waves from the cable pin, enabling single-port reflection measurements. Finite-element simulations (cf. Fig. B.1c) confirm that the external quality factor Q_c scales exponentially with with the chip-pin separation, changing by approximately one order of magnitude per 0.5 mm. The coupling strength can be tuned between cooldowns via an $M5 \times 0.5$ fine-thread between the waveguide tube and the fixed copper block securing the coaxial cable. When the chip is in contact with the pin (strong coupling), the resonator is positioned approximately 0.5 mm from the pin.

Mechanical stability is ensured by clamping the chip with a partially enclosing copper dowel, which also aligns it with the vector magnet to within 1° tilt. We enhance thermal contact of the chip to the cryostat, using *Apiezon N* [167] vacuum grease applied within the dowel slit. Experiments requiring magnetic fields on the Tesla scale (e.g. in Chapter 2 and Section 3.2) are performed in a Sionludi dilution refrigerator, operating at a base temperature of $T_{\text{base}} = 30$ mK and equipped with the 2D vector magnet. In contrast, experiments characterizing the Gralmonium qubit in zero field (Section 3.1 and Chapter 5) were performed in a BlueFors dilution refrigerator with a base temperature of 15 mK, where flux biasing was implemented via a small coil anchored to the base plate. In this configuration, the sample holder was enclosed within a Cryoperm magnetic shield. Notably, across all experiments, the absence of infrared shielding contributes to an elevated thermal population in the qubit states (cf. Section 6.4).

B.2 Perpendicular field compensation procedure

As demonstrated in Ref. [139], perpendicular magnetic fields $B_{\perp}$ exceeding a resonator-width-dependent threshold induce a hysteretic, non-monotonic response in grAl resonators. This includes additional frequency shifts and microwave losses, potentially arising from coupling to spurious magnetic-field-sensitive modes. To avoid these detrimental effects, all high-field experiments in this work are conducted with magnetic fields applied strictly

in the plane of the substrate ($B_{\parallel}$), while minimizing residual out-of-plane field components ($B_{\perp}$).

Perpendicular magnetic fields can result from chip misalignment within the circular sample holder (cf. Appendix B.1), including both tilt and rotational offsets with respect to the solenoid axis of the main magnetic field. To mitigate this, we determine a compensation field $B_{\perp,\mathrm{comp}}$ for each value of $B_{\parallel}$, thereby ensuring:

- resonator measurements (Chapter 2 and Chapter 4) are performed under minimized effective $B_{\perp}$,
- Qubit measurements (Section 3.2 and Chapter 6) are conducted within the flux period closest to zero effective out-of-plane field.

The compensation procedure leverages the approximately three orders of magnitude higher magnetic susceptibility of grAl resonators to $B_{\perp}$ compared to $B_{\parallel}$. By sweeping the perpendicular field component and monitoring the associated quadratic suppression of the resonator frequency, we identify $B_{\perp,\mathrm{comp}}$ as the field that maximizes the resonator frequency – corresponding to the point of minimal perpendicular field exposure. For the gradiometric gralmonium qubit measurements in magnetic field, this procedure revealed an effective chip misalignment of 0.66 mT/T.

Bibliography

We note that large language models were employed during the preparation of this manuscript for AI assisted copyediting, including for example improvements to readability, grammar, and style. Their use was limited to refining human-written text generated by the author and did not involve autonomous content generation.

[1] S. Günzler, J. Beck, D. Rieger, N. Gosling, N. Zapata, M. Field, S. Geisert, A. Bacher, J. K. Hohmann, M. Spiecker, W. Wernsdorfer, and I. M. Pop, "Spin Environment of a Superconducting Qubit in High Magnetic Fields", arXiv, 10.48550/arXiv.2501.03661 (2025).

[2] S. Günzler, D. Rieger, M. Spiecker, T. Koch, G. A. Timco, R. E. P. Winpenny, I. M. Pop, and W. Wernsdorfer, "Kinetic inductance coupling for circuit QED with spins", arXiv, 10.48550/arXiv.2502.07605 (2025).

[3] D. Rieger, S. Günzler, M. Spiecker, P. Paluch, P. Winkel, L. Hahn, J. K. Hohmann, A. Bacher, W. Wernsdorfer, and I. M. Pop, "Granular aluminium nanojunction fluxonium qubit", Nat. Mater. **22**, 194–199 (2023).

[4] D. Rieger, S. Günzler, M. Spiecker, A. Nambisan, W. Wernsdorfer, and I. M. Pop, "Fano Interference in Microwave Resonator Measurements", Phys. Rev. Appl. **20**, 014059 (2023).

[5] N. Zapata, I. Takmakov, S. Günzler, S. Geisert, S. Ihssen, M. Field, A. Nambisan, D. Rieger, T. Reisinger, W. Wernsdorfer, and I. M. Pop, "Granular Aluminum Parametric Amplifier for Low-Noise Measurements in Tesla Fields", Phys. Rev. Lett. **133**, 260604 (2024).

[6] D. Gusenkova, F. Valenti, M. Spiecker, S. Günzler, P. Paluch, D. Rieger, L.-M. Pioraş-Ţimbolmaş, L. P. Zârbo, N. Casali, I. Colantoni, A. Cruciani, S. Pirro, L. Cardani, A. Petrescu, W. Wernsdorfer, P. Winkel, and I. M. Pop, "Operating in a deep underground facility improves the locking of gradiometric fluxonium qubits at the sweet spots", Appl. Phys. Lett. **120**, 054001 (2022).

[7] M. Spiecker, P. Paluch, N. Gosling, N. Drucker, S. Matityahu, D. Gusenkova, S. Günzler, D. Rieger, I. Takmakov, F. Valenti, P. Winkel, R. Gebauer, O. Sander, G. Catelani, A. Shnirman, A. V. Ustinov, W. Wernsdorfer, Y. Cohen, and I. M. Pop, "Two-level system hyperpolarization using a quantum Szilard engine", Nat. Phys. **19**, 1–6 (2023).

[8] D. Willsch, D. Rieger, P. Winkel, M. Willsch, C. Dickel, J. Krause, Y. Ando, R. Lescanne, Z. Leghtas, N. T. Bronn, P. Deb, O. Lanes, Z. K. Minev, B. Dennig, S. Geisert, S. Günzler, S. Ihssen, P. Paluch, T. Reisinger, R. Hanna, J. H. Bae, P. Schüffelgen, D. Grützmacher, L. Buimaga-Iarinca, C. Morari, W. Wernsdorfer, D. P. DiVincenzo, K. Michielsen, G. Catelani, and I. M. Pop, "Observation of Josephson harmonics in tunnel junctions", Nat. Phys. **20**, 815–821 (2024).

[9] S. Geisert, S. Ihssen, P. Winkel, M. Spiecker, M. Fechant, P. Paluch, N. Gosling, N. Zapata, S. Günzler, D. Rieger, D. Bénâtre, T. Reisinger, W. Wernsdorfer, and I. M. Pop, "Pure kinetic inductance coupling for cQED with flux qubits", Appl. Phys. Lett. **125**, 064002 (2024).

[10] R. P. Feynman, "Simulating physics with computers", Int. J. Theor. Phys. **21**, 467–488 (1982).

[11] Y. Cao, J. Romero, and A. Aspuru-Guzik, "Potential of quantum computing for drug discovery", IBM J. Res. Dev. **62**, 1–6 (2018).

[12] B. Bauer, S. Bravyi, M. Motta, and G. K.-L. Chan, "Quantum Algorithms for Quantum Chemistry and Quantum Materials Science", Chem. Rev. **120**, 12685–12717 (2020).

[13] N. Gisin, G. Ribordy, W. Tittel, and H. Zbinden, "Quantum cryptography", Rev. Mod. Phys. **74**, 145–195 (2002).

[14] C. H. Bennett and G. Brassard, "Quantum cryptography: Public key distribution and coin tossing", Theoret. Comput. Sci. **560**, 7–11 (2014).

[15] L.-M. Duan, M. D. Lukin, J. I. Cirac, and P. Zoller, "Long-distance quantum communication with atomic ensembles and linear optics", Nature **414**, 413–418 (2001).

[16] V. Giovannetti, S. Lloyd, and L. Maccone, "Quantum-Enhanced Measurements: Beating the Standard Quantum Limit", Science **306**, 1330–1336 (2004).

[17] C. L. Degen, F. Reinhard, and P. Cappellaro, "Quantum sensing", Rev. Mod. Phys. **89**, 035002 (2017).

[18] L. Pezzè, A. Smerzi, M. K. Oberthaler, R. Schmied, and P. Treutlein, "Quantum metrology with nonclassical states of atomic ensembles", Rev. Mod. Phys. **90**, 035005 (2018).

[19] G. Burkard, T. D. Ladd, A. Pan, J. M. Nichol, and J. R. Petta, "Semiconductor spin qubits", Rev. Mod. Phys. **95**, 025003 (2023).

[20] M. Zhong, M. P. Hedges, R. L. Ahlefeldt, J. G. Bartholomew, S. E. Beavan, S. M. Wittig, J. J. Longdell, and M. J. Sellars, "Optically addressable nuclear spins in a solid with a six-hour coherence time", Nature **517**, 177–180 (2015).

[21] D. Serrano, S. K. Kuppusamy, B. Heinrich, O. Fuhr, D. Hunger, M. Ruben, and P. Goldner, "Ultra-narrow optical linewidths in rare-earth molecular crystals", Nature **603**, 241–246 (2022).

[22] J. O'Sullivan, J. Travesedo, L. Pallegoix, Z. W. Huang, A. May, B. Yavkin, P. Hogan, S. Lin, R. Liu, T. Chaneliere, S. Bertaina, P. Goldner, D. Esteve, D. Vion, P. Abgrall, P. Bertet, and E. Flurin, "Individual solid-state nuclear spin qubits with coherence exceeding seconds", arXiv, `10.48550/arXiv.2410.10432` (2024).

[23] K. Serniak, S. Diamond, M. Hays, V. Fatemi, S. Shankar, L. Frunzio, R. J. Schoelkopf, and M. H. Devoret, "Direct Dispersive Monitoring of Charge Parity in Offset-Charge-Sensitive Transmons", Phys. Rev. Appl. **12**, 014052 (2019).

[24] M. McEwen, K. C. Miao, J. Atalaya, A. Bilmes, A. Crook, J. Bovaird, J. M. Kreikebaum, N. Zobrist, E. Jeffrey, B. Ying, A. Bengtsson, H.-S. Chang, A. Dunsworth, J. Kelly, Y. Zhang, E. Forati, R. Acharya, J. Iveland, W. Liu, S. Kim, B. Burkett, A. Megrant, Y. Chen, C. Neill, D. Sank, M. Devoret, and A. Opremcak, "Resisting High-Energy Impact Events through Gap Engineering in Superconducting Qubit Arrays", Phys. Rev. Lett. **133**, 240601 (2024).

[25] B. G. Christensen, C. D. Wilen, A. Opremcak, J. Nelson, F. Schlenker, C. H. Zimonick, L. Faoro, L. B. Ioffe, Y. J. Rosen, J. L. DuBois, B. L. T. Plourde, and R. McDermott, "Anomalous charge noise in superconducting qubits", Phys. Rev. B **100**, 140503 (2019).

[26] T. Connolly, P. D. Kurilovich, S. Diamond, H. Nho, C. G. L. Bøttcher, L. I. Glazman, V. Fatemi, and M. H. Devoret, "Coexistence of Nonequilibrium Density and Equilibrium Energy Distribution of Quasiparticles in a Superconducting Qubit", Phys. Rev. Lett. **132**, 217001 (2024).

[27] J. Krause, G. Marchegiani, L. M. Janssen, G. Catelani, Y. Ando, and C. Dickel, "Quasiparticle effects in magnetic-field-resilient three-dimensional transmons", Phys. Rev. Appl. **22**, 044063 (2024).

[28] P. Kumar, S. Sendelbach, M. A. Beck, J. W. Freeland, Z. Wang, H. Wang, C. C. Yu, R. Q. Wu, D. P. Pappas, and R. McDermott, "Origin and Reduction of $1/f$ Magnetic Flux Noise in Superconducting Devices", Phys. Rev. Appl. **6**, 041001 (2016).

[29] S. M. Anton, J. S. Birenbaum, S. R. O'Kelley, V. Bolkhovsky, D. A. Braje, G. Fitch, M. Neeley, G. C. Hilton, H.-M. Cho, K. D. Irwin, F. C. Wellstood, W. D. Oliver, A. Shnirman, and J. Clarke, "Magnetic Flux Noise in dc SQUIDs: Temperature and Geometry Dependence", Phys. Rev. Lett. **110**, 147002 (2013).

[30] J. Braumüller, L. Ding, A. P. Vepsäläinen, Y. Sung, M. Kjaergaard, T. Menke, R. Winik, D. Kim, B. M. Niedzielski, A. Melville, J. L. Yoder, C. F. Hirjibehedin, T. P. Orlando, S. Gustavsson, and W. D. Oliver, "Characterizing and Optimizing Qubit Coherence Based on SQUID Geometry", Phys. Rev. Appl. **13**, 054079 (2020).

[31] M. Stern, G. Catelani, Y. Kubo, C. Grezes, A. Bienfait, D. Vion, D. Esteve, and P. Bertet, "Flux Qubits with Long Coherence Times for Hybrid Quantum Circuits", Phys. Rev. Lett. **113**, 123601 (2014).

[32] F. Yoshihara, K. Harrabi, A. O. Niskanen, Y. Nakamura, and J. S. Tsai, "Decoherence of Flux Qubits due to $1/f$ Flux Noise", Phys. Rev. Lett. **97**, 167001 (2006).

[33] C. D. Nugroho, V. Orlyanchik, and D. J. Van Harlingen, "Low frequency resistance and critical current fluctuations in Al-based Josephson junctions", Appl. Phys. Lett. **102**, 142602 (2013).

[34] F. Yan, S. Gustavsson, A. Kamal, J. Birenbaum, A. P. Sears, D. Hover, T. J. Gudmundsen, D. Rosenberg, G. Samach, S. Weber, J. L. Yoder, T. P. Orlando, J. Clarke, A. J. Kerman, and W. D. Oliver, "The flux qubit revisited to enhance coherence and reproducibility", Nat. Commun. **7**, 1–9 (2016).

[35] C. Müller, J. H. Cole, and J. Lisenfeld, "Towards understanding two-level-systems in amorphous solids: insights from quantum circuits", Rep. Prog. Phys. **82**, 124501 (2019).

[36] T. Thorbeck, A. Eddins, I. Lauer, D. T. McClure, and M. Carroll, "Two-Level-System Dynamics in a Superconducting Qubit Due to Background Ionizing Radiation", PRX Quantum **4**, 020356 (2023).

[37] M. Odeh, K. Godeneli, E. Li, R. Tangirala, H. Zhou, X. Zhang, Z.-H. Zhang, and A. Sipahigil, "Non-Markovian dynamics of a superconducting qubit in a phononic bandgap", Nat. Phys., 1–6 (2025).

[38] Y. Kubo, F. R. Ong, P. Bertet, D. Vion, V. Jacques, D. Zheng, A. Dréau, J.-F. Roch, A. Auffeves, F. Jelezko, J. Wrachtrup, M. F. Barthe, P. Bergonzo, and D. Esteve, "Strong Coupling of a Spin Ensemble to a Superconducting Resonator", Phys. Rev. Lett. **105**, 140502 (2010).

[39] D. I. Schuster, A. P. Sears, E. Ginossar, L. DiCarlo, L. Frunzio, J. J. L. Morton, H. Wu, G. A. D. Briggs, B. B. Buckley, D. D. Awschalom, and R. J. Schoelkopf, "High-Cooperativity Coupling of Electron-Spin Ensembles to Superconducting Cavities", Phys. Rev. Lett. **105**, 140501 (2010).

[40] A. Bienfait, J. J. Pla, Y. Kubo, M. Stern, X. Zhou, C. C. Lo, C. D. Weis, T. Schenkel, M. L. W. Thewalt, D. Vion, D. Esteve, B. Julsgaard, K. Mølmer, J. J. L. Morton, and P. Bertet, "Reaching the quantum limit of sensitivity in electron spin resonance", Nat. Nanotechnol. **11**, 253–257 (2016).

[41] C. Eichler, A. J. Sigillito, S. A. Lyon, and J. R. Petta, "Electron Spin Resonance at the Level of 10^4 Spins Using Low Impedance Superconducting Resonators", Phys. Rev. Lett. **118**, 037701 (2017).

[42] C. Bonizzoni, A. Ghirri, M. Atzori, L. Sorace, R. Sessoli, and M. Affronte, "Coherent coupling between Vanadyl Phthalocyanine spin ensemble and microwave photons: towards integration of molecular spin qubits into quantum circuits", Sci. Rep. **7**, 1–8 (2017).

[43] M. Mergenthaler, J. Liu, J. J. Le Roy, N. Ares, A. L. Thompson, L. Bogani, F. Luis, S. J. Blundell, T. Lancaster, A. Ardavan, G. A. D. Briggs, P. J. Leek, and E. A. Laird, "Strong Coupling of Microwave Photons to Antiferromagnetic Fluctuations in an Organic Magnet", Phys. Rev. Lett. **119**, 147701 (2017).

[44] I. Gimeno, W. Kersten, M. C. Pallarés, P. Hermosilla, M. J. Martínez-Pérez, M. D. Jenkins, A. Angerer, C. Sánchez-Azqueta, D. Zueco, J. Majer, A. Lostao, and F. Luis, "Enhanced Molecular Spin-Photon Coupling at Superconducting Nanoconstrictions", ACS Nano **14**, 8707–8715 (2020).

[45] E. Moreno-Pineda and W. Wernsdorfer, "Measuring molecular magnets for quantum technologies", Nat. Rev. Phys. **3**, 645–659 (2021).

[46] Z. Wang, L. Balembois, M. Rančić, E. Billaud, M. Le Dantec, A. Ferrier, P. Goldner, S. Bertaina, T. Chanelière, D. Esteve, D. Vion, P. Bertet, and E. Flurin, "Single-electron spin resonance detection by microwave photon counting", Nature **619**, 276–281 (2023).

[47] A. Bienfait, J. J. Pla, Y. Kubo, X. Zhou, M. Stern, C. C. Lo, C. D. Weis, T. Schenkel, D. Vion, D. Esteve, J. J. L. Morton, and P. Bertet, "Controlling spin relaxation with a cavity", Nature **531**, 74–77 (2016).

[48] A. Blais, A. L. Grimsmo, S. M. Girvin, and A. Wallraff, "Circuit quantum electrodynamics", Rev. Mod. Phys. **93**, 025005 (2021).

[49] P. Haikka, Y. Kubo, A. Bienfait, P. Bertet, and K. Mølmer, "Proposal for detecting a single electron spin in a microwave resonator", Phys. Rev. A **95**, 022306 (2017).

[50] N. Didier, J. Bourassa, and A. Blais, "Fast Quantum Nondemolition Readout by Parametric Modulation of Longitudinal Qubit-Oscillator Interaction", Phys. Rev. Lett. **115**, 203601 (2015).

[51] S. Richer and D. DiVincenzo, "Circuit design implementing longitudinal coupling: A scalable scheme for superconducting qubits", Phys. Rev. B **93**, 134501 (2016).

[52] R. Dassonneville, T. Ramos, V. Milchakov, L. Planat, É. Dumur, F. Foroughi, J. Puertas, S. Leger, K. Bharadwaj, J. Delaforce, C. Naud, W. Hasch-Guichard, J. J. García-Ripoll, N. Roch, and O. Buisson, "Fast High-Fidelity Quantum Nondemolition Qubit Readout via a Nonperturbative Cross-Kerr Coupling", Phys. Rev. X **10**, 011045 (2020).

[53] R. Ruskov and C. Tahan, "Quantum-limited measurement of spin qubits via curvature couplings to a cavity", Phys. Rev. B **99**, 245306 (2019).

[54] S. Bosco, P. Scarlino, J. Klinovaja, and D. Loss, "Fully Tunable Longitudinal Spin-Photon Interactions in Si and Ge Quantum Dots", Phys. Rev. Lett. **129**, 066801 (2022).

[55] C. G. L. Bøttcher, S. P. Harvey, S. Fallahi, G. C. Gardner, M. J. Manfra, U. Vool, S. D. Bartlett, and A. Yacoby, "Parametric longitudinal coupling between a high-impedance superconducting resonator and a semiconductor quantum dot singlet-triplet spin qubit", Nat. Commun. **13**, 1–10 (2022).

[56] B. Harpt, J. Corrigan, N. Holman, P. Marciniec, D. Rosenberg, D. Yost, R. Das, R. Ruskov, C. Tahan, W. D. Oliver, R. McDermott, M. Friesen, and M. A. Eriksson, "Ultra-dispersive resonator readout of a quantum-dot qubit using longitudinal coupling", npj Quantum Inf. **11**, 1–4 (2025).

[57] C. A. Potts, R. C. Dekker, S. Deve, E. W. Strijbis, and G. A. Steele, "Strong Intrinsic Longitudinal Coupling in Circuit Quantum Electrodynamics", Phys. Rev. Lett. **134**, 153603 (2025).

[58] D. P. Divincenzo, "Topics in Quantum Computers", in *Mesoscopic Electron Transport* (Springer, Dordrecht, The Netherlands, 1997), pp. 657–677.

[59] Z.-L. Xiang, S. Ashhab, J. Q. You, and F. Nori, "Hybrid quantum circuits: Superconducting circuits interacting with other quantum systems", Rev. Mod. Phys. **85**, 623–653 (2013).

[60] G. Kurizki, P. Bertet, Y. Kubo, K. Mølmer, D. Petrosyan, P. Rabl, and J. Schmiedmayer, "Quantum technologies with hybrid systems", Proc. Natl. Acad. Sci. U.S.A. **112**, 3866–3873 (2015).

[61] A. A. Clerk, K. W. Lehnert, P. Bertet, J. R. Petta, and Y. Nakamura, "Hybrid quantum systems with circuit quantum electrodynamics", Nat. Phys. **16**, 257–267 (2020).

[62] R. Vincent, S. Klyatskaya, M. Ruben, W. Wernsdorfer, and F. Balestro, "Electronic read-out of a single nuclear spin using a molecular spin transistor", Nature **488**, 357–360 (2012).

[63] S. Thiele, F. Balestro, R. Ballou, S. Klyatskaya, M. Ruben, and W. Wernsdorfer, "Electrically driven nuclear spin resonance in single-molecule magnets", Science **344**, 1135–1138 (2014).

[64] J. Gao, J. Zmuidzinas, B. A. Mazin, H. G. LeDuc, and P. K. Day, "Noise properties of superconducting coplanar waveguide microwave resonators", Appl. Phys. Lett. **90**, 102507 (2007).

[65] A. Palacios-Laloy, F. Nguyen, F. Mallet, P. Bertet, D. Vion, and D. Esteve, "Tunable Resonators for Quantum Circuits", J. Low Temp. Phys. **151**, 1034–1042 (2008).

[66] R. Barends, J. J. A. Baselmans, S. J. C. Yates, J. R. Gao, J. N. Hovenier, and T. M. Klapwijk, "Quasiparticle Relaxation in Optically Excited High-Q Superconducting Resonators", Phys. Rev. Lett. **100**, 257002 (2008).

[67] M. R. Vissers, J. Gao, D. S. Wisbey, D. A. Hite, C. C. Tsuei, A. D. Corcoles, M. Steffen, and D. P. Pappas, "Low loss superconducting titanium nitride coplanar waveguide resonators", Appl. Phys. Lett. **97**, 232509 (2010).

[68] H. Paik and K. D. Osborn, "Reducing quantum-regime dielectric loss of silicon nitride for superconducting quantum circuits", Appl. Phys. Lett. **96**, 072505 (2010).

[69] S. J. Weber, K. W. Murch, D. H. Slichter, R. Vijay, and I. Siddiqi, "Single crystal silicon capacitors with low microwave loss in the single photon regime", Appl. Phys. Lett. **98**, 172510 (2011).

[70] M. Reagor, H. Paik, G. Catelani, L. Sun, C. Axline, E. Holland, I. M. Pop, N. A. Masluk, T. Brecht, L. Frunzio, M. H. Devoret, L. Glazman, and R. J. Schoelkopf, "Reaching 10 ms single photon lifetimes for superconducting aluminum cavities", Appl. Phys. Lett. **102**, 192604 (2013).

[71] Z. K. Minev, I. M. Pop, and M. H. Devoret, "Planar superconducting whispering gallery mode resonators", Appl. Phys. Lett. **103**, 142604 (2013).

[72] L. Grünhaupt, N. Maleeva, S. T. Skacel, M. Calvo, F. Levy-Bertrand, A. V. Ustinov, H. Rotzinger, A. Monfardini, G. Catelani, and I. M. Pop, "Loss Mechanisms and Quasiparticle Dynamics in Superconducting Microwave Resonators Made of Thin-Film Granular Aluminum", Phys. Rev. Lett. **121**, 117001 (2018).

[73] A. Shearrow, G. Koolstra, S. J. Whiteley, N. Earnest, P. S. Barry, F. J. Heremans, D. D. Awschalom, E. Shirokoff, and D. I. Schuster, "Atomic layer deposition of titanium nitride for quantum circuits", Appl. Phys. Lett. **113**, 212601 (2018).

[74] J. Verjauw, A. Potočnik, M. Mongillo, R. Acharya, F. Mohiyaddin, G. Simion, A. Pacco, T. Ivanov, D. Wan, A. Vanleenhove, L. Souriau, J. Jussot, A. Thiam, J. Swerts, X. Piao, S. Couet, M. Heyns, B. Govoreanu, and I. Radu, "Investigation of Microwave Loss Induced by Oxide Regrowth in High-Q Niobium Resonators", Phys. Rev. Appl. **16**, 014018 (2021).

[75] R. Gao, H.-S. Ku, H. Deng, W. Yu, T. Xia, F. Wu, Z. Song, M. Wang, X. Miao, C. Zhang, Y. Lin, Y. Shi, H.-H. Zhao, and C. Deng, "Ultrahigh Kinetic Inductance Superconducting Materials from Spinodal Decomposition", Advanced Materials **34**, 2201268 (2022).

[76] R. Barends, N. Vercruyssen, A. Endo, P. J. de Visser, T. Zijlstra, T. M. Klapwijk, P. Diener, S. J. C. Yates, and J. J. A. Baselmans, "Minimal resonator loss for circuit quantum electrodynamics", Appl. Phys. Lett. **97**, 023508 (2010).

[77] R. Barends, J. Wenner, M. Lenander, Y. Chen, R. C. Bialczak, J. Kelly, E. Lucero, P. O'Malley, M. Mariantoni, D. Sank, H. Wang, T. C. White, Y. Yin, J. Zhao, A. N. Cleland, J. M. Martinis, and J. J. A. Baselmans, "Minimizing quasiparticle generation from stray infrared light in superconducting quantum circuits", Appl. Phys. Lett. **99**, 113507 (2011).

[78] K. Geerlings, S. Shankar, E. Edwards, L. Frunzio, R. J. Schoelkopf, and M. H. Devoret, "Improving the quality factor of microwave compact resonators by optimizing their geometrical parameters", Applied Physics Letters **100**, 192601 (2012).

[79] M. R. Vissers, M. P. Weides, J. S. Kline, M. Sandberg, and D. P. Pappas, "Identifying capacitive and inductive loss in lumped element superconducting hybrid titanium nitride/aluminum resonators", Appl. Phys. Lett. **101**, 022601 (2012).

[80] I. Nsanzineza and B. L. T. Plourde, "Trapping a Single Vortex and Reducing Quasiparticles in a Superconducting Resonator", Phys. Rev. Lett. **113**, 117002 (2014).

[81] U. Patel, I. V. Pechenezhskiy, B. L. T. Plourde, M. G. Vavilov, and R. McDermott, "Phonon-mediated quasiparticle poisoning of superconducting microwave resonators", Phys. Rev. B **96**, 220501 (2017).

[82] J. D. Brehm, A. Bilmes, G. Weiss, A. V. Ustinov, and J. Lisenfeld, "Transmission-line resonators for the study of individual two-level tunneling systems", Appl. Phys. Lett. **111**, 112601 (2017).

[83] F. Henriques, F. Valenti, T. Charpentier, M. Lagoin, C. Gouriou, M. Martinez, L. Cardani, M. Vignati, L. Günhaupt, D. Gusenkova, J. Ferrero, S. T. Skacel, W. Wernsdorfer, A. V. Ustinov, G. Catelani, O. Sander, and I. M. Pop, "Phonon traps reduce the quasiparticle density in superconducting circuits", Appl. Phys. Lett. **115**, 212601 (2019).

[84] S. Ganjam, Y. Wang, Y. Lu, A. Banerjee, C. U. Lei, L. Krayzman, K. Kisslinger, C. Zhou, R. Li, Y. Jia, M. Liu, L. Frunzio, and R. J. Schoelkopf, "Surpassing millisecond coherence in on chip superconducting quantum memories by optimizing materials and circuit design", Nat. Commun. **15**, 1–13 (2024).

[85] A. Bruno, G. de Lange, S. Asaad, K. L. van der Enden, N. K. Langford, and L. DiCarlo, "Reducing intrinsic loss in superconducting resonators by surface treatment and deep etching of silicon substrates", Appl. Phys. Lett. **106**, 182601 (2015).

[86] G. Calusine, A. Melville, W. Woods, R. Das, C. Stull, V. Bolkhovsky, D. Braje, D. Hover, D. K. Kim, X. Miloshi, D. Rosenberg, A. Sevi, J. L. Yoder, E. Dauler, and W. D. Oliver, "Analysis and mitigation of interface losses in trenched superconducting coplanar waveguide resonators", Appl. Phys. Lett. **112**, 062601 (2018).

[87] S. E. de Graaf, L. Faoro, J. Burnett, A. A. Adamyan, A. Y. Tzalenchuk, S. E. Kubatkin, T. Lindström, and A. V. Danilov, "Suppression of low-frequency charge noise in superconducting resonators by surface spin desorption", Nat. Commun. **9**, 1–6 (2018).

[88] A. Melville, G. Calusine, W. Woods, K. Serniak, E. Golden, B. M. Niedzielski, D. K. Kim, A. Sevi, J. L. Yoder, E. A. Dauler, and W. D. Oliver, "Comparison of dielectric loss in titanium nitride and aluminum superconducting resonators", Appl. Phys. Lett. **117**, 124004 (2020).

[89] M. V. P. Altoé, A. Banerjee, C. Berk, A. Hajr, A. Schwartzberg, C. Song, M. Alghadeer, S. Aloni, M. J. Elowson, J. M. Kreikebaum, E. K. Wong, S. M. Griffin, S. Rao, A. Weber-Bargioni, A. M. Minor, D. I. Santiago, S. Cabrini, I. Siddiqi, and D. F. Ogletree, "Localization and Mitigation of Loss in Niobium Superconducting Circuits", PRX Quantum **3**, 020312 (2022).

[90] B. D. Josephson, "Possible new effects in superconductive tunnelling", Physics Letters **1**, 251–253 (1962).

[91] I. Siddiqi, "Engineering high-coherence superconducting qubits", Nat. Rev. Mater. **6**, 875–891 (2021).

[92] A. A. Golubov, M. Y. Kupriyanov, and E. Il'ichev, "The current-phase relation in Josephson junctions", Rev. Mod. Phys. **76**, 411–469 (2004).

[93] Y. Nakamura, Y. A. Pashkin, and J. S. Tsai, "Coherent control of macroscopic quantum states in a single-Cooper-pair box", Nature **398**, 786–788 (1999).

[94] D. Vion, A. Aassime, A. Cottet, P. Joyez, H. Pothier, C. Urbina, D. Esteve, and M. H. Devoret, "Manipulating the Quantum State of an Electrical Circuit", Science **296**, 886–889 (2002).

[95] I. Chiorescu, W. Wernsdorfer, A. Müller, H. Bögge, and B. Barbara, "Butterfly Hysteresis Loop and Dissipative Spin Reversal in the $S = 1/2$, V_{15} Molecular Complex", Phys. Rev. Lett. **84**, 3454–3457 (2000).

[96] Y. Makhlin, G. Schön, and A. Shnirman, "Quantum-state engineering with Josephson-junction devices", Rev. Mod. Phys. **73**, 357–400 (2001).

[97] G. Ithier, E. Collin, P. Joyez, P. J. Meeson, D. Vion, D. Esteve, F. Chiarello, A. Shnirman, Y. Makhlin, J. Schriefl, and G. Schön, "Decoherence in a superconducting quantum bit circuit", Phys. Rev. B **72**, 134519 (2005).

[98] U. Vool and M. Devoret, "Introduction to quantum electromagnetic circuits", Int. J. Circuit Theory Appl. **45**, 897–934 (2017).

[99] V. E. Manucharyan, J. Koch, L. I. Glazman, and M. H. Devoret, "Fluxonium: Single Cooper-Pair Circuit Free of Charge Offsets", Science **326**, 113–116 (2009).

[100] J. Koch, T. M. Yu, J. Gambetta, A. A. Houck, D. I. Schuster, J. Majer, A. Blais, M. H. Devoret, S. M. Girvin, and R. J. Schoelkopf, "Charge-insensitive qubit design derived from the Cooper pair box", Phys. Rev. A **76**, 042319 (2007).

[101] A. Somoroff, Q. Ficheux, R. A. Mencia, H. Xiong, R. Kuzmin, and V. E. Manucharyan, "Millisecond Coherence in a Superconducting Qubit", Phys. Rev. Lett. **130**, 267001 (2023).

[102] A. Lupaşcu, S. Saito, T. Picot, P. C. de Groot, C. J. P. M. Harmans, and J. E. Mooij, "Quantum non-demolition measurement of a superconducting two-level system", Nat. Phys. **3**, 119–123 (2007).

[103] D. Gusenkova, M. Spiecker, R. Gebauer, M. Willsch, D. Willsch, F. Valenti, N. Karcher, L. Grünhaupt, I. Takmakov, P. Winkel, D. Rieger, A. V. Ustinov, N. Roch, W. Wernsdorfer, K. Michielsen, O. Sander, and I. M. Pop, "Quantum Nondemolition Dispersive Readout of a Superconducting Artificial Atom Using Large Photon Numbers", Phys. Rev. Appl. **15**, 064030 (2021).

[104] R. Vijay, D. H. Slichter, and I. Siddiqi, "Observation of Quantum Jumps in a Superconducting Artificial Atom", Phys. Rev. Lett. **106**, 110502 (2011).

[105] Q. Ficheux, S. Jezouin, Z. Leghtas, and B. Huard, "Dynamics of a qubit while simultaneously monitoring its relaxation and dephasing", Nat. Commun. **9**, 1–6 (2018).

[106] Z. K. Minev, S. O. Mundhada, S. Shankar, P. Reinhold, R. Gutiérrez-Jáuregui, R. J. Schoelkopf, M. Mirrahimi, H. J. Carmichael, and M. H. Devoret, "To catch and reverse a quantum jump mid-flight", Nature **570**, 200–204 (2019).

[107] R. Vijay, C. Macklin, D. H. Slichter, S. J. Weber, K. W. Murch, R. Naik, A. N. Korotkov, and I. Siddiqi, "Stabilizing Rabi oscillations in a superconducting qubit using quantum feedback", Nature **490**, 77–80 (2012).

[108] V. V. Sivak, A. Eickbusch, B. Royer, S. Singh, I. Tsioutsios, S. Ganjam, A. Miano, B. L. Brock, A. Z. Ding, L. Frunzio, S. M. Girvin, R. J. Schoelkopf, and M. H. Devoret, "Real-time quantum error correction beyond break-even", Nature **616**, 50–55 (2023).

[109] S. Krinner, N. Lacroix, A. Remm, A. Di Paolo, E. Genois, C. Leroux, C. Hellings, S. Lazar, F. Swiadek, J. Herrmann, G. J. Norris, C. K. Andersen, M. Müller, A. Blais, C. Eichler, and A. Wallraff, "Realizing repeated quantum error correction in a distance-three surface code", Nature **605**, 669–674 (2022).

[110] P. Campagne-Ibarcq, A. Eickbusch, S. Touzard, E. Zalys-Geller, N. E. Frattini, V. V. Sivak, P. Reinhold, S. Puri, S. Shankar, R. J. Schoelkopf, L. Frunzio, M. Mirrahimi, and M. H. Devoret, "Quantum error correction of a qubit encoded in grid states of an oscillator", Nature **584**, 368–372 (2020).

[111] N. Ofek, A. Petrenko, R. Heeres, P. Reinhold, Z. Leghtas, B. Vlastakis, Y. Liu, L. Frunzio, S. M. Girvin, L. Jiang, M. Mirrahimi, M. H. Devoret, and R. J. Schoelkopf, "Extending the lifetime of a quantum bit with error correction in superconducting circuits", Nature **536**, 441–445 (2016).

[112] N. Crescini, S. Cailleaux, W. Guichard, C. Naud, O. Buisson, K. W. Murch, and N. Roch, "Evidence of dual Shapiro steps in a Josephson junction array", Nat. Phys. **19**, 851–856 (2023).

[113] R. S. Shaikhaidarov, K. H. Kim, J. W. Dunstan, I. V. Antonov, S. Linzen, M. Ziegler, D. S. Golubev, V. N. Antonov, E. V. Il'ichev, and O. V. Astafiev, "Quantized current steps due to the a.c. coherent quantum phase-slip effect", Nature **608**, 45–49 (2022).

[114] F. Kaap, C. Kissling, V. Gaydamachenko, L. Grünhaupt, and S. Lotkhov, "Demonstration of dual Shapiro steps in small Josephson junctions", Nat. Commun. **15**, 1–6 (2024).

[115] B. Saxberg, A. Vrajitoarea, G. Roberts, M. G. Panetta, J. Simon, and D. I. Schuster, "Disorder-assisted assembly of strongly correlated fluids of light", Nature **612**, 435–441 (2022).

[116] M. Bild, M. Fadel, Y. Yang, U. von Lüpke, P. Martin, A. Bruno, and Y. Chu, "Schrödinger cat states of a 16-microgram mechanical oscillator", Science **380**, 274–278 (2023).

[117] S. Storz, J. Schär, A. Kulikov, P. Magnard, P. Kurpiers, J. Lütolf, T. Walter, A. Copetudo, K. Reuer, A. Akin, J.-C. Besse, M. Gabureac, G. J. Norris, A. Rosario, F. Martin, J. Martinez, W. Amaya, M. W. Mitchell, C. Abellan, J.-D. Bancal, N. Sangouard, B. Royer, A. Blais, and A. Wallraff, "Loophole-free Bell inequality violation with superconducting circuits", Nature **617**, 265–270 (2023).

[118] R. Assouly, R. Dassonneville, T. Peronnin, A. Bienfait, and B. Huard, "Quantum advantage in microwave quantum radar", Nat. Phys. **19**, 1418–1422 (2023).

[119] G. Wendin, "Quantum information processing with superconducting circuits: a review", Rep. Prog. Phys. **80**, 106001 (2017).

[120] I. M. Pop, K. Geerlings, G. Catelani, R. J. Schoelkopf, L. I. Glazman, and M. H. Devoret, "Coherent suppression of electromagnetic dissipation due to superconducting quasiparticles", Nature **508**, 369–372 (2014).

[121] A. Kou, W. C. Smith, U. Vool, I. M. Pop, K. M. Sliwa, M. Hatridge, L. Frunzio, and M. H. Devoret, "Simultaneous Monitoring of Fluxonium Qubits in a Waveguide", Phys. Rev. Appl. **9**, 064022 (2018).

[122] U. Vool, A. Kou, W. C. Smith, N. E. Frattini, K. Serniak, P. Reinhold, I. M. Pop, S. Shankar, L. Frunzio, S. M. Girvin, and M. H. Devoret, "Driving Forbidden Transitions in the Fluxonium Artificial Atom", Phys. Rev. Appl. **9**, 054046 (2018).

[123] L. B. Nguyen, Y.-H. Lin, A. Somoroff, R. Mencia, N. Grabon, and V. E. Manucharyan, "High-Coherence Fluxonium Qubit", Phys. Rev. X **9**, 041041 (2019).

[124] L. Grünhaupt, M. Spiecker, D. Gusenkova, N. Maleeva, S. T. Skacel, I. Takmakov, F. Valenti, P. Winkel, H. Rotzinger, W. Wernsdorfer, A. V. Ustinov, and I. M. Pop, "Granular aluminium as a superconducting material for high-impedance quantum circuits", Nat. Mater. **18**, 816–819 (2019).

[125] M. Pita-Vidal, A. Bargerbos, C.-K. Yang, D. J. van Woerkom, W. Pfaff, N. Haider, P. Krogstrup, L. P. Kouwenhoven, G. de Lange, and A. Kou, "Gate-Tunable Field-Compatible Fluxonium", Phys. Rev. Appl. **14**, 064038 (2020).

[126] M. Janík, K. Roux, C. Borja-Espinosa, O. Sagi, A. Baghdadi, T. Adletzberger, S. Calcaterra, M. Botifoll, A. Garzón Manjón, J. Arbiol, D. Chrastina, G. Isella, I. M. Pop, and G. Katsaros, "Strong charge-photon coupling in planar germanium enabled by granular aluminium superinductors", Nat. Commun. **16**, 1–9 (2025).

[127] M. Peruzzo, A. Trioni, F. Hassani, M. Zemlicka, and J. M. Fink, "Surpassing the Resistance Quantum with a Geometric Superinductor", Phys. Rev. Appl. **14**, 044055 (2020).

[128] M. Peruzzo, F. Hassani, G. Szep, A. Trioni, E. Redchenko, M. Žemlička, and J. M. Fink, "Geometric Superinductance Qubits: Controlling Phase Delocalization across a Single Josephson Junction", PRX Quantum **2**, 040341 (2021).

[129] F. Valenti, "Diagnostics and abatement of quasiparticle poisoning in superconducting quantum circuits", 47.12.03; LK 01, PhD thesis (Karlsruher Institut für Technologie (KIT), 2021), 133 pp.

[130] M. Tinkham, *Introduction to superconductivity* (Dover Publications, Mineola, 2004).

[131] S. E. de Graaf, S. T. Skacel, T. Hönigl-Decrinis, R. Shaikhaidarov, H. Rotzinger, S. Linzen, M. Ziegler, U. Hübner, H.-G. Meyer, V. Antonov, E. Il'ichev, A. V. Ustinov, A. Y. Tzalenchuk, and O. V. Astafiev, "Charge quantum interference device", Nat. Phys. **14**, 590–594 (2018).

[132] J. T. Peltonen, O. V. Astafiev, Y. P. Korneeva, B. M. Voronov, A. A. Korneev, I. M. Charaev, A. V. Semenov, G. N. Golt'sman, L. B. Ioffe, T. M. Klapwijk, and J. S. Tsai, "Coherent flux tunneling through NbN nanowires", Phys. Rev. B **88**, 220506 (2013).

[133] J. T. Peltonen, Z. H. Peng, Y. P. Korneeva, B. M. Voronov, A. A. Korneev, A. V. Semenov, G. N. Gol'tsman, J. S. Tsai, and O. V. Astafiev, "Coherent dynamics and decoherence in a superconducting weak link", Phys. Rev. B **94**, 180508 (2016).

[134] J. G. Kroll, F. Borsoi, K. L. van der Enden, W. Uilhoorn, D. de Jong, M. Quintero-Pérez, D. J. van Woerkom, A. Bruno, S. R. Plissard, D. Car, E. P. A. M. Bakkers, M. C. Cassidy, and L. P. Kouwenhoven, "Magnetic-Field-Resilient Superconducting Coplanar-Waveguide Resonators for Hybrid Circuit Quantum Electrodynamics Experiments", Phys. Rev. Appl. **11**, 064053 (2019).

[135] N. Samkharadze, A. Bruno, P. Scarlino, G. Zheng, D. P. DiVincenzo, L. DiCarlo, and L. M. K. Vandersypen, "High-Kinetic-Inductance Superconducting Nanowire Resonators for Circuit QED in a Magnetic Field", Phys. Rev. Appl. **5**, 044004 (2016).

[136] A. Bahr, M. Boselli, B. Huard, and A. Bienfait, "Improving magnetic-field resilience of NbTiN planar resonators using a hard-mask fabrication technique", Appl. Phys. Lett. **124**, 10.1063/5.0191393 (2024).

[137] O. V. Astafiev, L. B. Ioffe, S. Kafanov, Y. A. Pashkin, K. Y. Arutyunov, D. Shahar, O. Cohen, and J. S. Tsai, "Coherent quantum phase slip", Nature **484**, 355–358 (2012).

[138] T. Charpentier, D. Perconte, S. Léger, K. R. Amin, F. Blondelle, F. Gay, O. Buisson, L. Ioffe, A. Khvalyuk, I. Poboiko, M. Feigel'man, N. Roch, and B. Sacépé, "First-order quantum breakdown of superconductivity in an amorphous superconductor", Nat. Phys. **21**, 104–109 (2025).

[139] K. Borisov, D. Rieger, P. Winkel, F. Henriques, F. Valenti, A. Ionita, M. Wessbecher, M. Spiecker, D. Gusenkova, I. M. Pop, and W. Wernsdorfer, "Superconducting granular aluminum resonators resilient to magnetic fields up to 1 Tesla", Appl. Phys. Lett. **117**, 120502 (2020).

[140] G. Deutscher, H. Fenichel, M. Gershenson, E. Grünbaum, and Z. Ovadyahu, "Transition to zero dimensionality in granular aluminum superconducting films", J. Low Temp. Phys. **10**, 231–243 (1973).

[141] R. W. Cohen and B. Abeles, "Superconductivity in Granular Aluminum Films", Phys. Rev. **168**, 444–450 (1968).

[142] A. Glezer Moshe, E. Farber, and G. Deutscher, "Granular superconductors for high kinetic inductance and low loss quantum devices", Appl. Phys. Lett. **117**, 062601 (2020).

[143] F. Levy-Bertrand, T. Klein, T. Grenet, O. Dupré, A. Benoit, A. Bideaud, O. Bourrion, M. Calvo, A. Catalano, A. Gomez, J. Goupy, L. Grünhaupt, U. v. Luepke, N. Maleeva, F. Valenti, I. M. Pop, and A. Monfardini, "Electrodynamics of granular aluminum from superconductor to insulator: Observation of collective superconducting modes", Phys. Rev. B **99**, 094506 (2019).

[144] M. Kristen, J. N. Voss, M. Wildermuth, A. Bilmes, J. Lisenfeld, H. Rotzinger, and A. V. Ustinov, "Giant Two-Level Systems in a Granular Superconductor", Phys. Rev. Lett. **132**, 217002 (2024).

[145] H. Rotzinger, S. T. Skacel, M. Pfirrmann, J. N. Voss, J. Münzberg, S. Probst, P. Bushev, M. P. Weides, A. V. Ustinov, and J. E. Mooij, "Aluminium-oxide wires for superconducting high kinetic inductance circuits", Supercond. Sci. Technol. **30**, 025002 (2016).

[146] V. Gupta, P. Winkel, N. Thakur, P. van Vlaanderen, Y. Wang, S. Ganjam, L. Frunzio, and R. J. Schoelkopf, "Low-loss lumped-element inductors made from granular aluminum", Phys. Rev. Appl. **23**, 054067 (2025).

[147] C. Roy, S. Frasca, and P. Scarlino, "Study of Magnetic Field Resilient High Impedance High-Kinetic Inductance Superconducting Resonators", arXiv, 10.48550/arXiv.2503.13321 (2025).

[148] P. Winkel, K. Borisov, L. Grünhaupt, D. Rieger, M. Spiecker, F. Valenti, A. V. Ustinov, W. Wernsdorfer, and I. M. Pop, "Implementation of a Transmon Qubit Using Superconducting Granular Aluminum", Phys. Rev. X **10**, 031032 (2020).

[149] A. Théry, B. Neukelmance, B. Hue, W. Legrand, L. Jarjat, J. Craquelin, M. Villiers, A. Cottet, M. R. Delbecq, and T. Kontos, "Observation of quantum oscillations in the extreme weak anharmonic limit", Phys. Rev. B **109**, 064505 (2024).

[150] N. Maleeva, L. Grünhaupt, T. Klein, F. Levy-Bertrand, O. Dupre, M. Calvo, F. Valenti, P. Winkel, F. Friedrich, W. Wernsdorfer, A. V. Ustinov, H. Rotzinger, A. Monfardini, M. V. Fistul, and I. M. Pop, "Circuit quantum electrodynamics of granular aluminum resonators", Nat. Commun. **9**, 1–7 (2018).

[151] A. J. Annunziata, D. F. Santavicca, L. Frunzio, G. Catelani, M. J. Rooks, A. Frydman, and D. E. Prober, "Tunable superconducting nanoinductors", Nanotechnology **21**, 445202 (2010).

[152] G. Tosi, F. A. Mohiyaddin, H. Huebl, and A. Morello, "Circuit-quantum electrodynamics with direct magnetic coupling to single-atom spin qubits in isotopically enriched 28Si", AIP Adv. **4**, 10.1063/1.4893242 (2014).

[153] G. Franco-Rivera, J. Cochran, S. Miyashita, S. Bertaina, and I. Chiorescu, "Strong Coupling of a Gd^{3+} Multilevel Spin System to an On-Chip Superconducting Resonator", Phys. Rev. Appl. **19**, 024067 (2023).

[154] R. J. Schoelkopf and S. M. Girvin, "Wiring up quantum systems", Nature **451**, 664–669 (2008).

[155] M. F. Dumas, B. Groleau-Paré, A. McDonald, M. H. Muñoz-Arias, C. Lledó, B. D'Anjou, and A. Blais, "Measurement-Induced Transmon Ionization", Phys. Rev. X **14**, 041023 (2024).

[156] D. Sank, Z. Chen, M. Khezri, J. Kelly, R. Barends, B. Campbell, Y. Chen, B. Chiaro, A. Dunsworth, A. Fowler, E. Jeffrey, E. Lucero, A. Megrant, J. Mutus, M. Neeley, C. Neill, P. J. J. O'Malley, C. Quintana, P. Roushan, A. Vainsencher, T. White, J. Wenner, A. N. Korotkov, and J. M. Martinis, "Measurement-Induced State Transitions in a Superconducting Qubit: Beyond the Rotating Wave Approximation", Phys. Rev. Lett. **117**, 190503 (2016).

[157] J. Cohen, A. Petrescu, R. Shillito, and A. Blais, "Reminiscence of Classical Chaos in Driven Transmons", PRX Quantum **4**, 020312 (2023).

[158] E. A. Sete, J. M. Gambetta, and A. N. Korotkov, "Purcell effect with microwave drive: Suppression of qubit relaxation rate", Phys. Rev. B **89**, 104516 (2014).

[159] W. Wernsdorfer, "From micro- to nano-SQUIDs: applications to nanomagnetism", Supercond. Sci. Technol. **22**, 064013 (2009).

[160] S. Günzler, P. Winkel, D. Rieger, K. Borisov, M. Spiecker, A. V. Ustinov, I. M. Pop, and W. Wernsdorfer, "Superconducting microwave magnetometer for absolute flux detection", arXiv, 10.48550/arXiv.2107.05929 (2021).

[161] J. Luomahaara, V. Vesterinen, L. Grönberg, and J. Hassel, "Kinetic inductance magnetometer", Nat. Commun. **5**, 1–7 (2014).

[162] A. T. Asfaw, E. I. Kleinbaum, T. M. Hazard, A. Gyenis, A. A. Houck, and S. A. Lyon, "SKIFFS: Superconducting Kinetic Inductance Field-Frequency Sensors for sensitive magnetometry in moderate background magnetic fields", Appl. Phys. Lett. **113**, 10.1063/1.5049615 (2018).

[163] S. Sypkens, F. Faramarzi, M. Colangelo, A. Sinclair, R. Stephenson, and J. Glasby, "Development of an Array of Kinetic Inductance Magnetometers (KIMs)", IEEE Trans. Appl. Supercond. **31**, ArticleSequenceNumber:2400104 (2021).

[164] F. K. Larsen, E. J. L. McInnes, H. E. Mkami, J. Overgaard, S. Piligkos, G. Rajaraman, E. Rentschler, A. A. Smith, G. M. Smith, V. Boote, M. Jennings, G. A. Timco, and R. E. P. Winpenny, "Synthesis and Characterization of Heterometallic {Cr7M} Wheels", Angew. Chem. **115**, 105–109 (2003).

[165] A. Ardavan, O. Rival, J. J. L. Morton, S. J. Blundell, A. M. Tyryshkin, G. A. Timco, and R. E. P. Winpenny, "Will Spin-Relaxation Times in Molecular Magnets Permit Quantum Information Processing?", Phys. Rev. Lett. **98**, 057201 (2007).

[166] G. A. Timco, S. Carretta, F. Troiani, F. Tuna, R. J. Pritchard, C. A. Muryn, E. J. L. McInnes, A. Ghirri, A. Candini, P. Santini, G. Amoretti, M. Affronte, and R. E. P. Winpenny, "Engineering the coupling between molecular spin qubits by coordination chemistry", Nat. Nanotechnol. **4**, 173–178 (2009).

[167] *Apiezon N Grease*, [Online; accessed 15. Apr. 2024], Apr. 2024.

[168] B. Ho Eom, P. K. Day, H. G. LeDuc, and J. Zmuidzinas, "A wideband, low-noise superconducting amplifier with high dynamic range", Nat. Phys. **8**, 623–627 (2012).

[169] J. Zmuidzinas, "Superconducting Microresonators: Physics and Applications", Annu. Rev. Condens. Matter Phys., 169–214 (2012).

[170] D. Rieger, "Gralmonium – granular aluminum nano-junction fluxonium qubit", 47.12.01; LK 01, PhD thesis (Karlsruher Institut für Technologie (KIT), 2024), 103 pp.

[171] J. M. Kreikebaum, K. P. O'Brien, A. Morvan, and I. Siddiqi, "Improving wafer-scale Josephson junction resistance variation in superconducting quantum coherent circuits", Supercond. Sci. Technol. **33**, 06LT02 (2020).

[172] H. Paik, D. I. Schuster, L. S. Bishop, G. Kirchmair, G. Catelani, A. P. Sears, B. R. Johnson, M. J. Reagor, L. Frunzio, L. I. Glazman, S. M. Girvin, M. H. Devoret, and R. J. Schoelkopf, "Observation of High Coherence in Josephson Junction Qubits Measured in a Three-Dimensional Circuit QED Architecture", Phys. Rev. Lett. **107**, 240501 (2011).

[173] A. P. M. Place, L. V. H. Rodgers, P. Mundada, B. M. Smitham, M. Fitzpatrick, Z. Leng, A. Premkumar, J. Bryon, A. Vrajitoarea, S. Sussman, G. Cheng, T. Madhavan, H. K. Babla, X. H. Le, Y. Gang, B. Jäck, A. Gyenis, N. Yao, R. J. Cava, N. P. de Leon, and A. A. Houck, "New material platform for superconducting transmon qubits with coherence times exceeding 0.3 milliseconds", Nat. Commun. **12**, 1–6 (2021).

[174] A. A. Pishchimova, N. S. Smirnov, D. A. Ezenkova, E. A. Krivko, E. V. Zikiy, D. O. Moskalev, A. I. Ivanov, N. D. Korshakov, and I. A. Rodionov, "Improving Josephson junction reproducibility for superconducting quantum circuits: junction area fluctuation", Sci. Rep. **13**, 1–7 (2023).

[175] A. Schneider, T. Wolz, M. Pfirrmann, M. Spiecker, H. Rotzinger, A. V. Ustinov, and M. Weides, "Transmon qubit in a magnetic field: Evolution of coherence and transition frequency", Phys. Rev. Res. **1**, 023003 (2019).

[176] J. Krause, C. Dickel, E. Vaal, M. Vielmetter, J. Feng, R. Bounds, G. Catelani, J. M. Fink, and Y. Ando, "Magnetic Field Resilience of Three-Dimensional Transmons with Thin-Film Al/AlO_x/Al Josephson Junctions Approaching 1 T", Phys. Rev. Appl. **17**, 034032 (2022).

[177] D. A. Rower, L. Ateshian, L. H. Li, M. Hays, D. Bluvstein, L. Ding, B. Kannan, A. Almanakly, J. Braumüller, D. K. Kim, A. Melville, B. M. Niedzielski, M. E. Schwartz, J. L. Yoder, T. P. Orlando, J. I.-J. Wang, S. Gustavsson, J. A. Grover, K. Serniak, R. Comin, and W. D. Oliver, "Evolution of $1/f$ Flux Noise in Superconducting Qubits with Weak Magnetic Fields", Phys. Rev. Lett. **130**, 220602 (2023).

[178] M. Hays, V. Fatemi, D. Bouman, J. Cerrillo, S. Diamond, K. Serniak, T. Connolly, P. Krogstrup, J. Nygård, A. L. Yeyati, A. Geresdi, and M. H. Devoret, "Coherent manipulation of an Andreev spin qubit", Science **373**, 430–433 (2021).

[179] T. W. Larsen, K. D. Petersson, F. Kuemmeth, T. S. Jespersen, P. Krogstrup, J. Nygård, and C. M. Marcus, "Semiconductor-Nanowire-Based Superconducting Qubit", Phys. Rev. Lett. **115**, 127001 (2015).

[180] G. de Lange, B. van Heck, A. Bruno, D. J. van Woerkom, A. Geresdi, S. R. Plissard, E. P. A. M. Bakkers, A. R. Akhmerov, and L. DiCarlo, "Realization of Microwave Quantum Circuits Using Hybrid Superconducting-Semiconducting Nanowire Josephson Elements", Phys. Rev. Lett. **115**, 127002 (2015).

[181] A. Kringhøj, T. W. Larsen, O. Erlandsson, W. Uilhoorn, J. G. Kroll, M. Hesselberg, R. P. G. McNeil, P. Krogstrup, L. Casparis, C. M. Marcus, and K. D. Petersson, "Magnetic-Field-Compatible Superconducting Transmon Qubit", Phys. Rev. Appl. **15**, 054001 (2021).

[182] D. Sabonis, O. Erlandsson, A. Kringhøj, B. van Heck, T. W. Larsen, I. Petkovic, P. Krogstrup, K. D. Petersson, and C. M. Marcus, "Destructive Little-Parks Effect in a Full-Shell Nanowire-Based Transmon", Phys. Rev. Lett. **125**, 156804 (2020).

[183] F. Luthi, T. Stavenga, O. W. Enzing, A. Bruno, C. Dickel, N. K. Langford, M. A. Rol, T. S. Jespersen, J. Nygård, P. Krogstrup, and L. DiCarlo, "Evolution of Nanowire Transmon Qubits and Their Coherence in a Magnetic Field", Phys. Rev. Lett. **120**, 100502 (2018).

[184] J. G. Kroll, W. Uilhoorn, K. L. van der Enden, D. de Jong, K. Watanabe, T. Taniguchi, S. Goswami, M. C. Cassidy, and L. P. Kouwenhoven, "Magnetic field compatible circuit quantum electrodynamics with graphene Josephson junctions", Nat. Commun. **9**, 1–5 (2018).

[185] S. K. H. Lam, "Noise properties of SQUIDs made from nanobridges", Supercond. Sci. Technol. **19**, 963 (2006).

[186] J. E. Mooij and C. J. P. M. Harmans, "Phase-slip flux qubits", New J. Phys. **7**, 219 (2005).

[187] D. Kiselov, M. A. Skvortsov, and M. V. Feigel'man, "Gapful electrons in a vortex core in granular superconductors", SciPost Phys. **15**, 008 (2023).

[188] G. Rastelli, I. M. Pop, and F. W. J. Hekking, "Quantum phase slips in Josephson junction rings", Phys. Rev. B **87**, 174513 (2013).

[189] K. A. Matveev, A. I. Larkin, and L. I. Glazman, "Persistent Current in Superconducting Nanorings", Phys. Rev. Lett. **89**, 096802 (2002).

[190] F. Friedrich, P. Winkel, K. Borisov, H. Seeger, C. Sürgers, I. M. Pop, and W. Wernsdorfer, "Onset of phase diffusion in high kinetic inductance granular aluminum micro-SQUIDs", Supercond. Sci. Technol. **32**, 125008 (2019).

[191] P. Winkel, "Superconducting quantum circuits for hybrid architectures", PhD thesis (Karlsruher Institut für Technologie (KIT), 2020), 273 pp.

[192] P. Winkel, I. Takmakov, D. Rieger, L. Planat, W. Hasch-Guichard, L. Grünhaupt, N. Maleeva, F. Foroughi, F. Henriques, K. Borisov, J. Ferrero, A. V. Ustinov, W. Wernsdorfer, N. Roch, and I. M. Pop, "Nondegenerate Parametric Amplifiers Based on Dispersion-Engineered Josephson-Junction Arrays", Phys. Rev. Appl. **13**, 024015 (2020).

[193] A. Glezer Moshe, E. Farber, and G. Deutscher, "From orbital to Pauli-limited critical fields in granular aluminum films", Phys. Rev. Res. **2**, 043354 (2020).

[194] J. N. Voss, Y. Schön, M. Wildermuth, D. Dorer, J. H. Cole, H. Rotzinger, and A. V. Ustinov, "Eliminating Quantum Phase Slips in Superconducting Nanowires", ACS Nano **15**, 4108–4114 (2021).

[195] J. Schriefl, Y. Makhlin, A. Shnirman, and G. Schön, "Decoherence from ensembles of two-level fluctuators", New J. Phys. **8**, 1 (2006).

[196] D. J. Van Harlingen, T. L. Robertson, B. L. T. Plourde, P. A. Reichardt, T. A. Crane, and J. Clarke, "Decoherence in Josephson-junction qubits due to critical-current fluctuations", Phys. Rev. B **70**, 064517 (2004).

[197] U. Eckern, G. Schön, and V. Ambegaokar, "Quantum dynamics of a superconducting tunnel junction", Phys. Rev. B **30**, 6419–6431 (1984).

[198] J. R. Friedman and D. V. Averin, "Aharonov-Casher-Effect Suppression of Macroscopic Tunneling of Magnetic Flux", Phys. Rev. Lett. **88**, 050403 (2002).

[199] I. M. Pop, B. Douçot, L. Ioffe, I. Protopopov, F. Lecocq, I. Matei, O. Buisson, and W. Guichard, "Experimental demonstration of Aharonov-Casher interference in a Josephson junction circuit", Phys. Rev. B **85**, 094503 (2012).

[200] V. E. Manucharyan, N. A. Masluk, A. Kamal, J. Koch, L. I. Glazman, and M. H. Devoret, "Evidence for coherent quantum phase slips across a Josephson junction array", Phys. Rev. B **85**, 024521 (2012).

[201] M. J. Schwarz, J. Goetz, Z. Jiang, T. Niemczyk, F. Deppe, A. Marx, and R. Gross, "Gradiometric flux qubits with a tunable gap", New J. Phys. **15**, 045001 (2013).

[202] D. Bénâtre, M. Féchant, N. Zapata, N. Gosling, P. Paluch, T. Reisinger, and I. M. Pop, "Simultaneous sweet-spot locking of gradiometric fluxonium qubits", arXiv, 10.48550/arXiv.2505.08769 (2025).

[203] A. Deshpande, J. Pusskeiler, C. Prange, U. Rogge, M. Dressel, and M. Scheffler, "Tuning the superconducting dome in granular aluminum thin films", J. Appl. Phys. **137**, 10.1063/5.0250146 (2025).

[204] D. H. Douglass, "Magnetic Field Dependence of the Superconducting Energy Gap", Phys. Rev. Lett. **6**, 346–348 (1961).

[205] T. Schwarz, J. Nagel, R. Wölbing, M. Kemmler, R. Kleiner, and D. Koelle, "Low-Noise Nano Superconducting Quantum Interference Device Operating in Tesla Magnetic Fields", ACS Nano **7**, 844–850 (2013).

[206] M. Spiecker, A. I. Pavlov, A. Shnirman, and I. M. Pop, "Solomon equations for qubit and two-level systems: Insights into non-Poissonian quantum jumps", Phys. Rev. A **109**, 052218 (2024).

[207] E. Cartier, J. H. Stathis, and D. A. Buchanan, "Passivation and depassivation of silicon dangling bonds at the Si/SiO2 interface by atomic hydrogen", Appl. Phys. Lett. **63**, 1510–1512 (1993).

[208] A. A. Clerk and D. W. Utami, "Using a qubit to measure photon-number statistics of a driven thermal oscillator", Phys. Rev. A **75**, 042302 (2007).

[209] G. Zhang, Y. Liu, J. J. Raftery, and A. A. Houck, "Suppression of photon shot noise dephasing in a tunable coupling superconducting qubit", npj Quantum Inf. **3**, 1–4 (2017).

[210] S. Kogan, *Electronic Noise and Fluctuations in Solids* (Cambridge University Press, Cambridge, England, UK, Aug. 1996).

[211] Z.-T. Zhuang, D. Rosenstock, B.-J. Liu, A. Somoroff, V. E. Manucharyan, and C. Wang, "Non-Markovian Relaxation Spectroscopy of Fluxonium Qubits", arXiv, 10.48550/arXiv.2503.16381 (2025).

[212] S. E. de Graaf, L. Faoro, L. B. Ioffe, S. Mahashabde, J. J. Burnett, T. Lindström, S. E. Kubatkin, A. V. Danilov, and A. Y. Tzalenchuk, "Two-level systems in superconducting quantum devices due to trapped quasiparticles", Sci. Adv. **6**, 10.1126/sciadv.abc5055 (2020).

[213] J. J. Burnett, A. Bengtsson, M. Scigliuzzo, D. Niepce, M. Kudra, P. Delsing, and J. Bylander, "Decoherence benchmarking of superconducting qubits", npj Quantum Inf. **5**, 1–8 (2019).

[214] S. Ihssen, S. Geisert, G. Jauma, P. Winkel, M. Spiecker, N. Zapata, N. Gosling, P. Paluch, M. Pino, T. Reisinger, W. Wernsdorfer, J. J. Garcia-Ripoll, and I. M. Pop, "Low crosstalk modular flip-chip architecture for coupled superconducting qubits", Appl. Phys. Lett. **126**, 10.1063/5.0245667 (2025).

[215] M. O. Hecht, K. Saurav, E. Vlachos, D. A. Lidar, and E. M. Levenson-Falk, “Beating the Ramsey limit on sensing with deterministic qubit control”, Nat. Commun. **16**, 1–8 (2025).

[216] S. Danilin, A. V. Lebedev, A. Vepsäläinen, G. B. Lesovik, G. Blatter, and G. S. Paraoanu, “Quantum-enhanced magnetometry by phase estimation algorithms with a single artificial atom”, npj Quantum Inf. **4**, 1–8 (2018).

[217] P. Paluch, M. Spiecker, N. Gosling, V. Adam, J. Kammhuber, K. Vermeulen, D. Bouman, W. Wernsdorfer, and I. M. Pop, “Thermalization of a flexible microwave stripline measured by a superconducting qubit”, Appl. Phys. Lett. **126**, 10.1063/5.0243116 (2025).

[218] F. Valenti, A. N. Kanagin, A. Angerer, L. Buimaga-Iarinca, C. Morari, J. Schmiedmayer, and I. M. Pop, “Hydrogen crystals reduce dissipation in superconducting resonators”, Phys. Rev. B **109**, 054503 (2024).

[219] J. B. Hertzberg, E. J. Zhang, S. Rosenblatt, E. Magesan, J. A. Smolin, J.-B. Yau, V. P. Adiga, M. Sandberg, M. Brink, J. M. Chow, and J. S. Orcutt, “Laser-annealing Josephson junctions for yielding scaled-up superconducting quantum processors”, npj Quantum Inf. **7**, 1–8 (2021).